

# **Ultrafast Dynamics of Nanoparticles in Highly Intense X-Ray Pulses**

vorgelegt von

Master of Science  
**Maximilian Jakob Bucher**

geb. in Frankfurt am Main

von der Fakultät II - Mathematik und Naturwissenschaften  
der Technischen Universität Berlin  
zur Erlangung des akademischen Grades

Doktor der Naturwissenschaften  
- Dr. rer. nat. -

vorgelegte Dissertation

Promotionsausschuss:

Vorsitzender: Prof. Dr. Mario Dähne  
Berichter/Gutachter: Prof. Dr. Thomas Möller  
Berichter/Gutachter: Prof. Dr. Christoph Bostedt

Berlin 2017



## Kurzfassung

Mit der Entwicklung von Freie-Elektronen-Lasern im Röntgen Wellenlängenbereich, wie der *Linac Coherent Light Source* (LCLS), sind strukturelle Studien an Nanopartikeln möglich. Eine Herausforderung bei diesen Studien mit höchst intensiven Röntgenpulsen ist die Schädigung der Nanopartikel, da dies die Auflösung limitiert. Nur ein fundiertes Verständnis von Strahlungsschäden, wie die Nanoplasma-Bildung und -Expansion, kann die Auflösung verbessern. Weiterhin wurde vorgeschlagen, dass eine Schutzhülle die schädigenden Prozesse und die Expansion von Nanopartikeln verlangsamen können.

Diese Arbeit untersucht die Nanoplasma-Bildung und -Expansion in nanometergroßen He-, Xe- und HeXe-Cluster, wobei HeXe-Cluster ein Modellsystem sind, um die Funktion von solchen Schutzhüllen zu untersuchen. Die Nanopartikel werden durch eine Überschall-Expansion von kaltem Gas ins Vakuum gebildet und werden an dem Röntgenlaser LCLS mit Röntgenstrahlungs-Doppelpulsen zeitaufgelöst untersucht. Hierbei startet ein Pump-Puls die Nanoplasma-Entwicklung mit Intensitäten von  $\sim 2 \cdot 10^{16} \text{ W cm}^{-2}$  und ein Probe-Puls erzeugt Beugungsbilder von dem Nanoplasma zu einem späteren Zeitpunkt  $\Delta t$ , mit Intensitäten von  $\sim 2 \cdot 10^{17} \text{ W cm}^{-2}$ . Die Verzögerung  $\Delta t$  wird zwischen (0 to 800) fs variiert und die finale Ionenverteilung wird mit einem Flugzeit-massenspektrometer (TOF) gemessen. Das Experiment dieser Arbeit ist in der LAMP Kammer des AMO Instruments an der LCLS durchgeführt worden. Ein wesentlicher experimenteller Teil dieser Arbeit war der Bau, die Inbetriebnahme, und die Teilnahme an Design-Diskussionen von der LAMP Kammer.

Die Studie zeigt Einzelschuss Beugungsbilder und TOF Spektren von Xe-, He- und HeXe-Clustern mit einer bisher unerreichten Auflösung. So ist beispielsweise die Rekonstruktion eines  $\sim 25 \text{ nm}$  Radius großen Xe-Cluster mit  $\sim 6 \text{ nm}$  Auflösung gezeigt. Die Beugungsbilder und Rekonstruktionen zeigen, wie sich die Nanopartikel zu einem expandierenden Nanoplasma entwickeln. Die Auswertung einiger hundert Einzelschussbeugungsbilder zeigt die Ausdehung der Xe-Cluster um etwa 20 % binnen 800 fs. Rekonstruktionen und 2D Computer Simulationen belegen, dass HeXe-Cluster eine Rosinenkuchenstruktur besitzen, da Xe-Atome in dem He-Tröpfchen zu mehreren kleinen Clustern kondensieren. TOF Spektren zeigen, dass Xenon kinetische Energie an die Schutzhülle aus Helium transferiert und, dass die Schutzhülle als Elektronenreservoir für das Xenon dient. Die Beugungsbilder der HeXe-Cluster weisen auf, dass Xe-Cluster in den ersten 800 fs praktisch nicht expandieren, während die He-Schutzhülle einer Nanoplasma-Expansion unterliegt. Abschließend wird die Nanoplasma-Expansion von reinen Xe- und He-Clustern, sowie gemischten HeXe-Clustern miteinander verglichen.

## Abstract

With the advent of X-ray free electron laser, such as the Linac Coherent Light Source (LCLS), structural studies on non-repetitive and non-reproducible nanoparticles, such as single biomolecules appear imminent. A key challenge to increasing the resolution of single particle imaging is radiation damage. Only a sound understanding of the underlying damage processes, such as the nanoplasma expansion, can overcome this challenge and will lead to higher spatial resolutions. Further, sacrificial layers have been proposed to slow the nanoplasma expansion.

This thesis investigates nanoplasma formation and expansion in superfluid He-, bulk Xe- and heterogeneous HeXe-clusters, whereby HeXe-clusters are testbed nanoparticles for sacrificial layers. The clusters are generated through a supersonic gas expansion into a vacuum and investigated using an ultrafast X-ray pump–X-ray probe technique from the LCLS. A first X-ray pulse triggers the nanoplasma evolution at intensities of  $\sim 2 \cdot 10^{16} \text{ W cm}^{-2}$ , and a second X-ray probe-pulse, with power densities of  $\sim 2 \cdot 10^{17} \text{ W cm}^{-2}$ , creates diffraction images of the nanoplasma at a later time,  $\Delta t$ .  $\Delta t$  is varied between (0 to 800) fs and furthermore ion-spectra are captured via time-of-flight (TOF) mass spectroscopy. The experiment was performed at the AMO instrument using the LAMP end-station at LCLS. The LAMP end-station was partly designed, built, and operated as part of this thesis work.

The study reveals single-shot diffraction images and TOF spectra of Xe-, He- and HeXe-clusters with unprecedented resolution, for example, the reconstruction of a  $\sim 25 \text{ nm}$  radius Xe-cluster with  $\sim 6 \text{ nm}$  resolution is shown. The diffraction images and corresponding reconstructions show the nanoplasma formation and expansion of those clusters. An analysis of several hundred diffraction images suggests that the initial Xe-cluster radius increases by  $\sim 20\%$  over 800 fs. Therefore, the expansion-speed is  $\sim 15\,250 \text{ m s}^{-1}$ , and the electron temperature is  $\sim 125 \text{ eV}$ . Reconstructions and 2D computer models of few-hundred nanometer radius HeXe-clusters indicate that they agglomerate similar to a plum-pudding model, as Xe-atoms condense to multiple small clusters within the He-droplet. TOF spectra strongly imply that the Xe-clusters transfer kinetic energy to the sacrificial layer and that the He-layer supplies electrons to the ionized Xe-clusters. Diffraction images and 2D computer models of HeXe-clusters show that encapsulated Xe-clusters do not exhibit detectable damage in the initial 800 fs, while the He-layer undergoes an expansion. As a measure of the effectiveness of the sacrificial layer, the radiation damage of pristine He- and Xe-clusters, as well as HeXe-clusters are compared to each other.

# Contents

<b>1</b>	<b>Introduction</b>	<b>1</b>
<b>2</b>	<b>Fundamental Concepts</b>	<b>5</b>
2.1	Why X-ray free electron lasers? . . . . .	5
2.1.1	Generating X-rays with undulators . . . . .	7
2.1.2	Self-amplification by spontaneous emission . . . . .	9
2.1.3	Soft X-ray self-seeding . . . . .	11
2.1.4	Novel X-ray pump–X-ray probe techniques . . . . .	13
2.2	Rare-gas clusters . . . . .	17
2.2.1	Production of homogenous clusters: The supersonic gas expansion . . . . .	17
2.2.2	Creation of heterogeneous clusters: The pickup principle . . . . .	23
2.3	Fundamental processes of soft X-rays and nanoparticles . . . . .	24
2.3.1	Photoionization and core-hole decay . . . . .	25
2.3.2	From Thomson scattering to diffractive imaging . . . . .	29
2.3.3	Generalized index of refraction . . . . .	33
2.4	Clusters in intense soft X-ray pulses . . . . .	35
2.4.1	Formation and expansion of a nanoplasma . . . . .	36
2.4.2	Sacrificial layers slow the nanoplasma expansion . . . . .	40
<b>3</b>	<b>Experimental Considerations</b>	<b>45</b>
3.1	The X-ray beam transport to the LAMP end-station . . . . .	46
3.2	The LAMP end-station at the AMO instrument . . . . .	48
3.3	The large area pnCCD detectors . . . . .	51
3.4	Sample delivery . . . . .	54
3.4.1	Sample jet timing at LCLS . . . . .	56
3.5	Time-of-flight mass-spectrometer . . . . .	58
3.6	X-ray focus characterization . . . . .	61
3.6.1	Focus characterization using a TOF spectrometer . . . . .	61
3.6.2	Focus characterization via an imprint study . . . . .	62

## *Contents*

<b>4 Methods</b>	<b>65</b>
4.1 The computing environment at LCLS . . . . .	65
4.2 pnCCD photon detectors . . . . .	67
4.2.1 Combining multiple pnCCD detectors . . . . .	69
4.3 Phase retrieval from a single diffraction pattern . . . . .	72
4.3.1 Principle of phase retrieval . . . . .	73
4.3.2 2D reconstructions and image resolution . . . . .	74
4.3.3 1D projections and phase reconstructions . . . . .	78
4.4 Impact of the X-ray pump–X-ray probe on diffraction pattern . . . . .	78
4.5 2D electron density and diffraction image simulations . . . . .	80
4.6 Data filtering . . . . .	81
<b>5 Results and discussion</b>	<b>85</b>
5.1 Ion time-of-flight X-ray pump–X-ray probe data . . . . .	85
5.1.1 Time-dependent response of Xe-atoms and -clusters to intense X-rays . . . . .	85
5.1.2 Time-resolved response of highly ionized He- and HeXe-clusters . . . . .	87
5.2 Scattering response of rare-gas clusters . . . . .	91
5.2.1 Structural damage in Xe-clusters induced by intense X-rays . . . . .	91
5.2.2 X-ray induced damage in pristine He-cluster . . . . .	99
5.2.3 Condensation of xenon in helium cluster: Plum-pudding type cluster . . . . .	100
5.2.4 Understanding sample damage in the plum-pudding type clusters . . . . .	105
5.2.5 Sacrificial layers: Comparison of sample damage in HeXe-cluster . . . . .	108
<b>6 Summary and outlook</b>	<b>111</b>
<b>Appendix</b>	<b>115</b>
1 Python code on combining detectors . . . . .	115
2 Matlab code on spherical integrations . . . . .	117
3 Python code on 1D phase-retrieval . . . . .	118
<b>Bibliography</b>	<b>121</b>
<b>Publikationsliste</b>	<b>A</b>
<b>Eidesstattliche Versicherung</b>	<b>C</b>
<b>Acknowledgment</b>	<b>E</b>

# List of Figures

1.1	Conceptual setup of a single particle imaging experiment. . . . .	2
1.2	Computer simulations of aluminum spheres with tamper layers . . . . .	3
2.1	Aerial view of the Linac Coherent Light Source. . . . .	6
2.2	Schematics of several X-ray generating methods. . . . .	8
2.3	Undulator gain curve correlated to microbunching. . . . .	9
2.4	SASE single-shot and average spectra. . . . .	11
2.5	Schematic setup of soft X-ray self-seeding system. . . . .	12
2.6	Soft X-ray self-seeding spectra and brilliance of various light sources. . . . .	13
2.7	Schematic setup of an undulator based pump–probe scheme. . . . .	14
2.8	Schematic setup of a bunch based pump-probe setup. . . . .	16
2.9	Schematic of a supersonic gas expansion into a vacuum. . . . .	19
2.10	Schematic of a pickup (gas-)source. . . . .	23
2.11	Total cross-section of atomic carbon. . . . .	25
2.12	Schematic illustration of fundamental light-matter processes. . . . .	26
2.13	Total absorption cross-sections for helium and xenon. . . . .	26
2.14	Fluorescence peaks from xenon and neon K-LL Auger spectrum. . . . .	28
2.15	Principle of scattering rays of an atom. . . . .	31
2.16	Schematic of the nanoplasma formation and expansion. . . . .	36
2.17	Measurement and simulation of the nanoplasma expansion in Xe-clusters. . . . .	38
2.18	Experiment that shows early evolution of the nanoplasma transition. . . . .	39
2.19	Tamper layers and nanoparticles that undergo a nanoplasma formation. . . . .	42
3.1	Schematic overview of the AMO beamline instrumentation. . . . .	46
3.2	Overview of the AMO instrument in the LAMP end-station configuration. . . .	48
3.3	Inside view of the C1 chamber showcasing the interaction region. . . . .	49
3.4	pnCCD detector geometry in the LAMP instrument. . . . .	50
3.5	Geometry of a single pnCCD module. . . . .	52
3.6	Sideview of double sample jet configuration. . . . .	54

*List of Figures*

3.7	Schematic of the Parker-Hannifin Series 99 valve.	55
3.8	Schematic of the LCLS event receiver (EVR) timing system.	56
3.9	Event receiver time delay at LCLS for supersonic gas jets.	58
3.10	Drawing of the time-of-flight spectrometer.	60
3.11	Sideview of the spectrometer showing ion, electron and photon trajectories.	60
3.12	Focal spot analysis using a time-of-flight ion spectrometer.	62
3.13	Focal spot analysis via an ex-situ microscope imprint study.	63
4.1	Diagram of the computing environment at LCLS and DAQ traffic.	66
4.2	ADU histograms from electronic noise of dark pnCCDs.	68
4.3	Front and rear pnCCD arranged to combine measured diffraction image.	71
4.4	Spherical projection of 2D diffraction image onto 1D.	72
4.5	Example of a phase retrieval algorithm.	73
4.6	Illustration of resolution enhancement and diffraction image cropping.	76
4.7	Influence of X-ray pump–X-ray probe pulses to a diffraction image.	79
4.8	Used electron densities in 2D real and Fourier space simulations.	80
4.9	Comparison of analytical derived scattering and numerical simulations.	82
4.10	Schematic of data treatment and hit-finding procedures.	82
5.1	Time-resolved answer of xenon atoms in TOF spectroscopy.	86
5.2	Time-dependent response of atomic xenon in TOF spectroscopy.	87
5.3	Time-resolved answer of xenon clusters in TOF spectroscopy.	88
5.4	Time-resolved answer of He-clusters in TOF spectroscopy.	88
5.5	TOF spectra of HeXe-clusters with a ~0.6 % Xe-doping at various $\Delta t$ .	89
5.6	TOF spectra of HeXe-clusters with ~0.06 % Xe-doping at various delays.	90
5.7	Single Xe-cluster size distribution at varying time delay $\Delta t$ .	92
5.8	Average cluster size correlated to measured intensity on front pnCCD.	93
5.9	Time-resolved behavior of number of scatterers due to nanoplasma expansion	94
5.10	Single-shot diffraction patterns of Xe-clusters at varying time delays	96
5.11	Single-shot 2D reconstructions of ~25 nm radius Xe-clusters.	97
5.12	Single-shot 1D reconstruction of ~30 nm radius Xe-cluster	98
5.13	Recovered Amplitudes $ A $ and phase factor of 1D reconstruction	99
5.14	Single-shot diffraction images of He-droplets at different time delays	100
5.15	Diffraction image of HeXe-cluster at 0.5 % Xe-doping.	101
5.16	From a HeXe-cluster reconstruction to a simulated electron density.	102
5.17	Hypothetical arrangements of Xe-clusters within He-droplets.	104

*List of Figures*

5.18 Simulated structural damage scenarios in HeXe-clusters. . . . .	106
5.19 Simulation and exp. data: Structural damage in He-droplet. . . . .	107
5.20 Single-shot diffraction patterns of HeXe-cluster at different time delays . . . . .	109



# List of Tables

2.1	Parameter $K_{\text{gas}}$ values for rare-gases. . . . .	21
2.2	Subshell absorption cross-sections and ionization potentials for xenon. . . . .	27
2.3	Absorption cross-sections and ionization potentials for xenon and helium . . .	27
2.4	Atomic scattering factors for helium and xenon. . . . .	33
3.1	Summary of LCLS beam parameters during experiment. . . . .	48
3.2	pnCCD gain modes and typical ADU values at 1 keV photons. . . . .	53
3.3	Installed vacuum pumps in the experiment. . . . .	54
3.4	Terminal velocities of some rare gases at room temperature, $T = 293.15$ K. . . .	58
3.5	Applied voltages to the time-of-flight spectrometer (ion side use only). . . . .	61
4.1	Typical parameters used in the Hawk software package. . . . .	74
5.1	Relative comparison of measured scattering versus expected scattering. . . . .	110



# 1 Introduction

Following the discovery of X-radiation at the end of the 19<sup>th</sup> century by Röntgen [1], X-rays have been used to understand and investigate matter in new ways. Soon after this discovery, X-rays were used to take the first medical image. Later, X-rays led to the understanding of fundamental aspects of atoms [2] and crystals [3, 4]. Today, the success story continues in various fields of science. A large and active scientific field is structural biology [5, 6]. Here, X-rays are being used to study the structure of proteins through crystallography. Proteins are the so-called “workhorse” in the human body and the structure of a protein defines its biological function. Unfortunately not all proteins can be grown into large crystals making the molecular structure determination challenging. However, new light sources, namely X-ray free-electron lasers (XFELs) [7], have more and more peak brightness allowing the structure determination of smaller and smaller protein-crystals [8].

The first free-electron laser reaching into the hard X-ray wavelength range was built at Stanford University and is called the Linac Coherent Light Source (LCLS) [9]. It is a 3.2 km long machine that produces X-rays with wavelengths from (4.6 to 0.1) nm, provides intensities of up to  $\sim 10^{21}$  W cm<sup>-2</sup>, and has ultra-short pulses ranging from (1 to 500) fs. Scientists from various disciplines can apply to use this light source for their experiments, which are conducted in several instruments. The Atomic, Molecular, and Optical physics (AMO) instrument [10] at the LCLS was the first of seven instruments in operation and has conducted experiments ranging from biological imaging to basic science [11].

The intense pulses from XFELs open up an entirely new method for biologists, which is the single particle imaging (SPI). With SPI (see Figure 1.1), the shape of single nanoscale samples can be determined through diffractive imaging [12]. First experiments have successfully delivered single-shot diffraction images of biological particles, such as viruses [13], and non-biological particles, such as rare-gas clusters [14]. It has been a rapidly developing field that has recently succeeded in visualizing 3D images of nano-objects [15, 16].

But, the highly-intense pulses that enable diffractive imaging lead to new questions. When an

## 1 Introduction

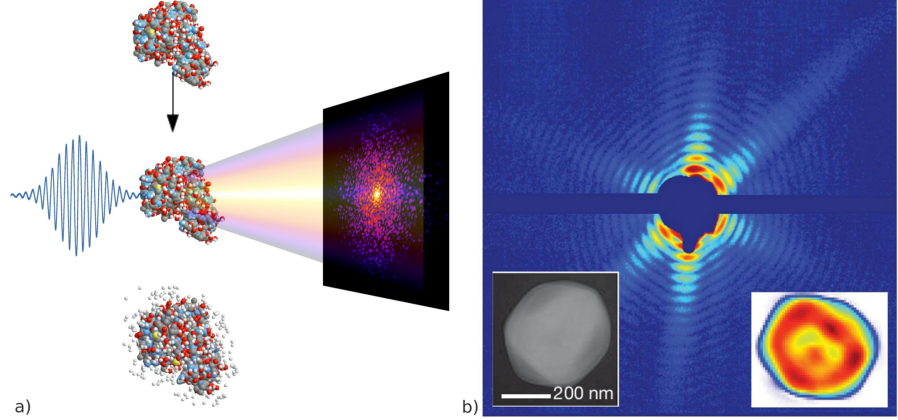


Figure 1.1: a) Conceptual setup of a single particle imaging experiment. A nanoparticle is injected and intercepted by an XFEL pulse. The nanoparticle diffracts light before it is destroyed and the diffraction is recorded with a detector. b) Single-shot diffraction image and reconstruction (right inset) of a single Mimivirus. An electron-microscopy image is shown as comparison (left inset). From [13, 17, 18].

intense X-ray pulse irradiates a nanoparticle, the particle will simultaneously absorb and scatter X-rays with the absorption cross-section typically being much larger than the scattering cross-section. From the first moment of light-matter interaction, the absorption will lead to inner atomic-shell vacancies [19] and these vacancies make the above mentioned cross-sections time-dependent. Subsequent core-hole decays, such as the Auger decay, typically occur only a few femtoseconds later and the nanoparticle is thus transformed into a nanoplasm on a femtosecond timescale [20]. Several forces will ultimately expand the plasma [21, 22] until eventually, the nanoplasm disintegrates into its atomic components.

The underlying principle of diffractive imaging, which is that intense X-ray pulses diffract from a single structure before they destroy it<sup>1</sup> [18], demands very short and intense light pulses [23, 24]. These will not become available at the currently planned light sources. Therefore, time-dependent scattering factors and trapped or delocalized electrons will affect the diffraction image [25]. While diffractive imaging is already feasible, these fundamental processes will limit the achievable resolution in single particle imaging. Several ideas have been proposed to address radiation damage in single particle imaging: Atomistic computer models could theoretically account for known damage processes in small systems [26–28]; and sacrificial tamper layers slow the nanoplasm expansion [29–34]. The tamper consists of thin layers surrounding a single particle. When a tampered particle is exposed to intense X-rays, charge-transfer occurs from the

---

<sup>1</sup>This is often referred to as “diffraction before destruction”.

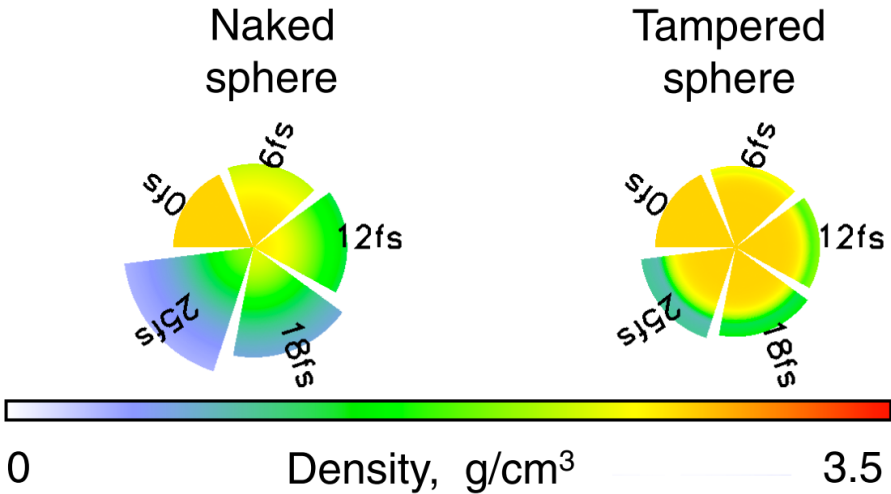


Figure 1.2: Computer simulations of 7.5 nm radius aluminum spheres that are illuminated by intense soft X-rays with a fluence of  $2.5 \cdot 10^8 \text{ J cm}^{-2}$ . On the left is a pristine Al-sphere and on the right is a Al-sphere with a 2.5 nm thick silicon layer (tamper). From [33]. Reprinted with permission from the American Physical Society (APS).

photoionized sample to the tamper. The increasingly ionized layers are shed off or sacrificed and radiation damage of the encapsulated sample is retarded (see Figure 1.2). A part of this thesis is concerned with the investigation of sacrificial layers.

An effective sacrificial layer would ideally be thin and uniform around the sample to minimize its background signal. The initial idea of a tamper material was water, since bio-molecules are typically embedded in water-based layers when injected into typical diffractive imaging setups using an aerosol sample jet. However, water-based tampers become disordered in thicker layers and are usually uneven around macro-molecules [25]. As an alternative, helium layers have been proposed as a tamper material [35], but it is unclear if materials with low atomic numbers are a good tamper material [30]. Currently, aerosol sample jets use helium to dry the injected sample before injection and a next step that is discussed [36] is to equip a sample with a helium tamper during the injection process.

This thesis discusses the nanoplasma transformation and expansion in solid Xe-, superfluid He- and heterogeneous HeXe-clusters. These rare-gas clusters are a testbed to study nanoparticles in intense X-rays [37]. Particularly the sacrificial layer physics can be studied with HeXe-clusters. A novel X-ray pump–X-ray probe method [38] was employed to study the nanoplasma formation in those samples. Here, a pump-pulse triggers a nanoplasma formation and a probe-pulse creates

## *1 Introduction*

a diffraction image of the system at a later time. Diffraction images and time-of-flight mass spectra are measured coincidentally and are further analyzed. Real-space reconstructions of the clusters are shown with thus far unprecedented resolution and the analysis allows to answer the following questions:

- How does an X-ray induced nanoplasma expansion affect the shape of Xe-clusters?
- What is the structure of HeXe-clusters?
- Does helium act as sacrificial layer in mixed HeXe-clusters?

This thesis is organized as follows: Chapter 2 discusses fundamental aspects that are used throughout this study; Chapter 3 describes the experimental setup at the AMO instrument at LCLS and in particular the LAMP end-station with its detectors; Chapter 4 discusses several computational methods; Chapter 5 presents the results of the X-ray pump–X-ray probe study; and Chapter 6 summarizes the present work and provides an outlook for further studies.

## 2 Fundamental Concepts

This chapter condenses the theoretical concepts that will recur throughout this thesis. The chapter starts off in Section 2.1 with an introduction to the key aspects of X-ray free electron lasers (XFEL), including the beam operating modes self-amplified spontaneous emission (SASE), self-seeding, and multipulse operations. Section 2.2 is about the formation of rare-gas clusters via supersonic jets and pickup sources. We then dive into the interaction of light and matter in Section 2.3 that discusses coherent, elastic X-ray scattering, and absorption in atoms. The chapter ends with Section 2.4, describing nanoplasma formation in pristine clusters and core-shell systems.

### 2.1 Why X-ray free electron lasers?

X-rays were first created through *Bremsstrahlung*, where an electron beam with kinetic energies of (0.1 to 100) keV hits a block of copper and the deceleration of electrons in the copper led to the creation of X-rays. Since then, there has been immense progress in the creation of X-rays. For scientific purposes, X-rays are commonly created in X-ray synchrotron light sources and are often referred to as a “synchrotron facility”. In a synchrotron facility, electrons are produced in bursts by an electron gun and formed to a collimated electron bunch. Then, these electrons are accelerated near the speed of light, and injected into a synchrotron that keeps the kinetic energy of the electrons constant. In a synchrotron, the electrons are deflected by bending magnets (see Figure 2.2a) to travel around a closed-loop path. The deflection of the electrons at a bending magnet leads to the emission of X-rays. Typically, a synchrotron can store many electron bunches allowing a high repetition rate of light pulses on the order of megahertz. The X-ray pulses are characterized through a parameter that is called spectral brightness [39] or sometimes brilliance. We can define the spectral brightness as [40]

$$B = \frac{n}{A \Theta \Delta E}, \quad (2.1)$$

with  $n$  being the number of photons per second,  $A$  the source area,  $\Theta$  the divergence of the beam, and  $\Delta E$  being the spectral bandwidth of the light pulse. The spectral brightness is an overall measure of the quality of a light source. The development of modern synchrotron light sources

## 2 Fundamental Concepts



Figure 2.1: Aerial view of the Linac Coherent Light Source. LCLS uses the last third of SLAC’s linear accelerator but is overall a multikilometer long machine. The accelerator and buildings are stretched far because of the light generation process. From [41]

is hence often measured and compared to previously achieved brightness values. The motivation to improve the peak brightness is manifold and follows the recipe to let a sample interact with as many photons possible, in the shortest time possible, and with the best energy resolution possible. In other words, higher peak brightness light sources enable imaging of even smaller particles, or investigate dynamics that are even faster.

To get a numerical understanding, let us look at sequential photon absorption dynamics in atoms and molecules. One can conservatively estimate that a typical absorption cross section for soft X-rays<sup>1</sup> is around  $\sigma = 1$  megabarn (Mb) [42]. Typical X-ray foci<sup>2</sup> are  $A = 1 \mu\text{m}^2$  such that the number of photons,  $n_{in}$ , needed to absorb just one photon per atom,  $n_{abs} = 1$ , is

$$n_{in} = \frac{n_{abs}A}{\sigma} = \frac{10^{-8}}{10^{-18}} \frac{\text{cm}^2}{\text{cm}^2} = 10^{10} \quad \text{photons.} \quad (2.2)$$

We can compare this to a modern synchrotron source, for example, the Advanced Photon Source at Argonne National Laboratory. This synchrotron facility produces  $\sim 10^6$  photons per pulse in the Si(111) bandwidth at similar focal area conditions and with pulse durations of 40 ps [43]. That is far out of reach for investigating non-linear or multi-photon processes. While this back of the envelope type of calculation might be off by an order of magnitude or so depending on the specific case, it illustrates the orders of magnitude increase in the number of photons scientists were looking for to unravel entirely new aspects of X-ray science. As it is not possible to use conventional optical methods to increase the number of X-ray photons, drastic ideas were needed.

---

<sup>1</sup>Soft X-rays have wavelengths of (10 to  $\sim 0.2$ ) nm

<sup>2</sup>The focus size at the AMO instrument of LCLS is  $1 \mu\text{m}^2$ .

## 2.1 Why X-ray free electron lasers?

Reference [44] described in the 1970's the idea of coherent radiation in the ultraviolet to X-ray region, and over ten years later, the construction of free electron lasers was proposed [45, 46]. The Section 2.1.2 discusses the laser-like radiation in the X-ray region of these light sources in more detail.

Construction of the first hard XFEL, the Linac Coherent Light Source, finished in 2009. Figure 2.1 shows LCLS from a birds-eye view. LCLS is able to create  $\sim 10^{12}$  photons per pulse and achieves pulse-lengths of a few femtoseconds. The beam parameters of XFELs increased the peak brightness that is available at user facilities by many orders of magnitude<sup>3</sup>. This allows the study of, for example, the above mentioned sequential absorption of photons in atoms and molecules [19, 47], non-linear dynamics of atoms [48], the ultrafast movement of electrons in chemical reactions [49–51], and the imaging of nanoparticles [13, 52].

Only a few free-electron lasers (FELs) exist today. The Free-electron LASer Hamburg (FLASH) at *Deutsches Elektron Synchrotron* (DESY) in Germany, the LCLS at SLAC National Accelerator Laboratory (SLAC) in the United States, the Free Electron laser Radiation for Multidisciplinary Investigations (FERMI) at *Elettra-Sincrotrone* (ELETTRA) in Italy, and the SACLA at *Rikagaku Kenkyūsho* (RIKEN) in Japan. More FELs are being built around the world, for example, the European XFEL near DESY in Germany, the SwissFEL at *Paul Scherrer Institut* (PSI) in Switzerland, and the PAL-XFEL at Pohang Accelerator Laboratory (PAL) in South Korea.

### 2.1.1 Generating X-rays with undulators

In X-ray free-electron lasers, X-rays are generated from an electron bunch in an undulator. Undulators consist of magnets arranged in an alternating polarity. An electron bunch traveling through an undulator is “wiggled” along its path due to the magnetic fields, which cause the electrons to emit radiation (see Figure 2.2c). Although undulators are large constructs of a few meters and their magnet spacing is on the order of centimeters, traversing electrons near the speed of light can emit radiation on the nanometer wavelength range. This is due to a relativistic effect. In the frame of the electrons, the magnet spacing appears shorter.

Undulators can be characterized by the strength parameter,  $K$ , which is given by [53]

$$K = \frac{e B_{\max} \lambda_U}{2\pi m_e c}, \quad (2.3)$$

---

<sup>3</sup>See Figure 2.6 for an illustration of the improvement in peak brightness.

## 2 Fundamental Concepts

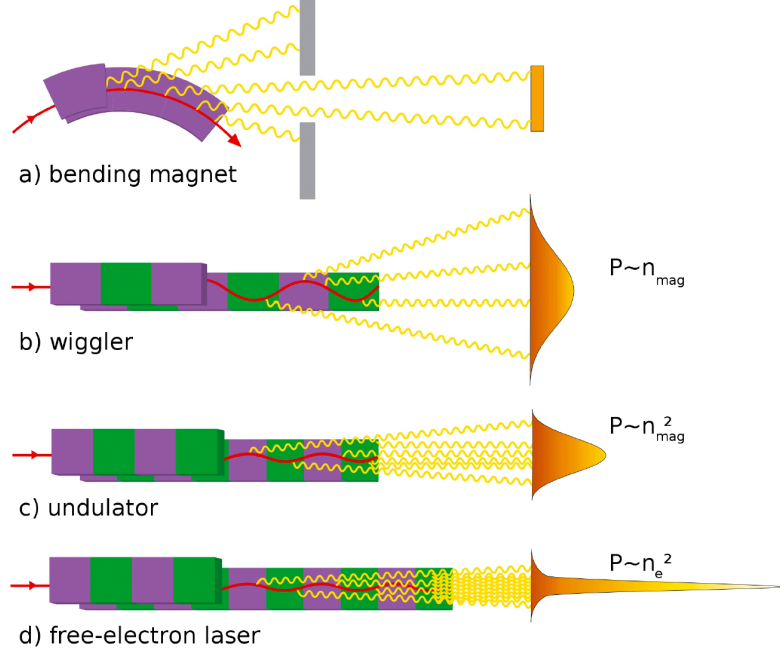


Figure 2.2: Schematics of several X-ray generating methods using magnets (purple & green). The red lines are pathways of the electron beams and the yellow lines represent emitted X-rays. The emitted spatial power distribution is orange. From [17].

where  $e$  is the elementary charge,  $B_{\max}$  is the maximum magnetic field in the undulator or wiggler,  $m_e$  is the mass of an electron,  $c$  is the speed of light, and  $\lambda_U$  is the so-called undulator period that corresponds to the magnet spacing.  $K$  can be expressed in convenient units as,

$$K \approx 0.934 B_{\max} \lambda_U \quad [\text{T cm}] . \quad (2.4)$$

Undulators usually have  $K < 1 \text{ T cm}$ . If  $K \gg 1 \text{ T cm}$  the magnet array is typically referred to as a wiggler (see Figure 2.2b). The X-rays emitted by undulators typically have a narrower spectrum and a higher flux than X-rays generated by wigglers. This is due to the fact that the undulator period and magnetic fields are chosen specifically in an undulator. The parameters are set such that their emitted radiation per period constructively interferes with each other. This resonance condition is expressed by the fundamental wavelength of an undulator,  $\lambda_r$ , and can be noted as [53]

$$\lambda_r = \frac{\lambda_U}{2\gamma} \left( 1 + \frac{K^2}{2} + \gamma^2 \Psi^2 \right), \quad (2.5)$$

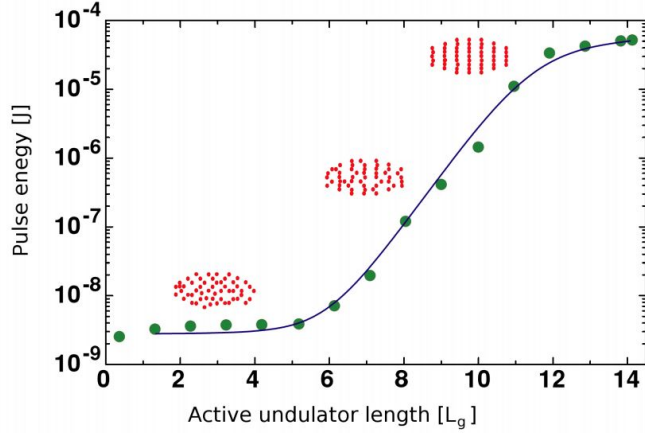


Figure 2.3: Undulator gain curve correlated to microbunching. The X-ray pulse energy is plotted logarithmically over the undulator length  $L_g$  (blue curve, green dots) and shows an exponential growth until saturation. The electron bunch (red dots) starts with a random density distribution. As the bunch travels through the undulator, its density is periodically modulated such that the electrons microbunch. Upon optimal microbunching, the X-ray lasing process saturates. From [17, 55]

with the Lorentz factor  $\gamma$  of the electron bunch in the undulator and the electron observation angle,  $\Psi$ . As a result, the emitted power,  $P$ , now scales as [54]

$$P \propto n_{\text{mag}}^2, \quad \text{in an undulator magnet.} \quad (2.6)$$

### 2.1.2 Self-amplification by spontaneous emission

If an electron bunch travels through just one undulator, the emitted power scales linearly with the number of electrons,  $n_e$ , which is due to the finite size and randomly distributed density of an electron bunch. If the electrons emit light from the same point or are separated by  $i \cdot \lambda_r$ , with  $i = (1, 2, 3, \dots)$ , the emitted photons would constructively interfere and be coherent [40]. This idea - to emit light from a point-like source - is exploited in XFELs by microbunching the electron bunches. Simplified this means that the electrons of a bunch are microscopically structured to stripes, which is illustrated in Figure 2.3. Following the figure, microbunching can be created in a straight and long undulator section<sup>4</sup>, where multiple undulators are connected in series. As the electron bunch travels in vacuum through the long XFEL undulator section, light is faster than the electrons. This slight velocity difference means that the co-propagating photons

---

<sup>4</sup>LCLS has a 112 m long undulator section.

## 2 Fundamental Concepts

and electrons have a phase difference and interact with each other. Depending on the phase, an electron will either gain or lose velocity. As a result, the initial uniform electron density is periodically modulated by the photon-field as it travels through the undulators of an XFEL [53]. The modulated electron bunch structure is called microbunching.

The key process in microbunching is that an electron bunch interacts with the emitted photon-field. The interaction occurs only because the particles have a narrow spatial and kinetic-energy distribution. The average spread of these distributions can be characterized by the so-called emittance. And only the linear accelerator components of a free electron laser (FEL) are able to compress an electron bunch in space and energy, i.e., create a low-emittance electron-bunch such that the electron bunch can interact with the photons and microbunch.

At LCLS, the low-emittance attribute effectively reduces the Equation 2.5 to  $\lambda_r(\Psi \rightarrow 0)$  [42]. This allows us to further describe the structure of the microbunching. Due to the velocity mismatch of the electrons and the photons, the photon-field travels the distance  $\lambda_r(\Psi = 0)$  more than the electron bunch over each undulator period,  $\lambda_U$ . This distance is also referred to as slippage and affects the modulation period of the electron density as mentioned above. The spacing between the dense areas is therefore  $\lambda_r(\Psi = 0)$  (see Figure 2.3). As the electron bunch becomes structured, it amplifies a narrower wavelength bandwidth around  $\lambda_r(\Psi = 0)$  through spontaneous emission. As more photons travel along-side the electron bunch, the bunch becomes even more structured and one speaks therefore of “self-amplification”. Eventually the microbunching is fully developed and the lasing process saturates.

This type of radiation, or XFEL operation mode, is called Self-Amplification by Spontaneous Emission (SASE). The emitted power,  $P$ , is now not only proportional to the square of the number of undulator magnets but due to the point-like emission it also scales as [40]

$$P \propto n_e^2, \quad \text{in SASE operation.} \quad (2.7)$$

Single-shot and average SASE spectra can be seen in Figure 2.4. A SASE spectrum is typically different from shot-to-shot and has distinct peaks on top of a more broad background. This is due to the initially emitted photons that have a pseudo-random wavelength within a narrow bandwidth. The electron-bunch amplifies these specific wavelengths as it travels through the undulators since its microbunching is defined by those specific wavelengths.

There are different types of FEL that can produce SASE radiation. Typically at longer wavelength

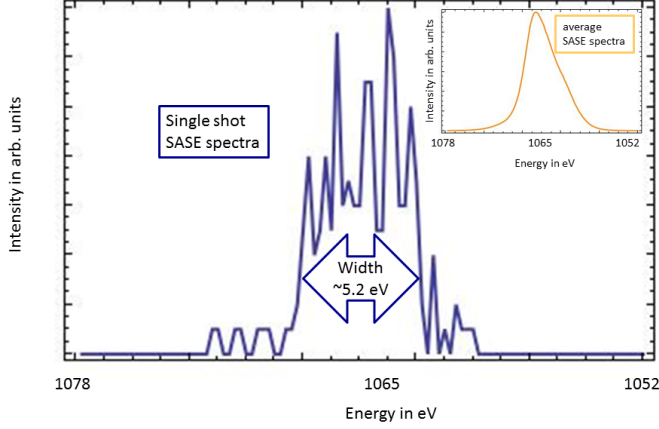


Figure 2.4: The large blue spectra is a SASE spectra from a single LCLS shot measured with a hemispherical analyzer [56]. Note the spiky peak structure on a background pedestal. Within the narrow bandwidth of an XFEL pulse some energies are more strongly amplified due to the microbunching. The yellow graph in the inset is an average spectrum of several hundred single-shots and shows a low energy tail, which is due to XFEL-jitter.

ranges, where efficient optics are readily available, a so-called multi-pass low-gain FEL is able to reuse electron-bunches, despite the fact that the lasing process affects the kinetic energy of the bunch. Without going into much detail, this FEL type leads to comparable high repetition rates and narrow spectra but few photons per pulse [57]. At shorter wavelength ranges, the kinetic energy of an electron bunch is drastically affected due to the X-ray lasing process. Additionally, there is a lack of efficient optics in the X-ray region. So, XFELs use only one electron-bunch<sup>5</sup>, which is dumped after a long undulator section. This is called a single-pass high-gain FEL.

### 2.1.3 Soft X-ray self-seeding

A special free electron laser beam mode is the seeded type. In contrast to the SASE operation, where the initial photons are randomly emitted and further amplified, a seeded FEL starts with a given seed of photons. If the set of initial photons is monochromatic, mostly this wavelength is amplified as the bunch travels through the undulator along-side the seed. The initial photon seed can be created through various processes and the wavelength of the photon seed is the critical parameter in determining which method to choose. In the case of the infra-red (IR) to

---

<sup>5</sup>The European XFEL uses a so-called bunch train, where multiple electron bunches are accelerated in series.

## 2 Fundamental Concepts

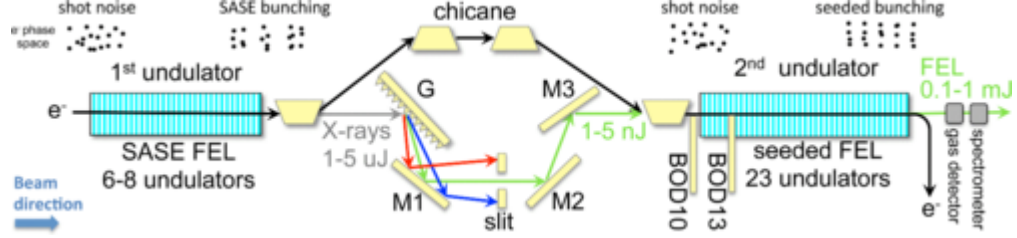


Figure 2.5: Schematic setup of the soft X-ray self-seeding system at LCLS. The X-rays are reflected of grating (G) and mirrors (M1-M3) and act as seed when they are overlapped with the electron bunch again using the beam overlap diagnostics (BOD10 & BOD13). From [58]. Reprinted with permission from APS.

extreme ultra-violet (XUV) wavelength range, conventional lasers can be used to produce the initial photon seed. However, due to the lack of lasers available at X-ray wavelengths, the idea of self-seeding is pursued.

Following Figure 2.5, an electron bunch is first sent through a few undulator magnets to generate a few SASE photons. The electrons and photons are then separated using a magnetic chicane, which also neutralizes the microbunching in the electron bunch. The grating monochromator selects a small wavelength slice from the comparably broad SASE spectrum of the initial photons. Photons exiting the monochromator are called the seed. The seed and the electron bunch are overlapped again using the magnetic chicane and then sent through more undulators. Here, the seed modulates the electron bunch and thus only a narrow spectral band is amplified. A typical spectrum of a soft X-ray self-seeded beam can be seen in the left panel of Figure 2.6. The characteristics of a self-seeded spectrum are an intense peak at the wavelength of the seed on top of a broad SASE background pedestal. The background is an artifact of the amplification of some spontaneous emission events and can be suppressed by using fewer undulator magnets. Self-seeded beams have a significantly reduced pulse energy – by an order of magnitude or so, depending on the exact beam parameters – as compared to LCLS SASE operations. However, in their main peak, self-seeded pulses have a higher spectral peak brightness when compared to SASE pulses. Using Equation (2.1), the increase in spectral brightness compared to SASE is understandable due to reduced bandwidth. The increase in peak brightness is illustrated in the right panel of Figure 2.6 and compared to other modern X-ray light sources.

Self-seeded beam operations have recently been demonstrated at LCLS. For hard X-rays, the Hard X-Ray Self-Seeding (HXRSS) instrument uses a diamond crystal to select a wavelength slice [60]. In the case of soft X-rays, the Soft X-ray Self Seeding (SX RSS) instrument uses a grating monochromator [58]. A seeded beam using an external laser to generate photons as

## 2.1 Why X-ray free electron lasers?

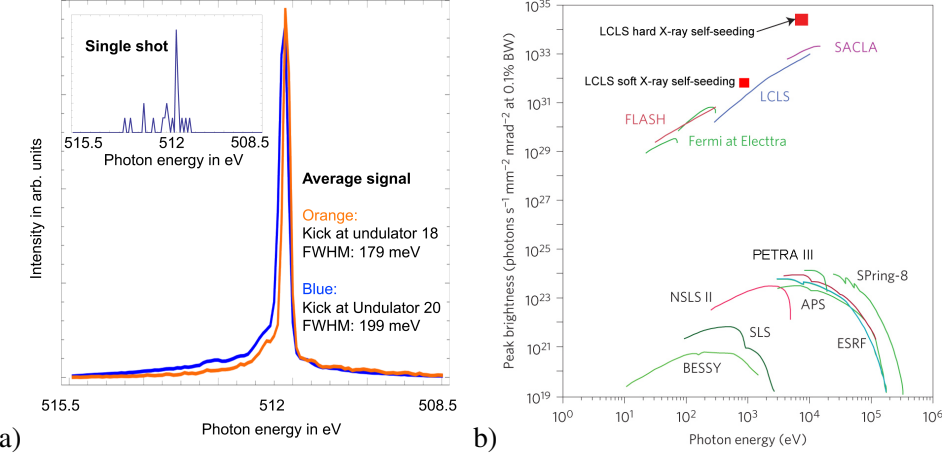


Figure 2.6: a) Normalized average spectra of soft X-ray self-seeding operations using the AMO instrument at LCLS. The self-seeding spectra is characterized by a sharp spectral peak around the seed energy, which is accompanied by a SASE pedestal. The often undesired pedestal is suppressed when the undulators length is shortened [56]. b) The peak brightness of various light sources over a wide photon energy range. Self-seeding operations have a higher peak brightness than current SASE operations. Adapted from [58, 59].

an initial seed has been demonstrated at the XUV-FEL FERMI [61]. The peak intensity in a narrow spectral band makes seeded beams interesting for a variety of applications, particularly in spectroscopy, where it is momentous to excite materials with narrow bandwidth photons. There are also applications in atomic and molecular physics, ranging from absorption spectroscopy [62], to ultrafast photoelectron spectroscopy on molecules [56], and to non-linear stimulated Raman spectroscopy [63]. Particularly interesting for this work is the magnetic chicane from the SXRSS instrument when used as described in the next section.

### 2.1.4 Novel X-ray pump–X-ray probe techniques

Pump–probe experiments are commonly used as they allow a precise study of dynamics. The pump-pulse gives a very controllable starting point, i.e., “time zero” in the dynamic process, and the probe-pulse can perform a measurement of the dynamics at a later time delay,  $\Delta t$ . Sometimes pump- and probe-pulse are switched, which is indicated by negative time delays and used to verify time zero, or to probe the system before any dynamics have occurred. It is often desirable to have a pump- and probe-pulse of different wavelength, for example, one can pair an optical laser pulse and an X-ray pulse. However, in order to study X-ray induced phenomena using X-ray imaging and spectroscopy techniques, as discussed in this thesis, two X-ray pulses are needed.

## 2 Fundamental Concepts

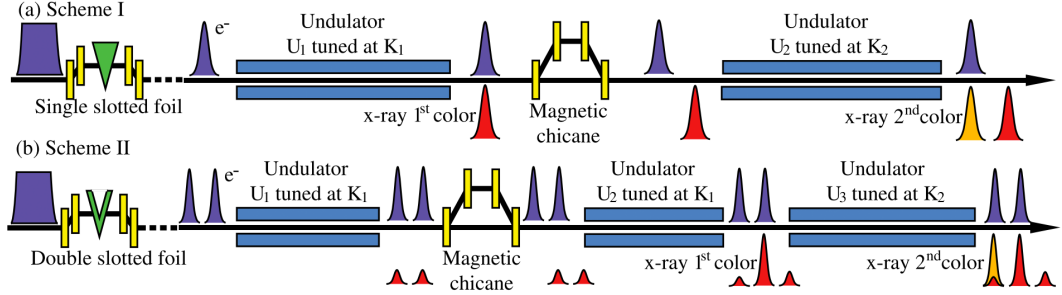


Figure 2.7: Schematic setup of undulator parameter- $K$  based pump–probe schemes at LCLS. In (a) Scheme I, one creates a single electron bunch using a single slotted foil. (b) Scheme II, one creates a double electron bunch using a double slotted foil. The electron bunches emit radiation with a wavelength depending on  $K_{1,2}$ . A time delay  $\Delta t$  between pulses is introduced using a magnetic chicane. From [38]. Reprinted with permission from APS.

Recently, two methods have been proposed to create two X-ray pulses to conduct a X-ray pump–X-ray probe experiment. Method one is a mirror-based beam split-and-delay system (XRSD device) [64–66]. It splits a single pulse into a pump- and probe-pulse, allowing a time delay of the latter. These systems are typically limited to short time delays, as the grazing incidence optics have to fit into existing setups. Method two uses accelerator-based schemes [38, 67] that manipulate electron bunches to create two X-ray pulses. Both methods have been demonstrated at LCLS and have been complementing the more widely available optical laser pump–X-ray probe methods, particularly in the chemical sciences [22, 50, 68].

The accelerator-based X-ray pump–X-ray probe method used in this thesis can also produce two X-ray pulses of different wavelength, which are so-called “two-color” pump–probe schemes. The generation of two-colored X-ray pulses is based on the parameters of Equation (2.5) and indicates two possible schemes: one, the undulator parameter,  $K$ , can be tuned to change the emitted wavelength; and two, the Lorentz factor,  $\gamma$ , can be different if there are two electron bunches. As the accelerator-based X-ray pump–X-ray probe method has been used in the present work, let us describe these schemes in greater detail.

### **Undulator parameter- $K$ based pump–probe schemes**

The first developed accelerator based X-ray pump–X-ray probe technique at LCLS [38] uses a difference in undulator parameters,  $K_{1,2}$ , to create two pulses of different wavelength. The time delay is introduced through a magnetic chicane.

## 2.1 Why X-ray free electron lasers?

A schematic setup is shown in Figure 2.7. Following the figure in the top panel (a) Scheme I, one electron bunch is created through a single slotted foil<sup>6</sup>. The use of the slotted foil enables control over the pulse duration. The electron bunch then travels through the undulator section  $U_1$  tuned at strength parameter  $K_1$  and is stimulated deep into the lasing process, but the lasing does not go into saturation such that the electron bunch can be reused in the second undulator section. A magnetic chicane removes the microbunching from the section  $U_1$  such that in undulator section  $U_2$ , tuned to undulator strength parameter  $K_2$ , the electron bunch lases again and the process is able to saturate. The maximal color separation between the two pulses is  $\sim 1.9\%$  in relative difference between  $K_1$  and  $K_2$ .

The time delay between the two pulses is introduced by a magnetic chicane that extends the pathway of the electrons and leaves photons unaffected. At LCLS, a dedicated chicane, for example, from the soft X-ray self-seeding instrument (see Section 2.1.3), can reach delays up to a maximum of 800 fs. In this scheme, several factors prevent a minimal time delay,  $\Delta t_{\min}$ , of zero. The minimal time delay opposed by the magnetic chicane,  $\tau_{\min}$ , is dictated by the electron drift velocity mismatch to the speed of light. We can express that as,

$$\tau_{\min} = \frac{l}{v_{\text{drift}}} - \frac{l}{c} \approx 50 \text{ as}, \quad (2.8)$$

with  $l \approx 4 \text{ m}$  being the length between undulator sections  $U_1$  and  $U_2$ ,  $c$  being the speed of light, and  $v_{\text{drift}}$  being the drift velocity of the electron bunch. As the electron bunch drifts undeflected through the chicane close to the speed of light  $\tau_{\min}$  is typically on the tens of attoseconds timescale. There is also a timing jitter between the two light pulses that is introduced by the magnetic chicane due to the magnetic field jitter and the electron beam energy jitter. The total contribution to the timing jitter is less than 0.4 % of the time delay imposed by the chicane. So, the delay chicane does not significantly contribute to the minimum time delay,  $\Delta t_{\min}$ . A bigger factor is the velocity mismatch of the light pulse and the electron bunch as they travel through a undulator section. This mismatch can be estimated by

$$\Delta t_{\min} - \tau_{\min} = \frac{N_u \lambda_r}{c}, \quad (2.9)$$

with  $N_u$  being the undulator periods. Given the parameters in study [38],  $\Delta t_{\min} = 3 \text{ fs}$ , such that a partial overlap between the electron bunch and light pulse could be achieved after the magnetic chicane. It should be noted that this scheme has been used in the described experiment.

---

<sup>6</sup>A single slotted foil or emittance-spoiling foil is typically inserted in a magnetic chicane. Here, it spoils the electron bunch by Coulomb scattering them leaving only a certain energy band of the electron bunch that is within the slot unspoiled. This usually narrows the electron beam and thus reduces its pulse duration [69].

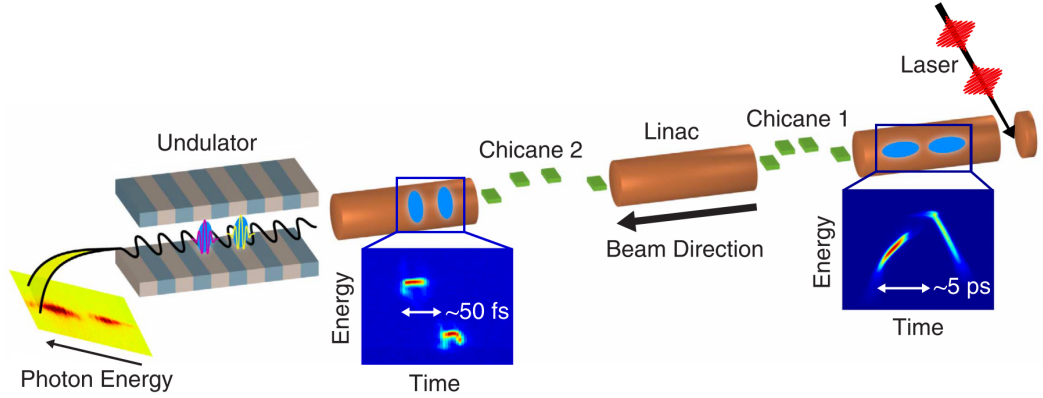


Figure 2.8: Schematic setup of the two bunch, two color pump–probe setup at LCLS. Two laser pulses shot at a cathode create two electron bunches with a delay  $\Delta t$  on the picosecond timescale. Two magnetic chicanes compress the bunches such that a delay  $\Delta t$  is on the ten femtosecond timescale. Both pulses go through one undulator section and the lasing process is saturated. The relative color separation is on the order of 1 % between the bunches. From [67].

#### The twin-bunch or Lorentz factor based pump–probe scheme

The second developed accelerator-based X-ray pump-X-ray probe technique at LCLS [67] uses two electron bunches of different energy. A schematic setup of this beam operation can be found in Figure 2.8. The electron bunches are created through a double laser pulse that impinges on a photo-cathode. Initially, these two bunches are delayed by a few picoseconds, however, two magnetic chicanes compress the peak current of the electron bunches from 20 A to 4 kA such that after the acceleration in the linac a time delay on the ten-femtosecond timescale is achieved. Also after the acceleration stage, the electron bunches also have a difference in kinetic energy, i.e., Lorentz factor,  $\gamma$ . When the electron bunches then travel through the undulator section, both pulses saturate in their lasing process at different colors. For 8.3 keV photons, both pulses combined can reach pulse energies of 1.2 mJ, the color separation is up to 100 eV, and the time separation ranges from  $\Delta t_{\min} = 0$  fs to  $\Delta t_{\max} = 100$  fs. For hard X-rays, this method requires the pump-pulse to have a higher photon energy than the probe-pulse, although their respective intensities may vary. For soft X-rays, the slotted spoiler foil can be used. This enables further control over the electron bunches and allows crossing time zero with both pulses.

## 2.2 Rare-gas clusters

Clusters have a long history as samples to study the light-matter interaction for a few reasons. In general, their characteristics are well known, they can form interesting states, and their use often has practical purposes [70]. Generally speaking, clusters are an aggregation of atoms or molecules and vary in size. Their size ranges from a few atoms to mesoscopic sizes such that one can classify a cluster as a bulk material. Rare-gas clusters are a subclass of clusters and they are bound by van der Waals forces, thus they are normally neutral-charged. Single, solid van der Waals clusters typically form in an icosahedral<sup>7</sup> shape when they are sufficiently small (up to nanometer sized) [71] and have mostly a fcc-crystal<sup>8</sup> structure but exhibit also hcp-crystal<sup>9</sup> structures [72, 73]. In the present work, superfluid helium clusters (or droplets), solid xenon clusters and a mixture of both have been used as samples as they form a finite system that can be produced and tuned in size easily, they have no energy dissipation in surrounding media and can exist in the gas phase. The creation of homogenous and heterogeneous rare-gas clusters is discussed in the next sub-sections.

### 2.2.1 Production of homogenous clusters: The supersonic gas expansion

Rare-gas clusters, for example, xenon clusters, can be generated in a variety of ways. In this thesis experiment, rare-gas clusters are created via supersonic expansion by releasing gas from a reservoir through a nozzle into a vacuum. The gas in the reservoir is at a certain stagnation pressure,  $p_0$ , and temperature,  $T_0$ . Typical values for  $p_0$  are 10 bar, where the mean free path of the atoms is much smaller than the nozzle diameter<sup>10</sup>. This is why many collisions occur in the nozzle during the gas expansion, but collisions do not occur in the free supersonic expansion. The collisions in the nozzle intuitively explain the cluster formation [74], which we will discuss first. We follow the phenomenological discussion with a more detailed description of the supersonic gas expansion and end the section with the empirically derived scaling laws that describe average sizes for rare-gas clusters.

In the nozzle, clusters grow through collisions. The process starts with the formation of a dimer. A dimer can condensate in a three-body collision, where two monomers bind and the third one is usually evaporated removing the excess binding energy. This can be expressed mathematically

<sup>7</sup>An icosahedron is a polyhedron with 20 faces, i.e., a dice with 20 faces.

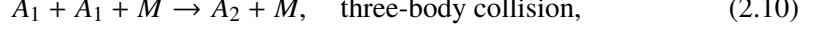
<sup>8</sup>fcc is an acronym for face-centered cubic. A very common crystal structure.

<sup>9</sup>hcp stands for hexagonal close-packed and is also a crystal structure.

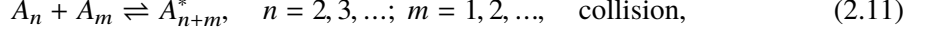
<sup>10</sup>A schematic drawing of the nozzle used in this work can be found in Figure 3.7. See also Equation (2.20) for non-pinhole nozzle openings.

## 2 Fundamental Concepts

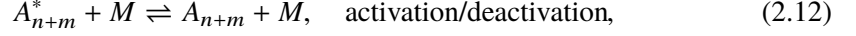
through the following reaction formula,



where  $A_1$  are monomers and  $M$  can be a chaperone of any kind. The subsequent cluster growth can be described mathematically as,



with  $n, m$  denoting the number of monomers assembling body  $A_{n,m}$ . Similar to above, when body  $A_n$  collides with another body  $A_m$  and forms the body  $A_{n+m}^*$ , the new body is in a metastable state that will dissociate if no subsequent collision deactivates it. This can be formulated as



where  $M$  can add or remove energy from the system. One can also say  $M$  activates or deactivates the system. The initial stages of the cluster growth are driven by monomer addition but as more and more clusters are available, cluster-cluster coagulation starts to dominate the later growth process. This is due to the quantitative increase in small clusters in the generation process that then start to collide. From empirical evidence [75, 76], we know that clusters solely generated through monomer addition follow a size distribution of an exponential decay with a rather large decay constant, whereas larger clusters that grew through coagulation follow a log-normal distribution. Here, the density of smaller clusters including monomers and dimers decreases as larger clusters are formed of these particles through coagulation.

During the entire formation process, binding energy is set free that heats the cluster efficiently. In order to lose energy, the cluster typically evaporates monomers. The evaporation process makes the ultimate temperature of the cluster size-independent, after the clusters have reached a certain minimum size [77]. The cluster temperature is heavily dependent on their material, particularly the binding energy. Relevant for this study are the temperature of Xe-cluster<sup>11</sup>, which is  $\sim 75$  K, and the fact that xenon clusters are solid as their melting temperature is higher [78]. For similar reasons, helium-clusters are liquid, which is why they are often called helium droplets. If He-droplets are produced using a cryogenic jet also superfluid helium-droplets can be observed [79].

---

<sup>11</sup>To put this temperature in perspective, krypton clusters have a temperature of  $\sim 50$  K and argon clusters  $\sim 40$  K, when they are created through a supersonic jet expansion, with a certain flight distance, and have a minimum size of 800 atoms [77, 78].

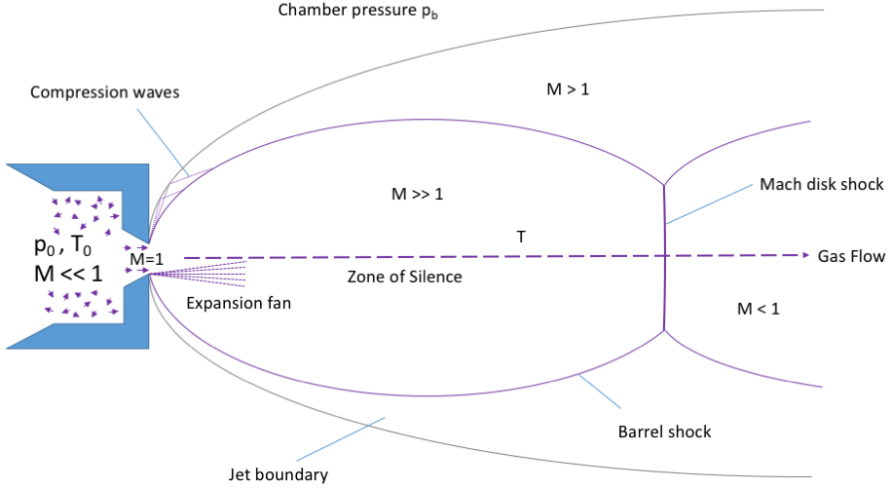


Figure 2.9: Schematic of a supersonic gas expansion into the vacuum. The gas is stored in a reservoir at pressure  $p_0$ , temperature  $T_0$ , and the speed of the gas is thermally distributed ( $M \ll 1$ ). As the gas enters the nozzle area, it is accelerated to the speed of sound ( $M = 1$ ) and as the gas expands, the temperature  $T$  drops altering the speed of sound such that the gas now travels supersonically ( $M \gg 1$ ). After [80].

To discuss the supersonic expansion in detail, we assume an ideal gas and say that turbulence and the effects of heat conduction are unimportant [70, 81]. Figure 2.9 shows a schematic drawing of this process. In the reservoir, the velocity distribution of the gas is thermally distributed at a set temperature  $T_0$ . The movement direction of each atom is randomly orientated. For an ideal gas, we can define the enthalpy,  $H_0$ , in the stagnation chamber by

$$H_0 = C_P T_0. \quad (2.13)$$

The expansion of the gas through the nozzle is driven by the pressure ratio  $p_b/p_0$ . Only when the ratio exceeds a critical value,  $G$ , the expansion will be supersonic. We note,  $G \equiv ((\gamma + 1)/2)^{\gamma/(\gamma-1)}$ , where  $\gamma$  is the ratio of specific heats,  $\gamma = C_P/C_V$ , at constant pressure,  $C_P$ , and volume  $C_V$ .  $\gamma$  can be regarded as independent of temperature for atomic gases. In the nozzle, the steady gas flow becomes directed and the enthalpy,  $H_0$ , is converted into kinetic energy,  $\frac{1}{2}m_{gas}v^2$ , and a remaining enthalpy,  $H$ . We can use the conservation of energy and Equation (2.13) to write down

$$H_0 = H + \frac{1}{2}m_{gas}v^2 = C_P T + \frac{1}{2}m_{gas}v^2, \quad (2.14)$$

with  $T$  being the local temperature along the gas flow and  $m_{gas}$  the atomic mass of the gas. To simplify, let us define the Mach number,  $M \equiv v/c_s$ , as the ratio of the stream velocity,  $v$ , and the

## 2 Fundamental Concepts

local speed of sound,  $c_s$ . We can express the local speed of sound as

$$c_s = \sqrt{\frac{\gamma k_B T}{m_{gas}}}, \quad (2.15)$$

where  $k_B$  is the Boltzmann constant and we can rearrange Equation (2.14) to

$$T = T_0 \left(1 + \frac{1}{2} (\gamma - 1) M^2\right)^{-1}. \quad (2.16)$$

Here, the interplay between the Mach number and the local temperature give insight into the directed mass flow versus the remaining thermal energy in the system. As indicated in the Figure 2.9,  $M$  increases dramatically along the indicated gas flow direction and that is due to a decrease in  $c_s$ , which is proportional to  $\sqrt{T}$  as indicated in Equation (2.15). The gas quickly reaches the terminal velocity while the speed of sound is decreasing. We may write the terminal velocity as

$$v_\infty = \sqrt{\frac{2R}{m_{gas}} \left(\frac{\gamma}{\gamma - 1}\right) T_0}, \quad (2.17)$$

with  $R$  being the universal gas constant. The expansion speed of the gas gives the name to such types of gas sources, namely supersonic jets. This equation is also useful to calculate gas or cluster flight times,  $t_{\text{flight}} = \frac{D}{v_\infty}$ , if the distance  $D$  from nozzle to interaction point is known (see Section 3.4.1).

The appearance of the supersonic jet stream (see Figure 2.9) is particularly important for the experimental aspect of delivering the sample to the interaction region. Upon exiting the nozzle, the Mach number increases by a wide margin ( $M \gg 1$ ). This means that the gas travels faster than information in this medium, i.e., the local speed of sound. Here, a zone of silence is formed, where the gas flow is not influenced by other particles or boundary conditions. At the borders of the zone of silence,  $M$  decreases drastically, resulting in dense regions that are called barrel shock to the sides and Mach disk shock downstream the gas flow [80]. For an unhindered transport of the gas and clusters to the interaction region, the interaction region needs to be within the zone of silence. We can express the distance from the nozzle to the Mach disk  $x_{MD}$  through

$$\frac{x_{MD}}{d} = 0.67 \sqrt{\frac{p_0}{p_b}}, \quad (2.18)$$

with the nozzle diameter  $d$ . So, the competing stagnation pressure,  $p_0$ , and the vacuum chamber pressure,  $p_b$ , define the distance of the otherwise static parameters.  $p_b$  needs to be low enough

Helium	Neon	Argon	Krypton	Xenon
3.85	185	1646	2980	5554

Table 2.1: Parameter  $K_{\text{gas}}$  values for rare-gases [82].

to drive the Mach disk downstream of the interaction region. By using skimmers and thereby physically separating the jet expansion into separately pumped compartments, the pressure  $p_b$  can be reduced, hence  $x_{MD}$  increased.

The average cluster size is very much dependent on the gas type, stagnation temperature  $T_0$ , stagnation pressure  $p_0$ , and the nozzle diameter. An empirically found scaling law, named after Hagena [83–85], can be summarized as follows. The Hagena scaling parameter,  $\Gamma^*$ , reads

$$\Gamma^* = K_{\text{gas}} \cdot T_0^{0.25x-1.5} \cdot p_0 \cdot d_{eq}^x \quad [\mu\text{m mbar K}^{-1}], \quad (2.19)$$

with the gas-specific parameter  $K_{\text{gas}}$  that can be found in Table 2.1 for some rare-gases, the gas specific parameter  $x$  that varies between 0.5 and 1 and is 0.85 for all rare-gases, and the equivalent nozzle opening,  $d_{eq}$ , that is  $d_{eq} = d$  for pinhole sources. For conical nozzles,  $d_{eq}$  becomes [86]

$$d_{eq} = d \frac{\tan(\Phi_0)}{\tan(\Phi)} = 0.719 \frac{d}{\tan(\Phi)}, \quad (2.20)$$

where  $\Phi$  is the half-opening angle of the nozzle and  $\Phi_0$  is the half-opening of the free gas expansion.  $\Gamma^*$  allows us to estimate the mean cluster size, i.e., the mean amount of accumulated particles per cluster  $\langle N \rangle$ , via the following cases

- $\Gamma^* < 350$ , no cluster formation is observed;
- $350 < \Gamma^* < 1800$ , in this region  $\langle N \rangle$  reads [87]

$$\langle N \rangle = 38.4 \left( \frac{\Gamma^*}{1000} \right)^{1.64}; \quad (2.21)$$

- after  $1800 < \Gamma^*$ ,  $\langle N \rangle$  is

$$\langle N \rangle = 33.0 \left( \frac{\Gamma^*}{1000} \right)^{2.35}. \quad (2.22)$$

There is a range, where the mean cluster size deviates from Hagena's law [88], and it is the range

## 2 Fundamental Concepts

- $10^4 < \Gamma^* < 10^6$ , where  $\langle N \rangle$  becomes

$$\langle N \rangle = 100 \left( \frac{\Gamma^*}{1000} \right)^{1.8}. \quad (2.23)$$

Note, however, that for larger cluster sizes, the Equation (2.22) becomes true again [89, 90]. The average number of atoms,  $\langle N \rangle$ , which arrange to a cluster, is in this thesis usually expressed as the radius of a cluster,  $r$ . In a good approximation, the number of atoms,  $\langle N \rangle$ , can be expressed as a cluster radius using the atomic Wigner-Seitz radius,  $R_s$ , as follows. The Wigner-Seitz radius can be noted as [79, 91]

$$R_s = \left( \frac{3M}{4\pi \rho N_A} \right)^{\frac{1}{3}}, \quad (2.24)$$

where  $M$  is the molar mass,  $\rho$  is the mass density, and  $N_A$  is the Avogadro number.  $R_s$  is typically given in ångström and using the mass density for superfluid He-droplets,  $R_s^{He} \approx 2.2 \text{ \AA}$  and for solid xenon,  $R_s^{Xe} \approx 1.7 \text{ \AA}$ . The cluster radius,  $r$ , can then be noted as,

$$\langle r \rangle = R_s \langle N \rangle^{\frac{1}{3}}, \quad (2.25)$$

assuming the cluster agglomerates symmetrically in three dimensions.

Experiments using supersonic jets for cluster generation are sometimes performed with pulsed valves to decrease cost and gas load in the overall system. Upon opening and closing of the valve, the gas density can vary. This affects the cluster size and one would expect to see smaller clusters. It has been observed that one finds smaller clusters in the beginning of the pulse but in the afterpulse, one finds giant clusters that exceed the above-described scaling laws due to the effects when closing the valve [92].

Supersonic jets generally create clusters of different sizes. This size distribution is centered around  $\langle N \rangle$  and for solid rare-gas clusters this distribution is a log-normal distribution. The size distribution can be an experimental challenge, especially when size-dependent effects are investigated. Historically, electron diffraction [77, 93] has been used to determine the mean cluster size, mean temperature, and mean geometry. Today, free electron lasers allow the determination of the size of a single cluster through a diffraction image [94], and by measuring enough single clusters, one can reproduce size distributions of a supersonic jet as shown in Figure 5.7.

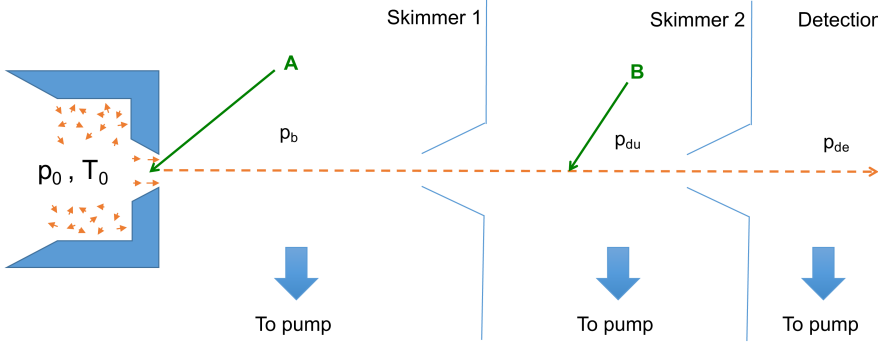


Figure 2.10: Schematic setup to generate heterogeneous clusters through pickup. Thereby is a cluster generated via supersonic gas expansion, which is doped at regions marked A or B. In region A, the dopant gas is mixed in the nozzle such that it becomes part of the nucleus. In region B, the cluster condenses atoms on its surface from the background gas of the chamber with pressure  $p_{du}$ . The cluster can be detected upon evaporation, e.g., due to contact with the chamber, through the pressure  $p_{de}$ . After [70, 95].

### 2.2.2 Creation of heterogeneous clusters: The pickup principle

A possibility to create heterogeneous clusters is through the principle of picking-up atoms or molecules [70]. Figure 2.10 illustrates pickup regions that are typically used in an experiment. Mainly, there are two different places where the cluster encounters a dopant material; one, monomers are added to the cluster in region A of Figure 2.10, which represents the nozzle of a supersonic source and can be achieved by, e.g., co-expanding a gas-mixture; two, they can be picked up by a cluster in region B, for example, through an increased chamber pressure  $p_{du}$  with the dopant material. If clusters encounter atoms or molecules in the nozzle region A, they can become part of the cluster formation and can be found inside of solid clusters [95]. If atoms or molecules are picked up in region B, they typically stick to the surface of solid clusters. If a liquid or superfluid cluster picks up a dopant, it may move within the droplet [96]. Since the traversing cluster in region B is much larger and heavier than a colliding monomer, the trajectory is not affected significantly. Ar-clusters with  $\langle N \rangle = 5.9 \cdot 10^9$  particles can pick-up 0.05 % as many SF<sub>6</sub> molecules with chamber pressures of  $p_{du} = 2 \cdot 10^{-3}$  Pa over a pickup length of a few centimeters [95]. At these low pressures, picking up atoms or molecules in region B requires less gas load on the system but is also less efficient than picking up in region A. To increase the pickup levels in region B, a gas cell with two openings for the cluster beam can be used. The cell contains the gas well and allows higher doping pressures, without putting too much gas-load on the overall system [14]. In this work, gaseous xenon was picked up by superfluid helium droplets in region B using a gas cell.

## 2 Fundamental Concepts

To understand the doping process further, the following considerations are useful. When a cluster and a dopant bond, the binding energy that is specific to the materials is added to the system. This is similar to the cluster growth process itself. The cluster will lose this energy through evaporation of monomers [79]. The loss of particles through evaporative cooling is dependent on the ratio of binding energies of the two materials and can be expressed as

$$N_{\text{Evaporated from cluster}} \approx \frac{\epsilon_{\text{cluster}}}{\epsilon_{\text{dopant}}}, \quad (2.26)$$

with the binding energy of the cluster  $\epsilon_{\text{cluster}}$  and of the dopant  $\epsilon_{\text{dopant}}$ . In this thesis, where a helium droplet is doped with xenon atoms, we may use the binding energies of helium,  $\epsilon_{He} \approx 0.6 \text{ meV}$ , and of xenon,  $\epsilon_{Xe} \approx 0.15 \text{ eV}$  [14, 79], to estimate that approximately 250 helium atoms evaporate by picking up 1 xenon atom.

Now we can extend this idea to estimate the number of picked-up atoms, if we were to know the number of atoms in the cluster before and after the pickup area. An estimate of the initial mean cluster-size, i.e.,  $\langle N_{\text{cluster}} \rangle$ , can be reached through the scaling laws<sup>12</sup> as discussed in Section 2.2.1. An estimate of the cluster size after the pickup can be established through measuring the partial pressure of the cluster material without the pickup,  $p_{de}$ , for example, in the detection chamber when the particle jet hits a wall and evaporates<sup>13</sup> (see Figure 2.10), and the partial pressure with pickup,  $\Delta p_{de}$ . The relative difference  $\frac{\Delta p_{de}}{p_{de}}$  then scales with [14]

$$\langle N_{\text{dopant}} \rangle \approx \frac{\epsilon_{\text{cluster}}}{\epsilon_{\text{dopant}}} \cdot \frac{\Delta p_{de} \langle N_{\text{cluster}} \rangle}{p_{de}}, \quad (2.27)$$

such that the mean amount of picked up atoms,  $\langle N_{\text{dopant}} \rangle$ , can be estimated.

## 2.3 Fundamental processes of soft X-rays and nanoparticles

Nanoparticles respond to intense X-ray radiation by scattering or absorbing the rays [40]. Figure 2.11 shows the most probable processes in the X-ray wavelength range. For soft X-rays, the processes are dominated by the photoionization process and the coherent and elastic scattering. Therefore, Section 2.3.1 discusses photoionization and the resulting core-hole decay processes; Section 2.3.2 discusses the coherent elastic scattering of an electron and extends this concept to the scattering and imaging of a nanoparticle; and Section 2.3.3 generalizes the refractive index. The chapter follows the discussion in Reference [40] and avoids effects that have negligible

---

<sup>12</sup>As already established the actual cluster size produced with a supersonic jet will vary, hence the average cluster size  $\langle N_{\text{cluster}} \rangle$ .

<sup>13</sup>For example with a residual gas analyzer.

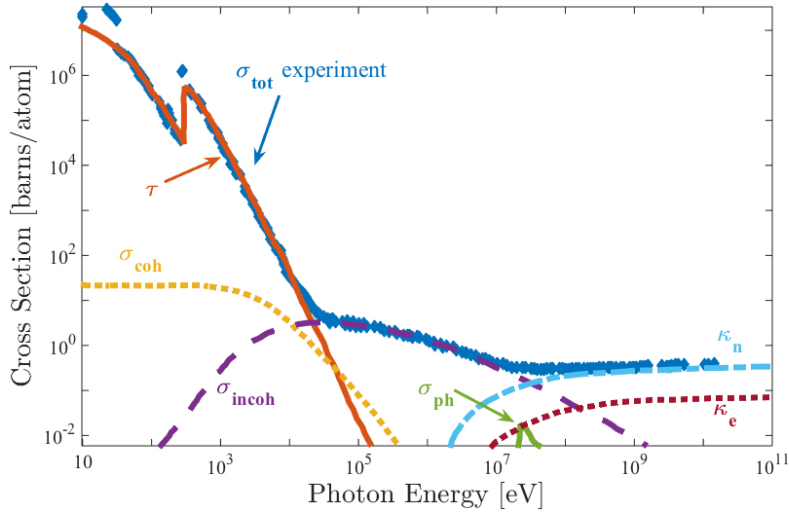


Figure 2.11: The total cross-section of atomic carbon,  $\sigma_{\text{tot}}$ , as a function of energy. Several processes add to,  $\sigma_{\text{tot}}$ :  $\tau$ , is the photoionization;  $\sigma_{\text{coh}}$ , is coherent scattering;  $\sigma_{\text{incoh}}$ , is the incoherent scattering;  $\sigma_{\text{ph}}$ , is photonuclear absorption;  $\kappa_n$ , and  $\kappa_e$ , are pair-production events. At the experimental photon energy of 837 eV, the dominant effects are photoionization and coherent scattering. From [97, 98].

cross-sections, such as the Compton effect, the pair-production, and the scattering from the nucleus.

### 2.3.1 Photoionization and core-hole decay

Given the photon energies of soft X-rays, atoms are typically core-ionized when absorbing a soft X-ray photon, which is depicted in Figure 2.12a) Photoionization. This typically leaves the atom in an excited state. In order to emit energy, the electron core-hole usually decays according to the schematics in Figure 2.12b) Auger decay and c) Fluorescence, whereby the Auger decay is the dominant process for the parameters discussed in this thesis. These processes are discussed in more detail below.

Photoionization is the process where an atom or molecule is transformed into an ion through absorption of a photon and emission of an electron (see Figure 2.12a). Here, the photon energy must be higher than the ionization threshold. Figure 2.13 shows the total absorption cross-sections,  $\tau$ , for xenon and helium for various photon energies.  $\tau$  is strongly dependent on the photon energies as resonant behavior occurs near absorption edges. It is therefore useful to state

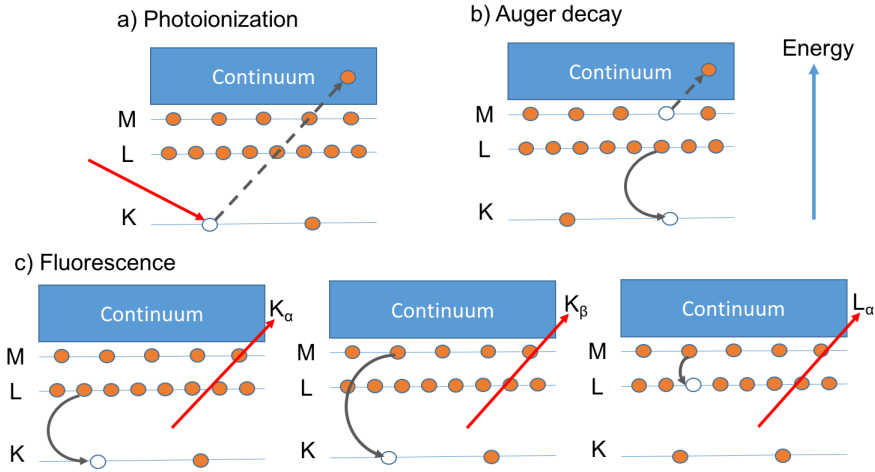


Figure 2.12: Schematic of fundamental light-matter processes. a) Photoionization: Describes a direct emission of a K-shell electron after absorbing an X-ray photon. b) Auger decay: A core-hole decay, where a K-shell hole is filled with an electron from the L-shell and the remaining energy is released through emission of an electron in an outer shell. c) Fluorescence: An electron hole is filled with an electron from an outer shell and the remaining energy is released through photons. After [40].

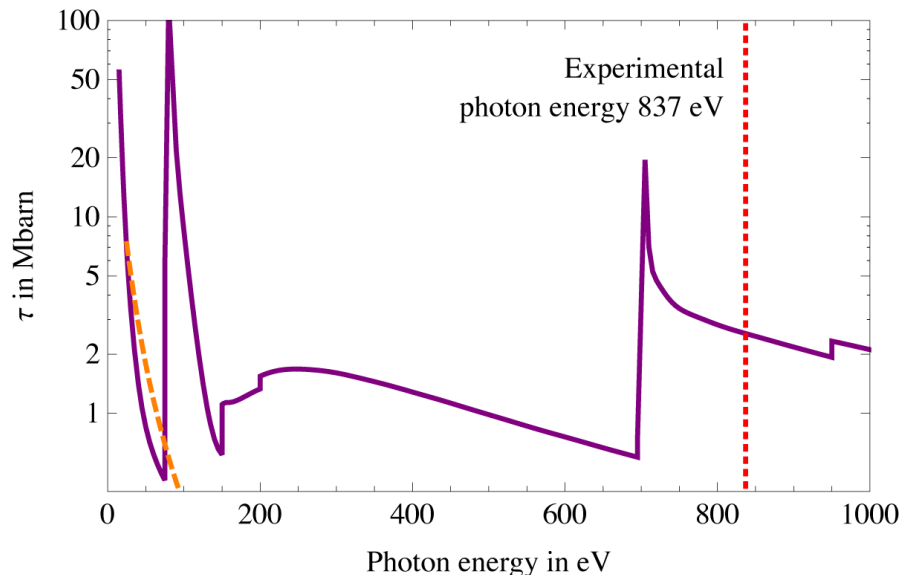


Figure 2.13: Total absorption cross-sections  $\tau$  in megabarn for xenon (purple line) and helium (orange, dashed line). The photon energy of the described experiment is 837 eV (red, dashed line). Data points from [99–101].

### 2.3 Fundamental processes of soft X-rays and nanoparticles

Shell	Subshell	Cross-section in Mb	subshell ionization potential in eV
K	1s	-	34630.0
L	2s	-	5466.4
	2p	-	4899.1
M	3s	-	1153.3
	3p	-	965.4
	3d	2.2505	682.7
N	4s	0.0305	223.7
	4p	0.1247	161.8
	4d	0.2587	68.2
O	5s	0.0040	27.3
	5p	0.0120	12.5

Table 2.2: Subshell absorption cross-sections and ionization potentials for certain electronic configurations of xenon at 837 eV. Calculations performed with [102, 103].

El. Configuration, and ionized subshell	Ionization of subshell	Cross-section $\tau$ in Mbarn	subshell ionization potential in eV
He <sup>+0</sup> , 1s <sup>2</sup>	1s <sup>2</sup>	0.0007	24.4
He <sup>+1</sup> , 1s <sup>1</sup>	1s <sup>1</sup>	0.0005	54.4
Xe <sup>+0</sup> , 5p <sup>6</sup>	3d <sup>10</sup>	2.2505	682.7
Xe <sup>+1</sup> , 3d <sup>9</sup>	3d <sup>9</sup>	2.1487	733.6
Xe <sup>+1</sup> , 5p <sup>5</sup>	3d <sup>10</sup>	2.2443	693.7
Xe <sup>+2</sup> , 5p <sup>4</sup>	3d <sup>10</sup>	2.2390	705.9

Table 2.3: Total absorption cross-sections  $\tau$  and ionization potentials for certain electronic configurations. Calculations performed with [102, 103].

the absorption cross-sections per atomic subshell<sup>14</sup>. Table 2.2 shows the subshell absorption cross-sections and ionization potentials for xenon. If the photon energy is below the ionization threshold of a subshell, this subshell cross-section becomes negligibly small. In this thesis experiment's photon energy of 837 eV, xenon dominantly absorbs photons in the 3d-subshell. After ionization, the electronic structure of an atom changes, which alters ionization energies and absorption cross-sections. Table 2.3 shows total absorption cross-sections for helium and xenon in various electronic configurations. The number of ionization configurations is numerous and the table gives the reader merely an impression of the change for some early ionization steps of helium and xenon in this thesis experiment. The cross-section and ionization potential calculations are performed with the Los Alamos Atomic Physics Codes [102] that are based on

<sup>14</sup>Disregarding the hyperfine structure, which is a shift in atomic energy levels due to interaction of electrons with the nucleus [104].

## 2 Fundamental Concepts

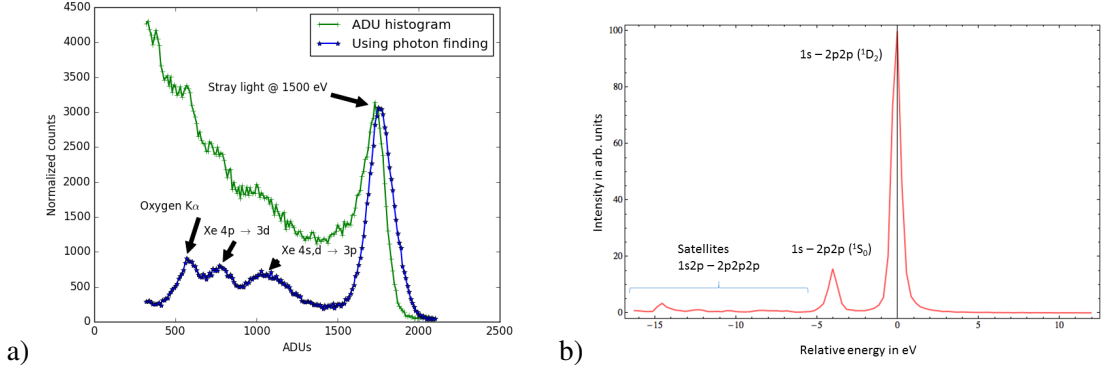


Figure 2.14: a) Fluorescence spectra of xenon and oxygen, which are excited by 1.5 keV photons from the LCLS. The spectra are recorded with pnCCD detectors [105] and the green curve is an ADU histogram of the raw pnCCD image. The blue curve uses a coalescent photon finder [106] and the peaks are identified as in [107]. b) Partial K-LL Auger spectrum with rel. energy 0 corresponding to 804.5 eV. Spectrum is measured with a hemispherical analyzer [56] and the peaks are identified as in [108].

Reference [103].

Far off resonance, the Auger decay is a two-step process (see Figure 2.12b) [109]: one, an outer shell electron is emitted into the continuum, the so-called Auger-electron<sup>15</sup>; two, another electron in the atom simultaneously fills the electron-hole. Auger decay typically occurs on a few femtoseconds timescale after core-ionization [110]. Emitted Auger-electrons have discrete energies depending on the combination of electrons involved in the process. One can use this attribute to, for example, identify elements or calibrate energies. The right panel of Figure 2.14 shows a partial K-LL<sup>16</sup> Auger spectrum from neon illuminated by 1050 eV photons from the LCLS and measured with a hemispherical analyzer [56]. In this example, neon is ionized in the K-shell and an electron-hole in the 1s shell is created. An electron from the L-shell fills the 1s hole and another electron from the L-shell, the Auger electron, is emitted into the continuum. As there are a variety of electronic configurations that can be involved in this process, multiple peaks appear for similar occupation configurations, e.g., 1s - 2p2p. More complex structures, called satellites, appear when the atom is already ionized, for example, when an atom has a hole in the L-shell and photoionization creates another hole in the K-shell, this leads to KL-LLL satellites [109]. Doubly K-ionized atoms will produce so-called hypersatellites [111], which occur in the

<sup>15</sup>Named after the French physicist Pierre Auger.

<sup>16</sup>This nomenclature means a single core-hole in the K-shell decays into two holes in the L-shell.

## 2.3 Fundamental processes of soft X-rays and nanoparticles

intense soft X-ray pulses of LCLS [19, 47]. The transition can also be of the same shell and is then called a Coster-Kronig transition, for example, the N-NN Coster-Kronig transitions in xenon [112].

Fluorescence is the emission of light by a material that has been photoexcited (see Figure 2.12c). If the material is has been core-ionized, the fluorescence decay can result in the emission of X-rays with distinct energies, for example, the for many materials well-known  $K_{\alpha}$ -,  $K_{\beta}$ -, and  $L_{\alpha}$ -lines. These can be used for, e.g., element identification, or chemical analysis. The left panel of Figure 2.14 shows fluorescence peaks that contribute to the background signal when diffraction images are taken with the pnCCD detectors (see Section 3.3). In our case, fluorescence often occurs on the pico- to nanosecond timescale [113] and it is therefore typical that the Auger decay rates beat the fluorescence decay rates [19]. However, the rates vary depending on the material and its electronic configuration such that in intense XFEL pulses these rates are expected to change as the electrons are stripped of the atom [114].

### 2.3.2 From Thomson scattering to diffractive imaging

The elastic scattering of photons off the nanoparticle is discussed in detail below. Let us therefore first consider the elastic scattering of a free electron, or Thomson scattering, as a result of being accelerated in an electro-magnetic field. Then, we use these insights and proceed to the scattering of an atom followed by the scattering of an extended object with a continuous electron density. We end the section with some considerations that are relevant for this work.

Let us introduce the electric field of an incident wave  $E_{in} = E_0 e^{-i\omega t}$  that irradiates an electron. The electron is accelerated in this electric field and emits radiation similarly to a small dipole antenna. We can write this radiated electric field as [40]

$$E_{rad}(R, t) = - \underbrace{\left( \frac{e^2}{4\pi\epsilon_0 mc^2} \right)}_{r_0} E_{in} \frac{e^{ikR}}{R} \cos(\psi), \quad (2.28)$$

with  $k$  being the usual wave-number,  $R$  being the distance from the source of radiation,  $\psi$  being the observation angle, and  $r_0$  being the Thomson scattering length, or the classical electron radius.  $r_0$  can be written in practical units as

$$r_0 = \frac{e^2}{4\pi\epsilon_0 mc^2} = 2.82 \cdot 10^{-5} \text{ Å}, \quad (2.29)$$

## 2 Fundamental Concepts

where  $-e$  is the charge of an radiating electron,  $m$  is the mass of the electron,  $c$  is the speed of light, and  $\epsilon_0$  is the permittivity of free space.

Now we would like to understand the cross-section of this scattering process better. We can establish a differential cross-section,  $\left(\frac{d\sigma}{d\Omega}\right)$ , which follows the same concept of the already discussed example in Equation (2.2). The only difference is that we now consider a scattered intensity,  $I_{sc}$ , of an incident flux,  $(I_0/A_0)$ , into a solid angle,  $\Delta\Omega$ . We may express this as

$$\left(\frac{d\sigma}{d\Omega}\right) = \frac{I_{sc}}{(I_0/A_0)\Delta\Omega} = \frac{|E_{rad}|^2 R^2}{|E_{in}|^2} = r_0^2 \cos^2(\psi), \quad (2.30)$$

which is also called the differential cross-section for Thomson scattering. By integrating over the full angular space, the total cross-section for Thomson scattering,  $\sigma_T$ , results in

$$\sigma_T = \left(\frac{8\pi}{3}\right) r_0^2 = 0.665 \text{ b}. \quad (2.31)$$

We can now move on and use this knowledge for atoms, where we have  $Z$  electrons. To describe electrons in an atom, let us introduce an electron density  $\rho_e(\vec{r})$  that describes the probability density of electrons in an atom. Figure 2.15 illustrates the scattering process by one atom. An incident beam, with wave-vector  $\vec{k}$ , is elastically scattered at the origin, O, into a wave with  $\vec{k}'$  such that  $|\vec{k}| = |\vec{k}'|$ . It is useful to define the wave-vector transfer,  $\vec{Q} = \vec{k} - \vec{k}'$ , which we can write in terms of the scattering angle,  $\Theta$ , as

$$|\vec{Q}| = 2|\vec{k}| \sin\left(\frac{\Theta}{2}\right) = \frac{4\pi}{\lambda} \sin\left(\frac{\Theta}{2}\right), \quad (2.32)$$

where  $\lambda$  is the wavelength of the scattering light.

A volume element  $d\vec{R}$  of the atom at  $\vec{R}$  will now scatter waves proportional to its electron density, which we can express by  $-r_0 \rho(\vec{R}) d\vec{R}$ . At scattering angle  $\Theta = \vec{Q} = 0$ , the atomic scattering factor,  $f^0$ , can be shown to be

$$f^0(\vec{Q} \rightarrow 0) = Z, \quad (2.33)$$

because all scatterers are in phase. As we increase the scattering angle  $\Theta$ , a wave that is scattered at the origin, O, and one at  $\vec{R}$  have an optical path difference of  $2\delta$ . This difference in path length results in a phase difference,  $\Delta\Phi$ , in the wavefront.  $\Delta\Phi$  can be expressed as

$$\Delta\Phi = (\vec{k} - \vec{k}') \cdot \vec{R} = \vec{Q} \cdot \vec{R}. \quad (2.34)$$

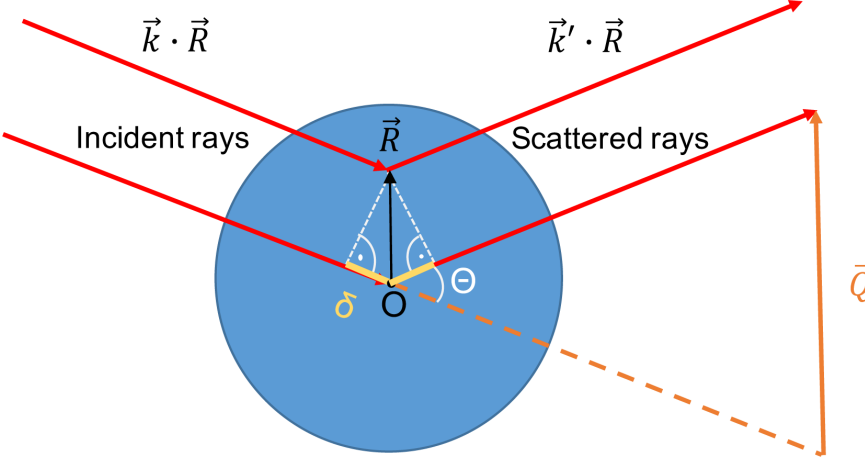


Figure 2.15: Principle of scattering rays of an atom. After [40, 115].

We may multiply a phase factor,  $e^{i\vec{Q} \cdot \vec{R}}$ , to the contribution of the scattered field,  $-r_0 \rho(\vec{R}) d\vec{R}$ , to argue that the volume elements start to scatter out of phase. As a consequence and in the limit of  $\vec{Q} \rightarrow \infty$ , the atomic form factor is thus  $f^0(\vec{Q} \rightarrow \infty) = 0$ . Let us gather these phenomenological arguments, integrate over them to obtain the total scattering volume, and note

$$-r_0 f^0(\vec{Q}) = -r_0 \int \rho_e(\vec{R}) e^{i\vec{Q} \cdot \vec{R}} d\vec{R}. \quad (2.35)$$

This important result is called the atomic form factor and is here written in units of  $-r_0$ . It can be understood as a Fourier transformation of the electron density of an atom.

Let us continue with the scattering of a molecule or cluster that consists of multiple atoms. We can label the atoms in such an object by

$$F^0(\vec{Q}) = \sum_{\vec{R}_j} f_j^0(\vec{Q}) e^{i\vec{Q} \cdot \vec{R}_j}, \quad (2.36)$$

with the atomic form factors  $f_j^0(\vec{Q})$  for the  $j$ 'th atom and call  $F^0$  the single particle structure factor. Similar to above, an electron density can be found for the molecule or cluster by labeling the atoms [116] and for coherent and monochromatic radiation, the scattered amplitude,  $A(\vec{Q})$ , of a nanoparticle can be written in the kinematical approximation<sup>17</sup> as

$$A(\vec{Q}) = \int \rho(\vec{R}) e^{i\vec{Q} \cdot \vec{R}} d\vec{R}, \quad (2.37)$$

---

<sup>17</sup>Sometimes called the weak-scattering limit, where multiple scattering effects are neglected.

## 2 Fundamental Concepts

where  $\rho(\vec{R})$  is the electron density of the scattering nanoparticle. This operation can again be interpreted as a Fourier transformation of the single particle's electron density. But, only scattered intensities can be measured with, e.g., a CCD detector. So, the scattered intensity in a diffraction pattern can be expressed by

$$I_{sc}(\vec{Q}) = I_0 |A(\vec{Q})|^2, \quad (2.38)$$

where  $I_0$  is the intensity of an incident beam<sup>18</sup>. Unfortunately, the operations on the amplitude,  $|A(\vec{Q})|^2$ , eliminate the phase factor, such that merely an inverse Fourier transformation cannot be used to reconstruct the real-space electron density from measured intensities. This is known as the inverse problem and can be solved by iterative phase-retrieval algorithms that we will discuss in Section 4.3.

Let us now make use of above's theory and address the scattering of a rare-gas cluster, as they will reoccur throughout this thesis. We may thus express an electron density of the desired object and Fourier transform it into reciprocal space to understand diffraction patterns better. Due to current resolution limitations<sup>19</sup>, we may approximate the shape of a few nanometer-sized cluster with a sphere. The density,  $\rho$ , of a hard sphere with radius,  $r$ , can be expressed by

$$\rho(\vec{R}) = \begin{cases} \rho & \text{for } r \geq |\vec{R}| \geq 0, \\ 0 & \text{for } r > |\vec{R}|. \end{cases} \quad (2.39)$$

Using this equation, we can solve the integral in Equation (2.37) by making use of spherical coordinates,

$$A_{\text{Sphere}}(\vec{Q}) = \rho \int_0^\pi \int_0^{2\pi} \int_0^r R^2 \sin(\Theta) e^{i|\vec{Q}|R \cos(\Theta)} dR d\Theta d\Phi, \quad (2.40)$$

$$= \frac{4\pi\rho}{|\vec{Q}|^3} \left( \sin(|\vec{Q}|r) - |\vec{Q}|r \cos(|\vec{Q}|r) \right). \quad (2.41)$$

This result can be exploited to determine the size of a spherical particle, i.e., a cluster, using local minima in the diffraction pattern<sup>20</sup> or through a numerical fit of the resulting curve. The envelope function of this curve is the from small-angle scattering well-known Porod's law [117].

---

<sup>18</sup>Here, we make use of the Born approximation and the intensity of the incident beam becomes constant, which holds true in the kinematical approximation

<sup>19</sup>Considering experimental details from Chapter 3

<sup>20</sup>Equation (2.41) can be solved numerically for the distance between the first two minima,  $\vec{Q}_{\min^n}$  and  $\vec{Q}_{\min^{n+1}}$ , such that  $r = \frac{3.24}{\vec{Q}_{\min^{n+1}} - \vec{Q}_{\min^n}}$ .

### 2.3 Fundamental processes of soft X-rays and nanoparticles

El. Configuration, and ionized subshell	Scattering cross-section $\sigma_{\text{coh}}$ in barn
$\text{He}^{+0}, 1s^2$	2.55
$\text{He}^{+1}, 1s^1$	0.65
$\text{Xe}^{+0}, 5p^6$	1874.36
$\text{Xe}^{+1}, 3d^9$	1813.56
$\text{Xe}^{+1}, 5p^5$	1814.68
$\text{Xe}^{+2}, 5p^4$	1754.08

Table 2.4: Atomic scattering cross-sections for certain electronic configurations at 837 eV photon energy. From [118].

For the here discussed spheres, the envelope function is proportional to

$$I(|\vec{Q}| \gg 0) \propto |\vec{Q}|^{-4}, \quad (2.42)$$

and for this thesis very useful in estimating the expected scattering.

The total atomic scattering cross-sections,  $\sigma_{\text{coh}}$ , for helium and xenon in some electron configurations can be found in Table 2.4. The scattering cross-section calculations are based on Equation (2.35) and are  $\sigma_{\text{coh}} = r_0^2 |f^0|^2$  [118]. Xenon atoms scatter dominantly over helium atoms as xenon's scattering cross-section is over 700 times larger than helium's. This means for the diffraction images of mixed HeXe-clusters that xenon atoms contribute as much as helium atoms to the scattering when the doping level is  $\sim 0.14\%$ . Also upon ionization, xenon atoms scatter dominantly. Singly ionized xenon atoms have their scattering cross-section reduced by only  $\sim 3\%$  and singly ionized helium atoms have their scattering cross-section reduced by  $\sim 75\%$  compared to the scattering cross-section of their neutral electron configurations. For the same ionization level in xenon, e.g.,  $Xe^{+1}$ , but different electron configurations, the scattering cross-section varies only on the order of  $\sim 0.05\%$ , which is a small effect compared to the change in the scattering cross-section when xenon becomes increasingly ionized.

#### 2.3.3 Generalized index of refraction

The last section established that an electron was accelerated by a light field and radiated as a result. But, it is not only the light field that drives the electron, also the electron has an effect on the light field. Ultimately, this effect changes how rays scatter off extended objects and therefore our interpretation of recovered real-space electron densities. The atomic form factor can be corrected for these effects with the so-called dispersion corrections. Single particle imaging software suites, such as Condor [119], can make full use of these corrections, which is why

## 2 Fundamental Concepts

the following considerations may be helpful. However, we do not derive this topic to its full extent as it can be found in [120, p. 55 ff], but we qualitatively compare the equation for the complex refractive index,  $n(\omega)$ , to the resonant description of the atomic form factor,  $f(\vec{Q}, \omega)$ . For simplicity, we reduce the following considerations to the case of forward scattering, where  $|\vec{Q}| = \Theta = 0$ .

As a wave propagates through a medium, for example, from air through water, it changes direction according to Snell's law [40]. Here, a medium is attributed a refractive index,

$$n = \frac{c}{v_{\text{phase}}}, \quad (2.43)$$

where  $v_{\text{phase}}$  is the phase velocity that changes inside the material.  $n$  is wavelength dependent and for visible wavelengths, it ranges between 1.2 and 2, which indicates  $v_{\text{phase}} < c$ . X-rays usually have a refractive index of  $n < 1$ . As a result, one usually speaks of a phase advance when an X-ray field traverses an object, for example, a 20 nm thick silicon nitride membrane causes an estimated phase advance of  $20^\circ$  in 32 nm light [12]. Another aspect, when a light wave is traveling through, e.g., from air through water, is the attenuation of the amplitude. When a light wave travels through a medium along the Z-axis, its amplitude is reduced by  $e^{\mu Z/2}$ , with  $\mu$  being the absorption coefficient, for example, the transmission of the 20 nm silicon nitride membrane is 44 % at the wavelength of 32 nm [12]. The amplitude of an electro-magnetic wave that propagates through a medium along the Z-axis with wave number  $k$  and the above considerations can be expressed as [120]

$$e^{inkZ} = \underbrace{e^{ikZ}}_{\text{vacuum propagation}} \underbrace{e^{i(\delta)kZ}}_{\text{phase shift}} \underbrace{e^{-\beta kZ}}_{\text{decay}}, \quad (2.44)$$

where  $n$  is the complex refractive index,  $\delta$  is its real part resulting in a phase shift of the wave, and  $i\beta = i\mu/(2k)$  is the imaginary part resulting in a decline of the amplitude of the wave. The complex refractive index,  $n$ , is thus usually written as

$$n = 1 - \delta + i\beta. \quad (2.45)$$

But, the refractive index can also be written in terms of the atomic form factor. For this, let us imagine electrons in an atom. The electron's response to being driven by a light field is reduced depending on their binding energies. This can be denoted as  $f'$ . The bound electrons can also be photoionized, which can be accounted for by an imaginary factor,  $i f''$ , similar to above. These two resonant effects are called dispersion corrections to the non-resonant atomic

scattering factor,  $f^0$ . Let us include these corrections to the atomic scattering factor and note

$$f(\vec{Q}, \omega) = f^0(\vec{Q}) + f'(\omega) + i f''(\omega). \quad (2.46)$$

Above resonance  $\omega$ , bound electrons can be largely seen as free electrons such that  $f'(\omega) \rightarrow 0$  and  $f''(\omega) \rightarrow 0$ . Close to resonance,  $f'(\omega)$  and  $f''(\omega)$  can become large factors.

We can compare Equation (2.45) to Equation (2.46) and note the complex refractive index through the atomic form factor as [40]

$$n = 1 - \frac{2\pi\rho_{atom}r_0}{k^2} \left( f^0(\vec{Q} = 0) + f'(\omega) + i f''(\omega) \right), \quad (2.47)$$

with the atomic number density,  $\rho_{atom}$ . The real and imaginary parts of the refractive index then read

$$\delta = \frac{2\pi\rho_{atom}r_0}{k^2} \left( f^0(\vec{Q} = 0) + f'(\omega) \right), \quad \text{and} \quad (2.48)$$

$$\beta = - \left( \frac{2\pi\rho_{atom}r_0}{k^2} \right) f''(\omega), \quad (2.49)$$

with

$$f''(\omega) = - \left( \frac{k}{4\pi r_0} \right) \tau, \quad (2.50)$$

where  $\tau$  is the absorption cross-section.

## 2.4 Clusters in intense soft X-ray pulses

The response of a cluster upon irradiation with light often differs from just the atomic response. In the soft X-ray region, the ionization of clusters is initially founded by the ionization of atoms, but the sample environment plays a dominant role in the overall response [22, 121]. As discussed in Section 2.2, clusters have testbed environment properties that allow studying effects ranging from atomic, to molecular, and to bulk material attributes. This is why they are an ideal sample to control light-driven many-particle processes [37]. In Section 2.4.1, we summarize how rare-gas clusters respond to femtosecond long, high-intense X-ray pulses and reflect on recent experiments; Section 2.4.2 discusses how tamper layers slow the nanoplasma expansion.

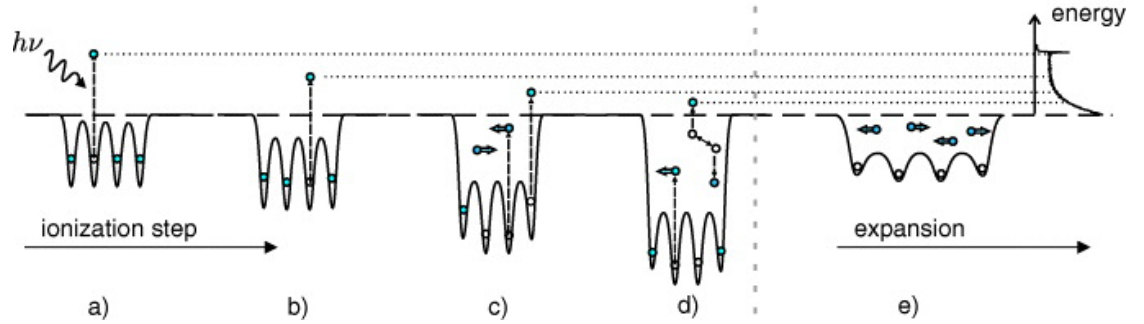


Figure 2.16: Schematic of the nanoplasma formation and expansion. Step a) X-ray photons ionize the atoms of a cluster. b) Subsequent multistep ionizations try to relax the electronically excited system, deepening the Coulomb potential of the cluster. Step c) shows a deepened Coulomb potential of the cluster, due to which the multistep ionization becomes (partially) frustrated and electrons are trapped in the potential. In step d) trapped electrons collide and start to thermalize. Collisions can lead to emission of trapped electrons. e) The superheated nanoplasma starts to expand. From [122].

#### 2.4.1 Formation and expansion of a nanoplasma

When nanoparticles are irradiated with intense soft X-rays, they form a plasma [123]. Due to the finite size of these systems, they are called nanoplasmas. Nanoplasma formation therefore describes the radiation damage processes in typical diffractive imaging experiments. The importance of imaging biological nanoparticles thus lead to much research about nanoplasma in the past [11, 20, 35, 37, 123–125] and is still ongoing. This section first discusses nanoplasma formation and expansion of clusters in intense soft X-rays. The discussion then summarizes recent experiments that study the nanoplasma evolution and some remarks for this thesis are made.

For soft X-rays, nanoplasma formation and expansion of clusters is schematically shown in Figure 2.16. The following steps describe it in more detail [122, 124]: Step a) the cluster is strongly ionized. Step b), further ionization through emission of photo electrons and Auger electrons lead to a multistep ionization that deepens the Coulomb potential [126–128]. Step c), the multistep ionization is suppressed or, so-called, frustrated because the Coulomb potential depth is larger than the excess energies of photo- and Auger electrons. The emitted electrons are now trapped in the cluster potential and are quasi-free. As a result, the cluster forms a nanoplasma<sup>21</sup>. Step d), the kinetic energies of the trapped electrons is initially defined by the discrete excess energies of,

---

<sup>21</sup>Plasma is another state of matter, similar to solid, liquid and gaseous, where molecular bonds dissociate and positive and negative particles are present in increasing numbers.

e.g., the Auger electrons, but collisions with other particles lead to a kinetic energy distribution that is similar to thermal distributions and can be measured via the spectra of emitted electrons [129, 130]. Step e) An hydrodynamic expansion and Coulomb explosion are the key mechanisms that now drive an expansion of the cluster until the cluster ultimately disintegrates.

Both expansion mechanisms reasonably describe the expansion process, are not mutually exclusive, and mostly depend on sample size and irradiation technique. Regarding the sample size, large clusters tend to efficiently trap electrons in their deep Coulomb potentials that thermalize efficiently, which leads to an expansion that is rather driven by hydrodynamic forces due to comparably high electron temperatures. It has been shown that electrons thermalize on the femto- to attosecond timescale and that the energy transfer to the ions can be as fast as 50 fs [91]. Small clusters trap photo- and Auger-electrons less efficiently and electrons are free such that the heating process is suppressed. In this case, the ions see the repelling force due to Coulomb interaction of like charges [131].

The nanoplasma formation is dependent on the wavelength that excites the cluster. We focus here on the soft X-ray wavelength range but to give an idea of wavelength dependent aspects in the nanoplasma formation the following can be said. For optical to ultraviolet (UV) pulses, strong field ionization can lead to ionization of clusters and a subsequent nanoplasma expansion [132]. In the vacuum-ultraviolet (VUV) range, inverse *Bremstrahlung* heating leads to efficient energy absorption in clusters and the ionization is driven by collisions inside the strongly coupled plasma [126]. In the extreme-ultraviolet (XUV) to soft X-ray range, direct photoionization and subsequent multistep ionization become the main driver of the ionization, as described above.

The sample damage due to the nanoplasma formation can be divided into two related aspects [27, 133]: One, electronic damage; the electronic configuration of a sample changes inevitably due to photoionization and subsequent processes, which is expected to break bonds and change scattering factors; this limits the ultimately achievable resolution from diffraction imaging. Two, structural damage; the nanoplasma expansion leads to structural changes due to the movement of nuclei [18]. As these damage aspects are very related, we will refer to them merely as sample- or radiation damage in this thesis. It is currently an active field to investigate these damage processes and determine particularly the timescales of these damage processes, the effect on the measured signal, and the actual structural changes [20]. Initial experiments aimed to reveal correlations between diffraction images and ion spectroscopic data using a coincident imaging and spectroscopy technique [52, 134].

## 2 Fundamental Concepts

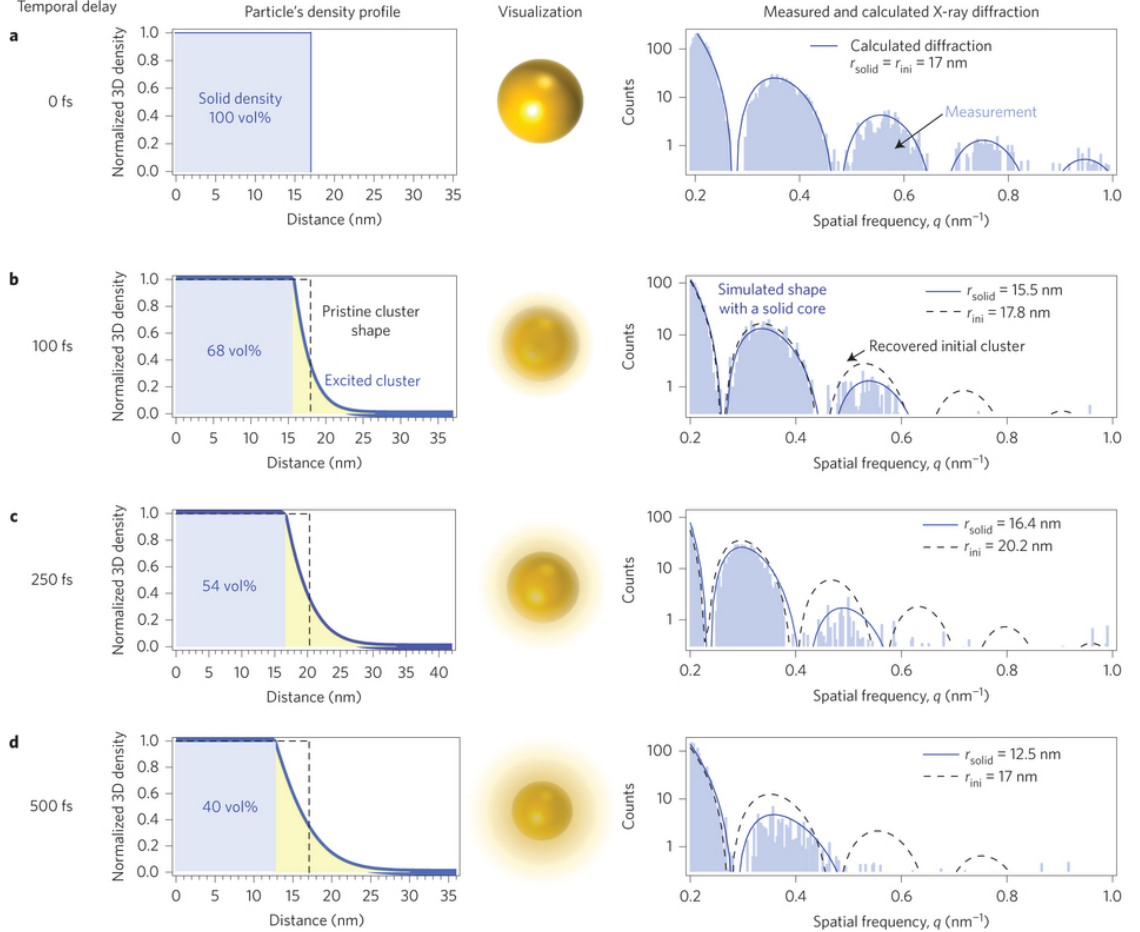


Figure 2.17: Xe-clusters after being pumped with a NIR laser pulse and probed at a certain time delay (indicated left) with a LCLS pulse. Left series, simulation of electron densities. Right series, measured diffraction patterns. The diffraction patterns show a decrease in intensity at larger  $q$  values, when the delay is increased. This can be explained through expanding electron densities, i.e., a surface softening. Fourier transformation of electron densities are fitted to the measurement for a solid sphere (dashed line) and an expanding sphere (solid line). From [21]. Reprinted with permission from Nature Publishing Group.

## 2.4 Clusters in intense soft X-ray pulses

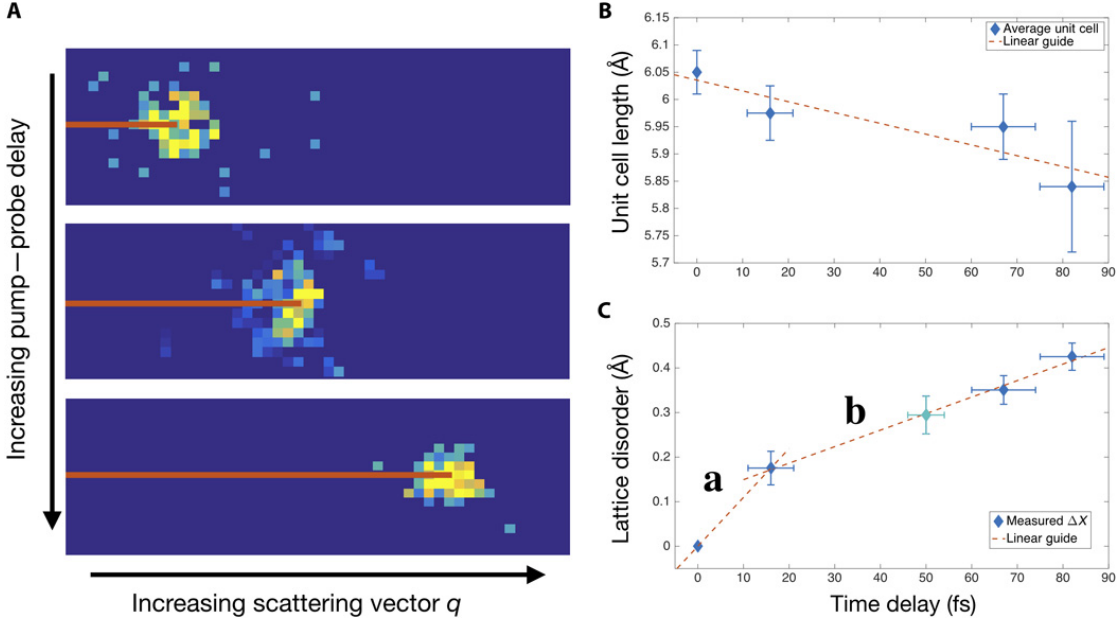


Figure 2.18: X-ray pump–X-ray probe scattering experiment on Xe-clusters that shows an early evolution of the nanoplasma transition. **A**, single-shot Bragg peaks at varying time delays. The scattering vector  $q$  increases over time delay. **B**, unit cell length over time delay. The clusters exhibit a transient lattice compression. **C**, Lattice disorder over time delay. The measured fcc lattice is becoming disordered after being pumped with an X-ray pulse. From [22]. Reprinted with permission from AAAS.

With the advent of ultrafast pump–probe techniques at XFELs, the nanoplasma expansion could be initiated in a controlled way using the pump-pulse, while the probe-pulse creates a snapshot of the nanoplasma formation and expansion. A first experiment used an infra-red-pump and soft X-ray FEL-probe pulse to study the nanoplasma expansion [21, 135]. Figure 2.17 shows diffraction images of Xe-clusters from this study. The diffraction images have been modeled with Fourier-transformed electron densities. As the time delay,  $\Delta t$ , between pump- and probe-pulse is varied on the hundred femtoseconds timescale, the diffraction images of the (15 to 20) nm radius Xe-cluster show declining intensities at larger spatial frequencies,  $q$ . The loss in signal could be explained through a surface softening of the electron density [125, 136]. This means for the nanoplasma expansion that initially the outer atomic layers of a Xe-cluster expand, and only at longer time delays inner atomic layers begin to expand. It remains a question however, whether the nanoplasma responds similarly to an X-ray induced formation.

So, an X-ray pump–X-ray probe study at 8.3 keV using the technique described in Section 2.1.4 followed at a later time [22]. Here, a coincident measurement of Bragg powder patterns and

## 2 Fundamental Concepts

ion spectroscopy data was performed and time delays up to  $\Delta t < 100$  fs could be observed. Figure 2.18A shows the measured Bragg peaks of Xe-clusters as a function of  $\Delta t$ . The analyzed signal shows that the unit cell length shrinks over the time delay range  $\Delta t = (0 \text{ to } 80)$  fs, which means that the cluster undergoes a transient lattice compression before it begins the nanoplasma expansion. This unintuitive and contradictory result is attributed to the changes in electronic configuration upon ionization. Quasi-free electrons that are trapped in the cluster's Coulomb potential have an increased mobility. These electrons act like delocalized valence electrons that change the cluster's weak van der Waals bonds to a more "metallic-like" state. The change in bond character changes the bond length. Due to the limitations in the time delay, it could not be determined, whether the transient lattice compression is followed immediately by a nanoplasma expansion.

Part of this thesis is to build on and complement the results of the above studies (see Section 5.2.1). The used X-ray pump–X-ray probe method in this thesis (see Section 2.1.4) has similar parameters to current bio-molecule imaging setups such that a nanoplasma formation and expansion can be observed under the conditions of typical single molecule imaging experiments. The pump-pulse has intensities of  $\sim 2 \cdot 10^{16} \text{ W cm}^{-2}$  and the probe-pulse  $\sim 2 \cdot 10^{17} \text{ W cm}^{-2}$ . Here, radiation damage remains a major challenge and is expected to limit maximum achievable resolutions [25]. Furthermore, the pump–probe method of this thesis experiment allows a time delay range from  $\Delta t = (0 \text{ to } 800)$  fs, thus extending the time delay window of above's X-ray pump–X-ray probe study.

### 2.4.2 Sacrificial layers slow the nanoplasma expansion

As we have discussed in the last section, radiation damage occurs as the nanoparticle is exposed to the light pulse. Radiation damage is visible in diffraction patterns when the imaging pulse durations are comparable to Auger decay rates. Thus, the principle of diffraction before destruction [18] demands stringent light source parameters to image a nanoparticle before structural damage, namely X-ray fluences of ( $10^{13}$  to  $10^{15}$ ) photons  $\mu\text{m}^{-2}$  and pulse lengths of a few femtoseconds or shorter [24]. But, these parameters are likely not achievable with the currently planned XFEL light sources [23]. There have been several proposals to reduce the requirements to light sources [25] by either reducing or accounting for the effects of radiation damage. Here are three promising candidates listed: One, radiation damage effects can - in principle - be accounted for by computer models using, e.g., atomistic cross-section calculations for small biological molecules [26–28]. Two, single particles can be aligned prior to the imaging process [24] and the known orientation of a reproducible nanoparticle in a 2D projection, i.e., the diffraction image, allows, for example, the averaging of multiple diffraction images; molecule alignment has seen some

success for small molecules [137], but it is currently unknown, whether this is applicable for larger molecules. The strong light fields that are needed to align the molecules, may change the molecule's structure. Three, nanoparticles or biological molecules can be encapsulated with sacrificial layers [30–32], which slow the progress of the nanoplasma expansion. The tamper supplies the imaged nanoparticle with electrons and the ionized tamper is sacrificed to delay sample damage. This allows longer light pulses to perform the diffractive imaging (see Figure 1.2 and the left panel of 2.19). Part of this thesis is to investigate the physics of sacrificial layers, which is why this is discussed in more detail below.

Initially water has been proposed as tamper layer material for biological particles [30, 31], but recent discussions [25] suggest that tamper layers of water tend to become uneven in thicker layers. The water layers are usually not uniform around the sample due to a mix of hydrophobic and hydrophilic surfaces on typical biological particles. It is important to have a uniform and thin tamper layer to cope with the contributions from the layer to the diffraction image. These contributions can be reduced by averaging multiple diffraction patterns and removing the average contributions from the layer [30, 138]. For the averaging of the diffraction images, the orientation of the nanoparticle needs to be accounted. Tamper layers have been used at FLASH using fixed targets that were mounted on a stage as a sample [33]. Here, a silicon tamper layer was placed around an aluminum pillar and compared to an aluminum pillar without a tamper layer (see Figure 1.2). The effects of the sacrificial layers were immediately obvious and the tamper ensured the sample integrity over a period of at least 5 ps after the irradiation with a 25 fs-long 13.5 nm FLASH pulse.

Another study [34] that is very close to the idea of tamper layers and the work described in this thesis is shown in the right panel of Figure 2.19. Here pristine Ar- and Xe- clusters as well as heterogeneous ArXe-clusters were investigated. The two rare-gases form a core–shell system, whereby the cluster's core consists of Xe-atoms and the shell is built of Ar-atoms. The clusters were irradiated with 93 eV photons from FLASH to undergo a nanoplasma formation and expansion. At this photon energy, dominantly xenon atoms are ionized. Figure 2.19b shows time-of-flight (TOF) mass spectra that are explained in more detail in Section 3.5. The top panel of Figure 2.19b shows TOF traces of small ArXe-clusters with  $\langle N \rangle = 400$ , where mostly Ar- and Xe-ions are measured. The bottom panel of Figure 2.19b shows TOF traces of larger ArXe-clusters with  $\langle N \rangle = 4000$ , where the Xe-ion count is significantly reduced. The data also indicates that argon atoms in the large cluster case release more kinetic energy than in the small cluster case. As we have discussed in Section 2.4.1, larger clusters trap electrons efficiently in their deep Coulomb potential. These trapped electrons are available for recombination [34,

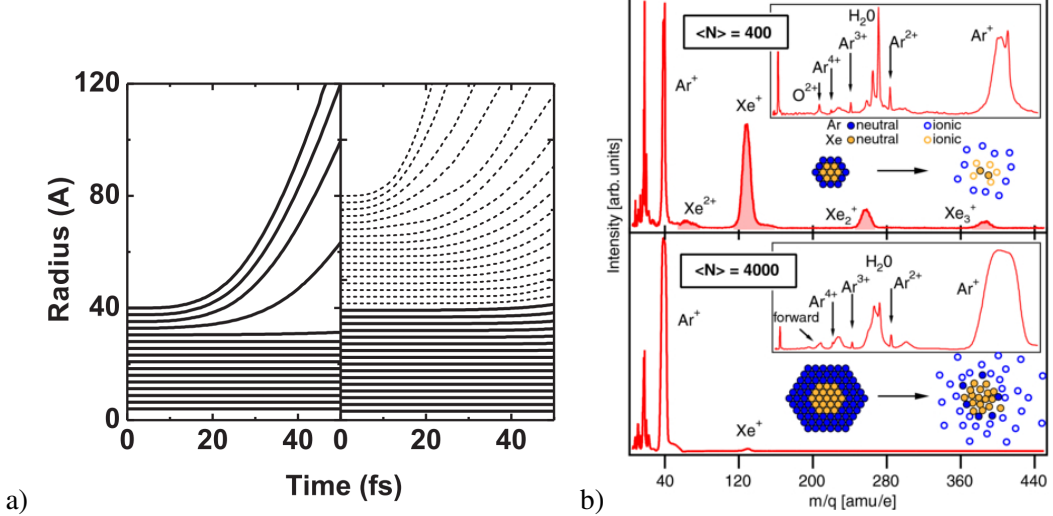


Figure 2.19: a) Simulation of atomic layers of a nanoparticle that undergoes a nanoplasma formation without tamper layers (left) and with tamper layers (right, tamper dashed line). From [30]. Reprinted with permission from APS. b) TOF traces of ArXe-cluster of different sizes,  $\langle N \rangle$ . Insets show  $m/q < 40$ . From [34].

37, 139] with other ionized atoms in the cluster. This is what the large ArXe-clusters TOF data indicates, here Xe-ions recombine with electrons that were attracted to the center of the core–shell system due to the deep Coulomb potential. Neutral xenon atoms are not detected by the TOF detector. The Ar-atoms in the outer shell are therefore charge-transfer ionized and this tamper layer is then shed off (sacrificed) by the mixed ArXe-cluster.

These are promising results that sacrificial layers slow the nanoplasma formation and expansion of nanoparticles that are exposed to highly intense X-ray pulses. While the underlying processes of a tamper layer are more and more understood and its application for diffractive imaging is demanded [25], experiments have not yet produced data that comes close to the conditions of typical diffractive imaging setups at XFELs. Here nanoparticles are typically injected using gas or aerosol jets to take diffraction images at high rates. The sample injection then poses the question, which tamper material should be used and how it can be placed reproducibly around a nanoparticle?

Helium droplets have a long tradition for studies of embedded species due to the unique attributes of the quantum fluid [14, 140–143]. About a decade ago, heterogeneous HeXe-clusters were studied theoretically as a core–shell system [35] and it was proposed to use helium tamper layers to slow and reduce the effects of a nanoplasma formation and expansion upon irradiation with

an XFEL.

This thesis investigates HeXe-clusters experimentally using the previously mentioned X-ray multipulse operations at LCLS (see Section 2.1.4) and a coincident measurement of diffraction images and TOF mass spectra (see Chapter 3). The data is analyzed using, for example, iterative phase-retrieval algorithms that reveal the first real-space reconstructions of rare-gas clusters (see Chapter 4). We find evidence in HeXe-clusters that the He-shell acts as a sacrificial layer, which is discussed further in Chapter 5.



## 3 Experimental Considerations

The experiment described in the present thesis has been performed using the LAMP end-station of the Atomic, Molecular and Optical (AMO) Physics instrument of the Linac Coherent Light Source, which is located at SLAC National Accelerator Laboratory. SLAC was founded in 1962 as the Stanford Linear Accelerator Center. The linear accelerator was early on used for high-energy physics experiments, which resulted in three Nobel Prizes in Physics [144–146]. SLAC’s research topics broadened in the 1970’s and with the Stanford Synchrotron Radiation Project, it became an X-ray user facility in 1974. Meanwhile, the synchrotron source was modernized and is now known as the Stanford Synchrotron Radiation Light-source (SSRL) and the linear accelerator was repurposed to function as the world’s first hard X-ray free electron laser - the LCLS. The LCLS began operations in April 2009 [9] and the AMO instrument started user operations in October 2009 [147]. AMO began operations with the High-Field Physics (HFP) and the CFEL<sup>1</sup>-ASG<sup>2</sup> Multi Purpose (CAMP) end-station, which was supplied by the Max-Planck Society from Germany. The so-called “LAMP” end-station is a successor of the CAMP end-station and was commissioned in September 2013 [10]. LAMP has been in use at the AMO instrument since commissioning and the experiment described in this thesis was performed in January 2014<sup>3</sup> in the LAMP end-station of the AMO instrument. My involvements in design discussions, the building, the commissioning, and the operation of the LAMP end-station were a significant effort during my doctoral studies and resulted - at the time of writing - in the publications [10, 50, 63, 148–153].

This chapter is organized as follows: Section 3.1 discusses the beam transport from the undulators to the LAMP end-station; Section 3.2 focuses on the specifics of the LAMP end-station; Section 3.3 goes over the pnCCD X-ray pixel detector and its geometry; Section 3.4 centers around relevant aspects of the sample delivery; Section 3.5 describes the time-of-flight (TOF) spectrometer for the LAMP end-station; and Section 3.6 goes over aspects of the here used X-ray focus characterizations.

---

<sup>1</sup>Acronym for the Center for Free Electron Laser Science on the DESY campus in Hamburg, Germany.

<sup>2</sup>Short for the Advanced Study Group of the Max Planck Society in Hamburg, Germany.

<sup>3</sup>Experimental identifier at SLAC: AMOA1214

### 3 Experimental Considerations

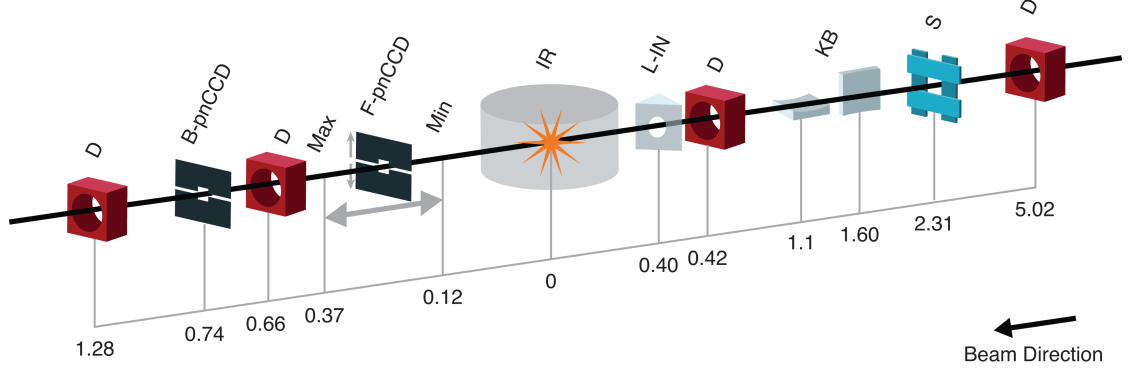


Figure 3.1: Schematic overview of the AMO beamline instrumentation in the LAMP configuration. The indicated distances below the schematic items are in meters from the interaction region (IR). As the X-ray beam enters the instrument, it can be visualized on a YAG crystal diagnostics (D). A set of 2 slits (S) cuts the beam in the vertical and horizontal to reduce straylight from the Kirkpatrick-Baez (KB) optics. The differential pumping section of the LAMP end-station houses an option to couple-in an optical laser (L-IN). The front and back pnCCD (F/B-pnCCD) are located downstream of the IR. From [10].

## 3.1 The X-ray beam transport to the LAMP end-station

The AMO instrument is located closest to the undulators of the LCLS at hutch 1. It is designed for soft X-ray photons in the energy range from (280 to 2000) eV [10, 154], where the beam divergence is a limiting factor for lower energies and the boron carbide ( $B_4C$ )-coating on the mirrors leads to absorption above 2000 eV [154]. After the X-ray pulse generation in the undulators of the LCLS, the X-rays are separated from the electron bunch using magnets, and optionally, the X-band transverse deflecting structure (XTCAV) [155] can be used to give insight into the kinetic energy and pulse duration of the electron bunch. Prior to entering the Front End Enclosure (FEE) [156], the electron beam is discarded in the electron dump such that only X-rays continue. In the FEE, the X-rays can be attenuated with either gas or solid attenuators. An X-ray pulse energy monitor, often referred to as a gas detector, measures the pulse energy of a single-shot before and after attenuation [157]. Eventually, the X-ray beam is deflected through a mirror system into the desired hutch. To direct the beam to the AMO hutch, the soft X-ray offset mirrors (SOMS) are used. The SOMS are a set of four mirrors, where the first two deflect the X-rays to the LCLS instruments that use soft X-rays, namely the AMO and the Soft X-ray (SXR) instrument [158–160]. The third SOMS mirror is a double mirror that either deflects the beam into the AMO or SXR instrument. The AMO instrument is versatile in its configuration and four different end-stations have been used so far. In historic order: one, the HFP end-station [147,

### 3.1 The X-ray beam transport to the LAMP end-station

154]; two, the diagnostics (DIA) end-station [147]; three, CAMP end-station [161]; and four, the LAMP end-station [10, 105]. Today, the HFP and LAMP end-station can be combined with additional instrumentation, for example, the modernized DIA end-station or the XRSD device (see Section 2.1.4). As the experiment described in the present work has been performed with the LAMP end-station, we shall focus on that AMO configuration from here on.

A schematic overview of the AMO beamline instrumentation in the LAMP configuration can be found in Figure 3.1. As the X-ray beam travels from the FEE to the AMO beamline, it can be viewed with a YAG crystal diagnostic viewer (D). Here the shape and position of the beam can be determined as it is several meters downstream of the SOMS such that a difference of the SOMS angle and position can be determined with sub-millimeter precision. This also reveals the alignment of the beam with respect to several differential pumping apertures that are located in the FEE. Experience shows that the X-rays should be centered to those apertures [162]. This diagnostic viewer is also useful to detect and correct for an unstable X-ray beam or erratic beam pointing. A beamline alignment laser, which is a typical HeNe-laser with low beam divergence, can be coupled into the beamline slightly downstream of the YAG screen<sup>4</sup> such that it co-propagates with the X-rays. The X-ray beam then travels through a set of four blades (S), which are often referred to as 4 Jaw slits that can be moved independently to cut into the beam and reduce parasitic scattering<sup>5</sup> originating from the Kirkpatrick-Baez (KB-)mirrors [163]. Experience shows that the blades should not cut into the main intensity profile of the beam but rather conservatively cut into the halo of the beam. This sufficiently reduces parasitic scattering but does not significantly reduce the peak intensity of the X-ray pulse (compare green and blue curve in Figure 3.12).

The KB-mirrors are a set of two concave mirrors that focus the X-ray beam into the interaction region [147]. The mirrors consist of two 400 mm long silicon (Si) substrates that are coated with boron carbide. They reflect the X-rays in grazing incidence at 13.85 mrad and are sometimes referred to as KB-optics. The first mirror focuses the beam in the horizontal and the second mirror focuses the beam in the vertical. As the mirrors are located at different positions in the horizontal and vertical, they are designed to have a focal length of 1600 mm in the horizontal and 1100 mm in the vertical. Additionally, the mirrors can be bent to change their focusing position along the Z-axis<sup>6</sup> and the optimal focus can be found and characterized by, for example, studying time-of-flight spectra [105] and analyzing imprints [164, 165], which we will discuss in Section

---

<sup>4</sup>Not shown in Figure 3.1

<sup>5</sup>Parasitic scattering is often referred to as stray light.

<sup>6</sup>The LCLS uses a right-handed coordinate system, where the index finger (*Y*-axis) points up and the middle finger (*Z*-axis) points colinear to the X-ray beam.

### 3 Experimental Considerations

	pump beam	probe beam
wavelength		1.5 nm
mean pulse energy	(80 to 100) $\mu$ J	(0.8 to 1) mJ
X-ray beam FWHM		$\sim$ 1.5 $\mu$ m
pulse duration		$\sim$ 25 fs
delay $\Delta t$ precision		<1 fs

Table 3.1: Summary of LCLS beam parameters during experiment.

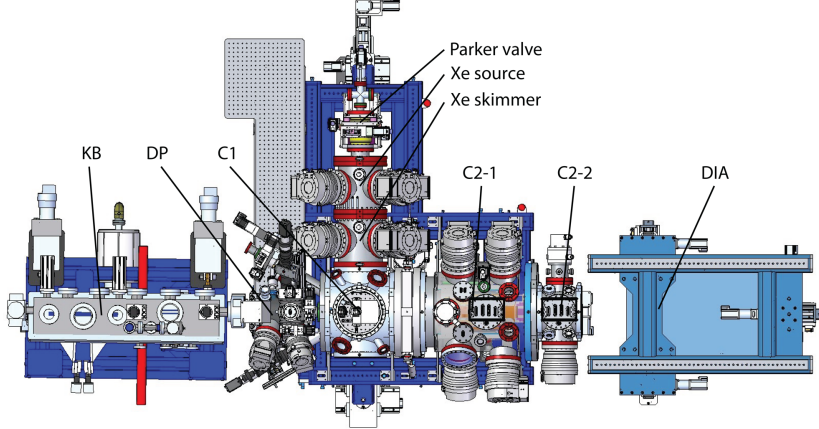


Figure 3.2: Overview of the AMO instrument in the LAMP end-station standard configuration. From left to right, the beam propagates through the Kirkpatrick-Baez (KB) optics, the differential pumping (DP) section, the interaction chamber (C1), the front pnCCD chamber (C2-1), the rear pnCCD chamber (C2-2) and finally the diagnostics (DIA) stand. The Xe jet is also shown, including the Parker valve, Xe-source and -skimmer chamber, which are mounted on C1.

3.6. A study of the X-ray focus is necessary to achieve the smallest focus, thereby increasing the intensities at the sample interaction region. For the experiment in this thesis, the X-ray beam focal size was determined to be  $\text{FWHM} \approx 1.5 \mu\text{m}$ , with an effective area of  $5 \mu\text{m}^2$  [105]. The LCLS beam parameters are summarized in Table 3.1. The pulse duration was determined through analysis of the electron beam and the delay,  $\Delta t$ , precision is estimated from geometric considerations of the delay chicane (see Section 2.1.4).

## 3.2 The LAMP end-station at the AMO instrument

After the KB-mirrors, the X-ray beam enters the LAMP end-station, which is indicated in the beamline schematic of the AMO instrument in Figure 3.1 and the overview of the AMO

### 3.2 The LAMP end-station at the AMO instrument

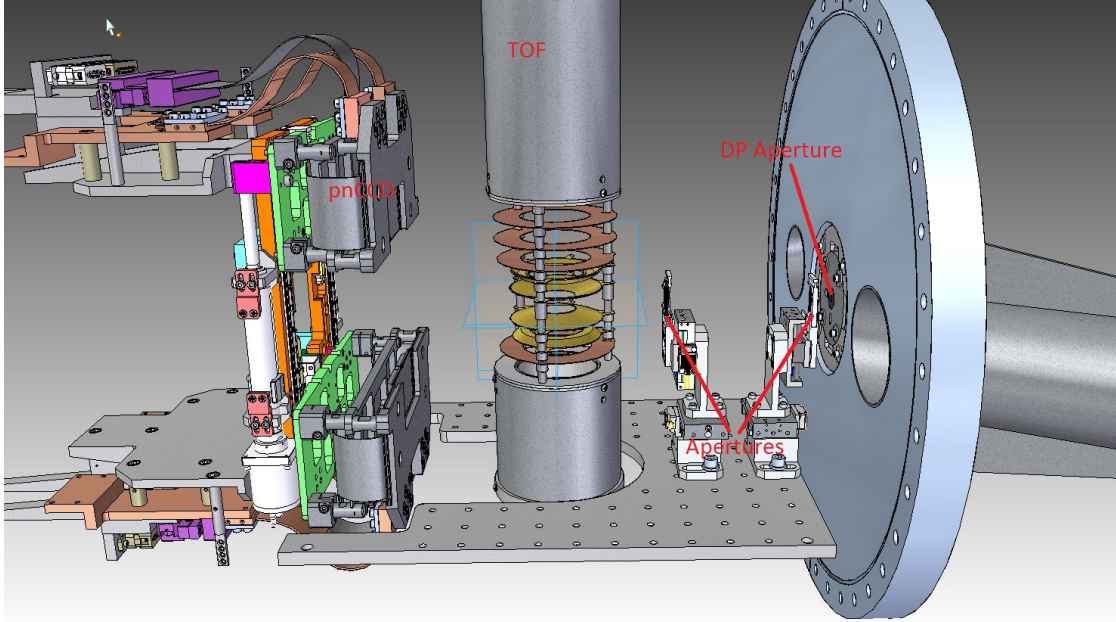


Figure 3.3: Inside view of the C1 chamber showcasing the interaction region.

instrument in Figure 3.2. LAMP begins with a differential pumping (DP) section that separates the interaction (C1) and detector chambers (C2-1, C2-2) from the KB optics and other upstream beamline instrumentation. The differential pumping section consists of two small tubes, which are pumped with turbo-molecular pumps at neighboring chambers. The tubes are 5 mm, 8 mm, or 10 mm diameter differential pumping apertures that are indicated in Figure 3.3 and are exchangeable. The DP stage is able to maintain over 4 orders of magnitude pressure difference, for example, the pressure in the C1 vacuum chamber,  $p_{C1}$ , may rise to  $p_{C1} = 10^{-6}$  kPa due to the sample injection, but the pressure in the KB-optics vacuum tank,  $p_{KB}$ , is maintained at  $p_{KB} = 10^{-10}$  kPa due to the differential pumping section. The second DP-stage chamber holds a YAG crystal to examine the X-ray beam after the KB optics and a removable laser in-coupling mirror to overlap X-rays with an optical laser or an aperture to reduce parasitic scattering from the differential pumping apertures and upstream elements.

The beam then travels into the C1 chamber that encloses the interaction region. Before reaching the sample interaction region, the beam is cut by apertures (see Figure 3.3). The apertures are mounted on encoded stages that are driven by piezoelectric actuators with sub-micron movement precision. Experience shows that a useful aperture material for the AMO instrument beam parameters is silicon nitride ( $Si_3N_4$ ). These silicon nitride substrates have windows with tapered-edges, which can be used to cut into the X-ray beam without generating significant scattering

### 3 Experimental Considerations

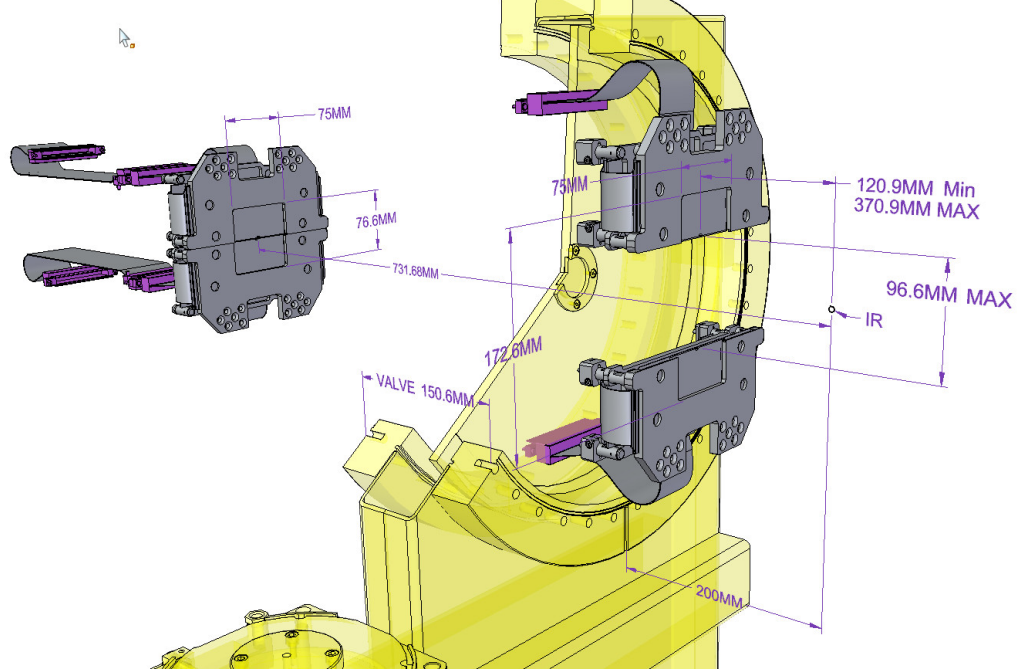


Figure 3.4: View of the pnCCD detector geometry inside LAMP. The interaction region (IR) is in the center of C1. The beam propagates along the Z-axis, where the rear (top) pnCCD is placed 728.53 mm away from the interaction region (original engineering distances). The half detector height is 38.3 mm and results in a scattering angle of  $\Theta = 4.3^\circ$ . With the gate-valve installed, the front pnCCDs are able to travel along the Z-axis from (121 to 371) mm downstream of the interaction region. The front pnCCDs can be moved along the Y-axis and at maximum extension, the outer corners of the front pnCCD detector correspond to a scattering angle of  $\Theta = 38.1^\circ$ .

of the tapered edges. The window-size can be fit to the size of the X-ray beam diameter, which can be estimated using geometric optics. Alternatively, oversized aperture windows can be used to drive one corner of the window on the first aperture stage and the opposite corner on the second stage into the beam, which is sometimes referred to as cornering apertures. As part of this thesis work, an improved aperture system was designed using four aperture blades with tapered edges. These allow full control over the aperture from four directions, thus allowing short aperture alignment times and a more controlled reduction of unwanted effects. For soft X-rays, it is important to note that the flat side of the tapered aperture is facing the beam such that the tapered-edges are facing downstream.

In the center of C1, where sample and X-rays interact, a time-of-flight spectrometer can be installed (see Figure 3.3), which is described in detail in Section 3.5. The beam then enters

the C2-1 chamber through a large gate valve. Here, a variety of distances become relevant for the digital combination of diffraction images from the front and rear pnCCD detectors (see Section 3.3). The algorithm to combine the images is discussed in detail in Section 4.2.1, but the following discusses the design distances. Figure 3.4 shows the pnCCD detector geometry inside the LAMP instrument including the gate-valve. The manufacturing size of the gate-valve along the Z-axis is 150.6 mm. The front pnCCD is mounted on a motorized stage and can be moved along the Z- and Y-axis inside the vacuum. The front-bottom pnCCD module can be set between (117.75 to 367.75) mm downstream of the center of C1 along the Z-axis. The front-top pnCCD module is mounted fix with respect to the bottom module and is always 3.15 mm closer to C1. The maximum extent along the Y-axis is 48.3 mm from the beam to the onset of the detector. In the thesis experiment, the front pnCCD modules were in the most rear position and their extent along the Y-axis was asymmetric, whereby the front-top pnCCD was 17.3 mm from the beam and the front-bottom pnCCD was 18.9 mm. The distance from the center of C1 to the bottom-rear pnCCD detector module is 731.68 mm and the top-rear pnCCD module is again 3.15 mm closer to C1<sup>7</sup>. A set of motorized, in-vacuum stages allow the use of another YAG crystal (D), an optical filter and a B<sub>4</sub>C beam stop just before the rear pnCCD. In this thesis, both pnCCD detectors were used such that another B<sub>4</sub>C beam stop and Yag crystal was mounted on a motorized stage behind the rear pnCCDs to stop the X-rays.

### 3.3 The large area pnCCD detectors

The pnCCDs are attractive photon area detectors for the following four reasons [166, 167]: one, their high quantum efficiency (QE) and good signal to noise ratio; two, their read-out rate is very high – up to 200 Hz; three, their large active areas cover wide scattering angles; and four, the detectors are almost defect free after applying widely-used pixel detector image corrections. pnCCDs were originally designed to be sent into space and have found usage in astronomy and material science [168]. The pnCCD detectors have been used first as X-ray diffractive imaging detectors at FLASH and at LCLS, namely in the CAMP instrument [161]. At LCLS, these detectors are mostly used for X-ray diffractive imaging, but they also have spectroscopic capabilities, which are demonstrated in the left panel of Figure 2.14. For this thesis, the pnCCD detectors were used to record diffraction images and are described in detail below.

Let us begin by describing the chip geometry [105]. Each front or rear pnCCD detector is made out of two modules. Figure 3.5 shows the layout of a single pnCCD module. The chip

---

<sup>7</sup>These design distances must be extended by ~5 mm along the Z-axis due to customization during the initial setup of LAMP.

### 3 Experimental Considerations

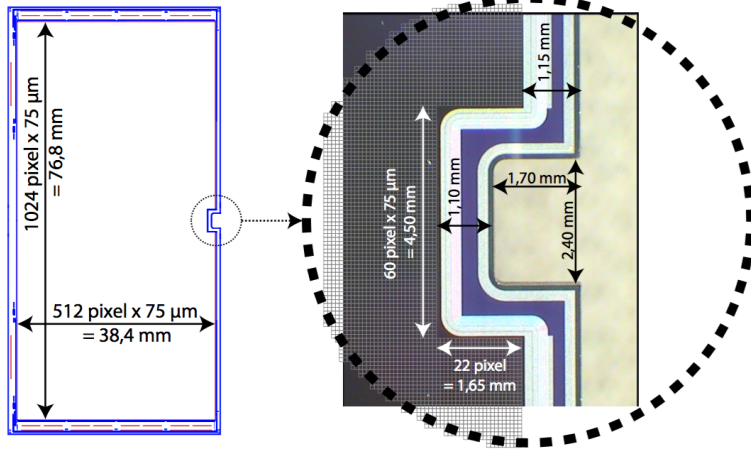


Figure 3.5: Geometry of a single pnCCD module with a detailed view of the beam conveying hole.

A single module consists of  $1024 \text{ pixels} \times 512 \text{ pixels}$ . Each pixel is  $75 \mu\text{m} \times 75 \mu\text{m}$ , which results in an active area of  $76.8 \text{ mm} \times 38.4 \text{ mm}$ . The chip is surrounded by non-active edges, which are  $1.15 \text{ mm}$  wide on beam facing edges. The hole reduces the active area on one module by  $60 \text{ pixels} \times 22 \text{ pixels}$ , or  $4.5 \text{ mm} \times 1.65 \text{ mm}$  and allows the beam to propagate through a  $2.4 \text{ mm} \times 1.7 \text{ mm}$  hole.

consists of  $512 \text{ pixels} \times 1024 \text{ pixels}$ . Each pixel has a size of  $75 \mu\text{m} \times 75 \mu\text{m}$ , so the area that the detector covers is  $38.4 \text{ mm} \times 76.8 \text{ mm}$ . To allow the FEL beam to travel through the instrument, each module has a rectangular region cut out in the middle of the center edge. On a single module this area is  $4.5 \text{ mm} \times 1.65 \text{ mm}$  and for the whole detector this “hole” has the dimensions  $4.5 \text{ mm} \times \sim 4.5 \text{ mm}$ . The rear pnCCD position has been chosen such that the pnCCD hole slightly oversizes the diverging FEL beam, when the focus is in the middle of the C1 chamber. The borders of each module are insensitive to photons over a width of  $1.15 \text{ mm}$  and  $1.10 \text{ mm}$  at the borders of the hole. To minimize the overall detector area that is insensitive to photons, the two pnCCD modules are mounted such that the non-sensitive areas overlap. As a result of that, each top module is  $3.15 \text{ mm}$  closer to the interaction region than the corresponding bottom module. The effective gap that is seen in the laboratory frame images between each top and bottom module measures  $16 \text{ pixels}$  or  $\sim 1.2 \text{ mm}$ .

The pnCCD chip is read out with a custom CMOS multichannel Analog MultiplEXer (CAMEX). Eight CAMEX are installed on each pnCCD module, which are indicated on top and bottom of the pnCCD module overview in Figure 3.5. The CAMEX performs two interesting functions; one, instead of reading out every pixel sequentially, it can read-out 128 pixel rows in parallel enabling pnCCD image read-out rates of up to  $200 \text{ Hz}$ ; two, it pre-amplifies the photon signal through a set of gain amplifiers. For this thesis experiment, the pnCCD gain settings become

Key	relative gain	approx. ADU/keV	max. photons per pixel
1	1/256	5	1100
2	1/128	10	640
3	1/64	20	320
4	1/16	79	80
5	1/4	316	20
6	1	1250	5

Table 3.2: Typical generated ADU values and dynamic range using 1 keV photons at all pnCCD gain settings. It is a valid approximation to linearly extrapolate to other photon energies.

interesting as they need to be considered when combining detector images and are discussed in detail below.

Different gain modes can be used to be more sensitive to photons at high gain or to store signal from more photons at low gain. Table 3.2 shows information about the pnCCD gain settings and arbitrary detector units (ADU) generation. Gain  $\frac{1}{1}$  is the highest gain and  $\frac{1}{256}$  is the lowest gain. As one steps from highest to lower gains, e.g., from  $\frac{1}{1}$  to  $\frac{1}{64}$ , the ADU value creation per photon goes with that fraction in good approximation.

Another useful consideration for an experiment using the pnCCD detectors is the quantum efficiency and gain behavior of the pnCCD chip at various wavelengths. The pnCCD is “back illuminated” and the entrance windows are coated with a thin aluminum layer to reduce their sensitivity to optical light. For the soft X-ray operating range at the AMO instrument of (280 to 2000) eV, this aluminum coating attenuates the X-rays only slightly and the detectors maintain a quantum efficiency of  $\sim 90\%$  [161]. At the AMO instrument, it is thus possible to linearly estimate the generated ADU values from elastic scattering at various photon energies, for example, a 1 keV photon will generate approximately 1250 ADU in highest gain (compare Table 3.2) and a 1.5 keV photon will generate approximately 1750 ADU in highest gain (compare Figure 2.14). For the photon energy of 837 eV used in this thesis experiment, photons approximately generate  $\sim 1087$  ADU in highest gain. The highest gain has been applied to the front pnCCD detector and the rear pnCCD detector was set to gain  $\frac{1}{64}$ . For the gain  $\frac{1}{64}$ , the ADU value generation per 837 eV photon can be estimated as  $\frac{1087}{64} \text{ ADU} \approx 17 \text{ ADU}$ .

### 3 Experimental Considerations

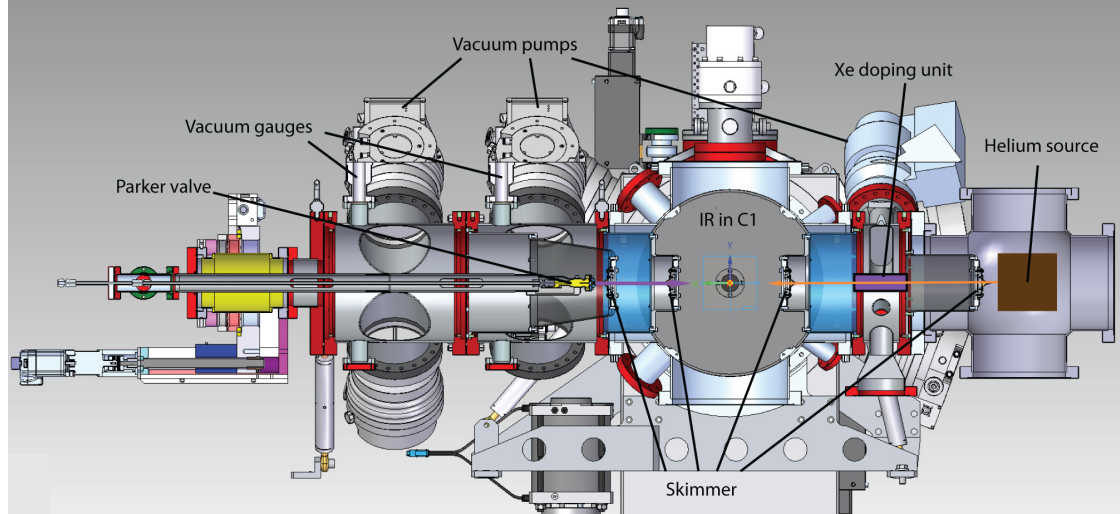


Figure 3.6: Downward view of a slice through the interaction region in C1 of the experimental setup. The purple arrow indicates the xenon gas flow, the orange arrow indicates the helium gas flow.

Chamber	Turbomolecular pump mod.	Roughing pump mod.
Xenon source	4x Leybold Turbovac TMP 361	
Xenon skimmer	2x Leybold Turbovac Mag W 300 P	
Helium source	2x Leybold PK-S 1300	adixen ACG600
Helium skimmer	2x Pfeiffer HiPace 300	
LAMP C1	1x Pfeiffer HiPace 700	
LAMP C2-1	4x Pfeiffer TC 400	adixen ACP 120G

Table 3.3: Installed vacuum pumps per chamber in the experiment.

### 3.4 Sample delivery

For this experiment, two gas sources are used in order to create single rare-gas clusters: one, a pulsed gas source for high pressure xenon operations at room temperature; and two, a continuous gas expansion source for helium operations that is cryogenically cooled. Given the time constraint of performing experiments at the LCLS, both sources are installed in one setup and operate independently, allowing quick sample changes. A schematic setup of the sample environment can be found in Figure 3.6 and a list of used vacuum pumps can be found in Table 3.3. The principle of the cluster generation is discussed in Section 2.2.1 and 2.2.2. Experimental aspects of the gas sources and operations is discussed in the following.

The AMO cluster source, which produces xenon clusters, consists of a Parker-Hannifin Series 99<sup>8</sup>

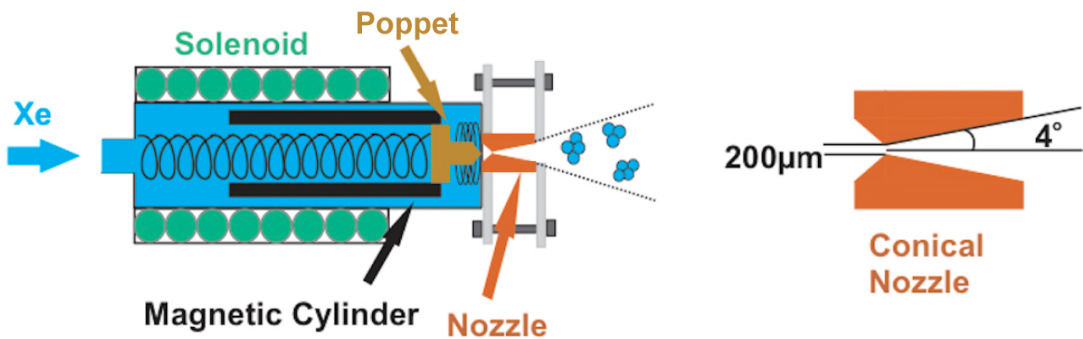


Figure 3.7: Schematic of the Parker-Hannifin Series 99 pulsed in-line valve and custom copper nozzle. The nozzle is clamped to the pulsed valve using an indium gasket to seal. The vespel poppet is attached to the magnetic cylinder and closes the valve. If a current is run through the solenoid, the valve actuates and opens. Adapted from [97].

pulsed valve using a solenoid with a custom manufactured conical copper nozzle, two vacuum chambers to mount two skimmers, a slit that is adjustable through a piezoelectric motor, and several vacuum pumps. It is a well-characterized source that was used extensively in the past [10, 21, 22, 52, 92]. The pulsed solenoid valve (see Figure 3.7) is controlled with a Parker-Hannifin Iota One pulsed-valve driver. The valve driver applies a current to the solenoid, a magnetic cylinder with the attached poppet actuates and opens the valve. After the TTL signal from the driver ends, the valve closes again. The valve's opening time is set to 1 ms and repetition rates of up to 30 Hz can be set at a xenon reservoir pressure range of (100 to 2000) kPa. The pulsed valve heats up substantially during operations and due to abrasion, the vespel poppet is replaced every ~60 h of operating time, or as needed to prevent a leakage from the gas source. The nozzle has a 200  $\mu\text{m}$  opening diameter and an opening half angle of 4°. It is clamped to the Parker valve using an indium gasket to seal. Two skimmers with an opening of 1 mm diameter and an adjustable piezo-skimmer have been installed to define the gas jet. The adjustable slit is formed by two razor blades and the slit width is adjusted through a piezo motor by applying a voltage,  $U$ , from (0 to 10) V. At  $U = 8$  V, the slit is virtually closed, allowing typically one cluster in the interaction region at a time, which is called the *single cluster regime*. The excess gas in the source and skimmer chambers is removed by turbo-molecular pumps that are connected to roughing pumps (see Table 3.3). Ultimately, these chambers reduce the gas load of C1 chamber and the pressure,  $p_{\text{IR}}$ , of the interaction region settles are  $p_{\text{IR}} \leq 10^{-3}$  Pa.

The helium source along with the xenon doping unit and the skimmers is depicted in Figure 3.6.

---

<sup>8</sup>Series 99 is at the time of writing not produced/advertised as a straight, in-line pulsed valve anymore.

### 3 Experimental Considerations

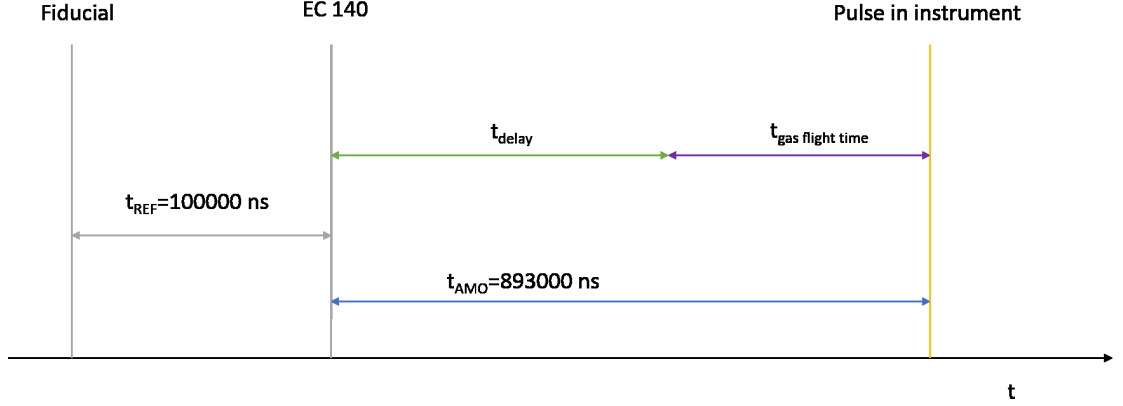


Figure 3.8: Schematic of the LCLS event receiver (EVR) timing system.

Helium droplets are produced in a continuous free gas expansion using an electron microscope diaphragm as nozzle (Plano A0200P) that has a  $5\text{ }\mu\text{m}$  orifice and an orifice channel length of  $\sim 2\text{ }\mu\text{m}$  [79]. The nozzle is cooled to cryogenic temperatures  $T = 5.8\text{ K}$  using a Sumitomo cold-head. The particle beam is defined by a first  $0.5\text{ mm}$  and a second  $1\text{ mm}$  diameter skimmer. As explained above, an adjustable slit system allows the definition the gas jet to single helium droplets. A doping unit is installed in the skimmer chamber of the helium source. It is a separate, smaller chamber in the skimmer chamber, where He-clusters can traverse through two smaller holes on each side. So, the gas load from the doping unit is mostly confined, which allows locally increasing the pressure of xenon to  $p_{du} \leq 0.3\text{ Pa}$ . The pressure is manually controlled using a leak valve. As schematically shown in Figure 2.10, the partial helium pressure is determined with a residual gas analyzer (RGA) opposite the helium source in the chamber that contains the AMO cluster source. The RGA pressure reading is used to determine the depletion  $\frac{\Delta p_{de}}{p_{de}}$  (see Equation (2.27)) of the helium clusters through the pickup of xenon atoms. A thorough alignment of the sources is necessary to overlap the particle beams such they traverse through all skimmers.

#### 3.4.1 Sample jet timing at LCLS

Pulsed gas jets such as the one using the Parker solenoid valve require an electric trigger to open the valve at the right time such that the injected sample intercepts the light pulse. At LCLS, an event generator sends a fiducial, i.e., a clock signal with  $360\text{ Hz}$ , and several event codes, e.g., at  $120\text{ Hz}$ , to an event receiver (EVR) over a fiber network with a  $10\text{ ps}$  precision [169]. The EVR processes these signals and supplies triggers to the components with a specific delay to an event code (EC). Figure 3.8 schematically illustrates the timing system. Following the schematic, the process starts with a fiducial and an event code, e.g., EC 140, is delayed by a time of event code x

### 3.4 Sample delivery

( $TECx$ ). After a certain time of the fiducial a LCLS pulse arrives. At the AMO instrument, this time<sup>9</sup> is  $t_{AMO} \approx 893\,000$  ns. Each event code  $x$  has a slight variation in arrival time,  $TECx$ , with respect to the initial fiducial, as the timing signal has a “clock rate” of 120 MHz only one EC can be sent every 8.4 ns. The LCLS control system automatically corrects for different  $TECx$  by internally correcting the delay to a reference time  $t_{REF}$  that corresponds to EC 140. EC 140 has a 120 Hz repetition rate and occurs only when an X-ray pulse is present. The reference time is artificially set to  $t_{REF} = 100\,000$  ns. We can gather the above considerations to establish a delay time to trigger a sample jet to coincide with a LCLS pulse. We note it as

$$t_{delay} = t_{AMO} - t_{gas\ flight\ time}, \quad (3.1)$$

with  $t_{delay}$  being the delay value for the LCLS EVR control system and  $t_{gas\ flight\ time}$  the flight time of the sample from the gas source to the interaction region. As described in Section 2.2.1 and Reference [80], the terminal velocity,  $v_\infty$ , of a sample from a supersonic jet is

$$v_\infty \approx \sqrt{\frac{2RT_0}{m} \left( \frac{\gamma}{\gamma-1} \right)}, \quad (3.2)$$

with the universal gas constant  $R$ , the temperature in the stagnation chamber  $T_0$ , and the ratio of specific heats  $\gamma = \frac{c_P}{c_V}$ , which is  $\gamma = \frac{5}{3}$  for monoatomic gases such as rare-gases. The flight time of a certain gas can then be calculated by measuring the distance,  $D$ , between the source and the interaction region, thus  $t_{gas\ flight\ time} = \frac{D}{v_\infty}$ . The approach may be extended to approximate flight times of molecules, e.g., using the mass of CO,  $m_{CO} = 28$  u, and also to gas mixtures, for example, the mass of a 2 % xenon-131 and 98 % helium-4 gas mixture can be estimated using a weighted average according to their relative contributions, thus  $m_{HeXe} = 6.54$  u. As convenience, the Table 3.4 shows terminal velocities of several rare gases at room temperature.

Figure 3.9 shows measured and calculated flight times using an Even-Lavie (EL) supersonic gas source<sup>10</sup> instead of the earlier described Parker valve. The gas dynamics from an EL-source are similar to a Parker valve, but it has a very well-defined opening time and thus a well-defined gas jet. A typical opening time of the one used here is 22 µs, which can be time consuming to trigger properly without knowing  $t_{delay}$ . The data show very good overlap of the calculated delay times  $t_{delay}$  from Equation 3.1 and the ion-yield maximum of the particle beam. The calculated flight times include an error margin, which can also be read as a recommended scan range. While the electric triggering and actual valve opening times may add errors on the microsecond time-scale,

---

<sup>9</sup>Times are in nanoseconds (ns) and in a format to comply with the LCLS interface.

<sup>10</sup>The EL-valve has the serial no.: EL 5 HRR NO 114.

### 3 Experimental Considerations

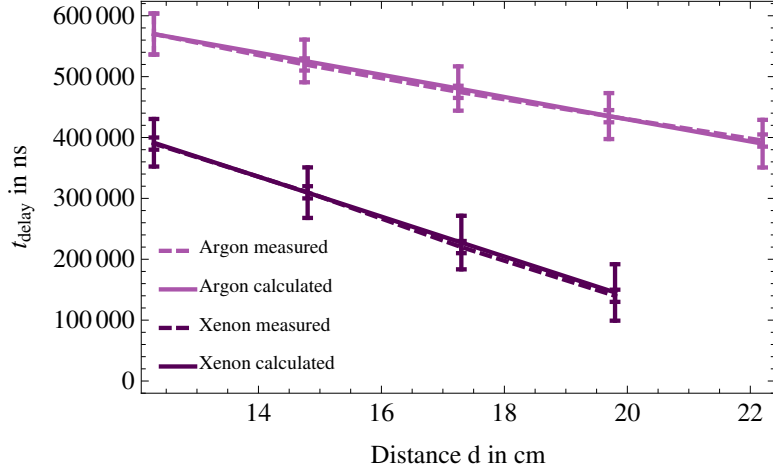


Figure 3.9:  $t_{\text{delay}}$  as a function of the gas source distance to the interaction region. Xenon and argon has been used as sample gas in an Even-Lavie pulsed valve. The calculated delay values (solid lines) agree well with the measured delay times (dashed lines) to overlap the onset of the pulsed jet with the laser.

Sample gas	Helium	Neon	Argon	Xenon
$v_\infty$	$1745.5 \text{ m s}^{-1}$	$780.6 \text{ m s}^{-1}$	$512.0 \text{ m s}^{-1}$	$305.0 \text{ m s}^{-1}$

Table 3.4: Terminal velocities of some rare gases at room temperature,  $T = 293.15 \text{ K}$ .

uncertainties in temperature  $T_0$  and distance  $D$  change delay times drastically.

Very long flight times can occur when heavy gases, such as xenon, are used or long distances,  $D$ , are necessary. If the flight times  $t_{\text{gas flight time}} > t_{\text{AMO}}$  the system has to be delayed onto the next event as negative delays are not possible in the LCLS timing scheme. In this case, Equation (3.1) can be rewritten to

$$t_{\text{delay}} = \frac{1}{f_{\text{rr}}} + t_{\text{AMO}} - t_{\text{gas flight time}}, \quad (3.3)$$

with  $f_{\text{rr}}$  being the repetition rate of the event code.

### 3.5 Time-of-flight mass-spectrometer

An ion time-of-flight spectrometer was used in the interaction region to detect xenon and helium ions. A time-of-flight spectrometer uses electric fields to accelerate ions from the interaction region towards a detector. The detector unit often consists of a micro-channel plate (MCP) that allows recoding an arrival signal and calculating the time-of-flight (TOF) of the ions. The

### 3.5 Time-of-flight mass-spectrometer

following considerations connect the time-of-flight to ions with a specific *mass-to-charge ratio* [170].

In the first stage, the ions are accelerated from the interaction region towards the detector. Here, the electric potential energy is converted into kinetic energy

$$qU = \frac{1}{2}m \left( \frac{d_1}{t_{\text{of}1}} \right)^2, \quad (3.4)$$

$$t_{\text{of}1} = \sqrt{\frac{m}{2qU}} \cdot d_1, \quad (3.5)$$

with  $q$  being the elementary charge of the ion,  $U$  the voltage difference,  $d_1$  the distance between the interaction region and spectrometer,  $m$  is the mass of the ion, and  $t_{\text{of}1}$  is the time-of-flight in the acceleration stage. The ions then travel through a drift tube of length  $d_2$  that is field free. As the velocity remains constant, we can write down

$$t_{\text{of}2} = \sqrt{\frac{m}{2qU}} \cdot d_2, \quad (3.6)$$

with  $t_{\text{of}2}$  being the time-of-flight in the drift tube. The total flight time can then be written as

$$t_{\text{tot}} = t_{\text{of}1} + t_{\text{of}2} = \sqrt{\frac{m}{2qU}} (d_1 + d_2), \quad (3.7)$$

In a typical experiment, all values aside from  $m$  and  $q$  can be considered constant. Therefore, we may note the time-of-flight in its well known dependency, as

$$t_{\text{tot}} \propto \sqrt{\frac{m}{q}}. \quad (3.8)$$

In specific cases, where atoms become ionized and their kinetic energy,  $E_{\text{kin}}$ , is  $E_{\text{kin}} = 0$ , the spectrometer records narrow peaks that are spaced according to their mass-to-charge ratio. However, atomic ions usually start with a kinetic energy,  $E_{\text{kin}} \neq 0$ , such that the time-of-flight is altered and the signal peak structure is broadened. If molecules or clusters become ionized, fragments have additional translational energy resulting from dissociation of a metastable ion measured relative to the center-of-mass, which is often referred to as kinetic energy release [171]. This leads to additional broadening of the signal peak structure.

The time-of-flight spectrometer used in this thesis experiment is depicted in Figure 3.10. It is a double sided spectrometer for electron and ion detection. A side view of the spectrometer can

### 3 Experimental Considerations

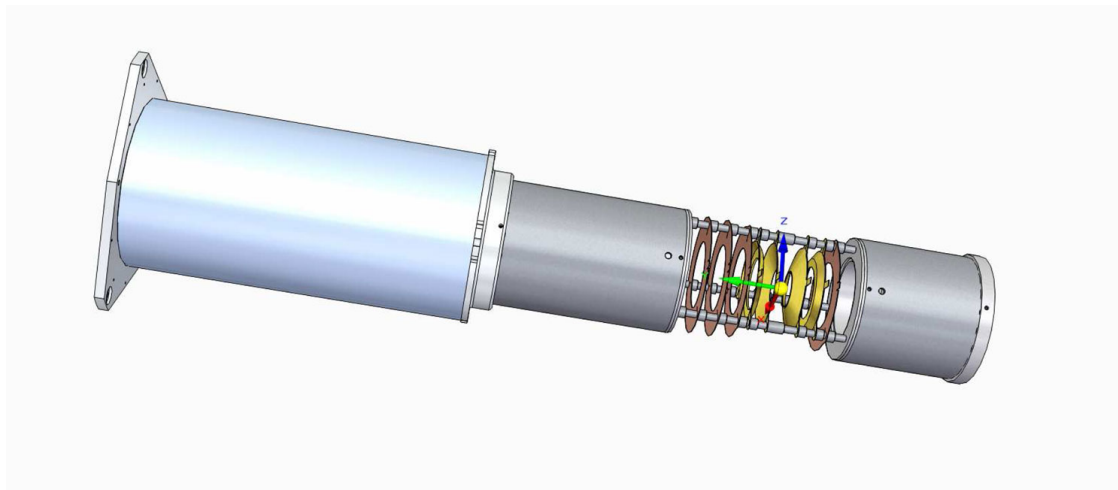


Figure 3.10: Drawing of the time-of-flight spectrometer.

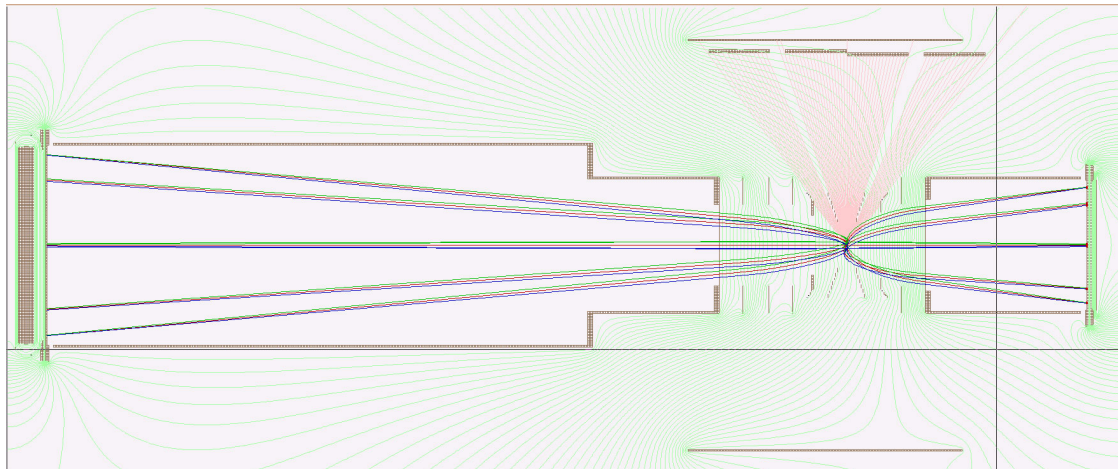


Figure 3.11: Sideview of the spectrometer showing ion, electron and photon trajectories upon interaction with LCLS. The image was created with SIMION. From [172].

<b>Ion-side Connection</b>	<b>Voltage in V</b>	<b>El. Side Connection</b>	<b>Voltage in V</b>
MCP Front	-2600	MCP Front	200
MCP Back	5	MCP Back	2200
Holder	200	Phosphor	3000
Conical lens 70deg	-923	Holder	6000
Conical lens 53deg	-1393	Conical lens 70 deg	500
Flat lens #1	-1490	Conical lens 53 deg	1370
Flat lens #2	-1564	Flat lens	1940
Flat lens #3	-1639	Flight tube	2736
Flight tube	-1714	-	-

Table 3.5: Applied voltages to the time-of-flight spectrometer (ion side use only).

be found in Figure 3.11. In this schematic, ion, electron and photon trajectories upon interaction with a LCLS pulse have been simulated using SIMION [172]. A conical lens stack avoids casting a shadow on the pnCCD detectors (top of schematic). The applied voltages in the experiment can be found in Table 3.5. Only ion spectra have been recorded but in the experiment, the electron side is powered to have unperturbed electric fields across the interaction region.

## 3.6 X-ray focus characterization

A focus characterization is usually performed before X-ray diffractive imaging experiments to optimally focus the X-rays at the desired interaction region. Two focus characterization methods are described here: one, using a TOF spectrometer; and two, being a so-called imprint study.

### 3.6.1 Focus characterization using a TOF spectrometer

For a focus characterization using a TOF spectrometer, the experimental chamber is usually filled with a well known gas, for example, neon, such that the pressure inside the experimental vacuum chamber is on the order of  $10^{-4}$  Pa. The TOF spectrometer or the focal point are then moved with respect to each other and ion time-of-flight data is recorded. The left panel in Figure 3.12 shows a focus characterization, where a TOF spectrometer was driven along the Z-axis on which the X-ray focus was placed. The fractional neon ion-yield per charge state is plotted as a function of the spectrometer's Z-position. The data show that a 2 mm region centering around the focal plane at  $Z = 0$  mm is most useful for experiments requiring high X-ray intensities. The right panel of Figure 3.12 compares the fractional neon ion-yield at the optimal focus position from November 2013 [105] to October 2009 [173] using  $\sim 1.25$  keV photons and comparable pulse energies. The comparison reveals that high-charge states of neon, for example,  $Ne^{8+}$  and  $Ne^{9+}$ ,

### 3 Experimental Considerations

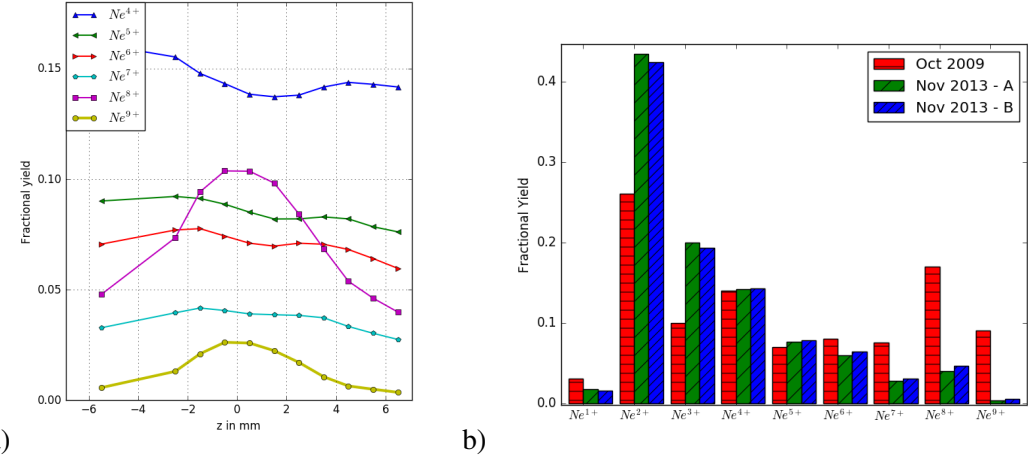


Figure 3.12: a) Atomic neon charge state yield from TOF as a function of Z-position, relative to optimal focus position  $Z = 0$ .  $Z = (0 \pm 1)$  mm is a favorable length for sample injection. b) Comparison of atomic neon charge state yield from TOF for different cases: red, experimental data from October 2009 with 4 blades (S) opened; green, experimental data from November 2013 with (S) closed; blue, Experimental data from November 2013 with (S) opened.

are less abundant, which can be attributed to the deterioration of the optics over the first years of operations.

#### 3.6.2 Focus characterization via an imprint study

In an imprint study, a target, typically a lead tungstate ( $PbWO_4$ ) window, is placed at the desired interaction region on a motorized stage. The X-ray focus is then moved and for each step at least one X-ray pulse should be shot at the target. The target is then moved slightly since the X-rays point at the same spot and the procedure repeated. This process should be repeated at various X-ray beam attenuation, as we will see below. Figure 3.13 shows exemplary data from an imprint study. The  $PbWO_4$ -target is studied using an optical microscope and typical imprint images are shown in the panel a) to d). Here the target was illuminated with LCLS X-ray pulses at 1600 eV at various transmission values,  $T$ . The crater sizes vary according to the X-ray peak fluence and we shall derive in the following the correlation between crater size and the full-width at half-maximum (FWHM).

### 3.6 X-ray focus characterization

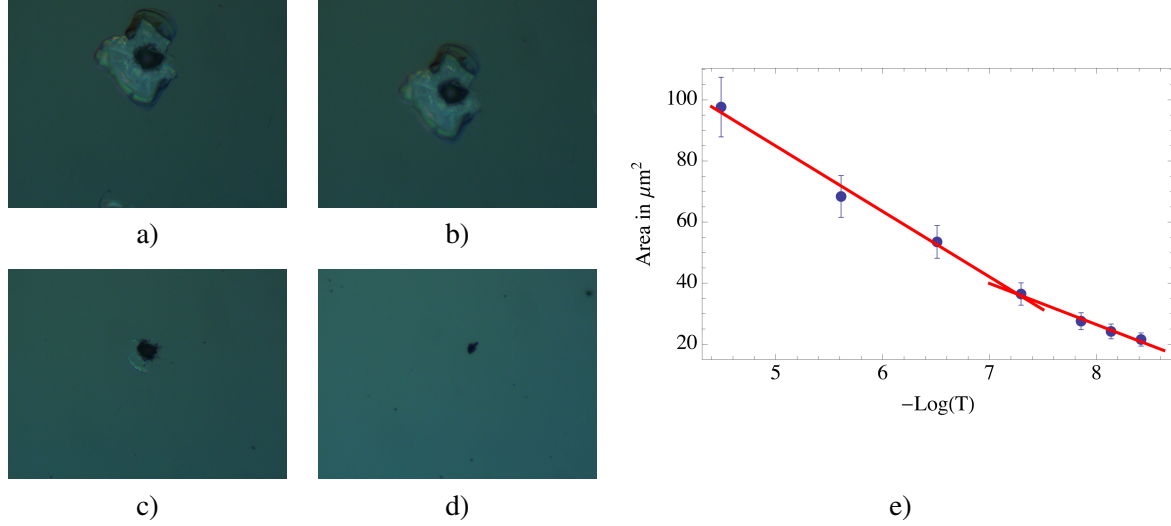


Figure 3.13: a)-d) Ex-situ microscope imprint study of a lead tungstate sample that was irradiated with single, 1600 eV LCLS pulses at different gas attenuation. e) Non-linearity in Liu plot [174] due to LCLS's multi-gaussian beam profile. The approximate FWHM  $\approx 3.4 \mu\text{m}$  is determined from the slope of the linear fits.

Let us describe the energy fluence,  $E(R)$ , of the X-rays as

$$E(R) = E_0 e^{\frac{-R^2}{2\sigma^2}}, \quad (3.9)$$

with the radial coordinate  $R$ , a characteristic radius  $\sigma$ , and the peak fluence  $E_0$ . Typically,  $\sigma$  stays a constant beam parameter, which is typically set by the optimal focus position of the KB-optics and thus does not affect the crater area. The crater area changes due to varying the peak fluence,  $E_0$ . As  $E_0$  increases, more and more of the target is irradiated with power densities above the damage threshold such that larger craters form. We can measure the peak fluence,  $E_0$ , through to the pulse energy,  $E_p$ , which is measured with the gas detector. Let us explicitly note their proportional dependency,  $E_0 \propto E_p$ . Now, we can express the peak fluence more conveniently in terms of the pressure,  $p$ , in the gas attenuator

$$\log(E_0) = \log(E_{\text{in}}) + \log(T) = -p \cdot c + \text{const.}, \quad (3.10)$$

with the incident peak fluence at the gas attenuator  $E_{\text{in}}$  and the transmission  $T$ . In the gas attenuator, the transmission is  $T = e^{-p \cdot c}$  and a constant  $c$ . The constant  $c$  can be derived from Reference [175]. For the LCLS attenuator filled with nitrogen gas ( $\text{N}_2$ ) over its 4.1 m length at 1600 eV photon energy,  $c \approx 4.208\,907\,37 \cdot 10^{-3} \text{ Pa}^{-1}$ . We can further approximate the crater

### 3 Experimental Considerations

surface area using a circle. The area then is  $\pi r_0^2$ , with the crater radius  $r_0$ . As shown in Reference [174],  $r_0^2 = 2\sigma^2 \log(\frac{E_0^2}{E_0^1})$ , with  $E_0^{1/2}$  being the peak fluence at two different attenuation levels. Thus, the slope of a linear fit between the two points  $E_0^{1/2}$  is  $2\pi\sigma^2$ . The FWHM =  $2\sqrt{2\ln(2)}\sigma$ . The right panel of Figure 3.13 shows the crater-area as a function of  $-\log(T) = p \cdot c$ , which is often referred to as a Liu's plot. The data points are fitted with two linear fits, which indicate nonlinearities that come from a multi-Gaussian beam-profile, which is often called a super-Gaussian beam-profile [176, 177]. The FWHM can be determined from the slope of the linear fit at smaller transmissions and is FWHM  $\approx 3.4 \mu\text{m}$  using the exemplary data. The LCLS parameters in the experiment of this thesis are different to the above exemplary data and are summarized in Table 3.1.

# 4 Methods

This chapter describes the analysis methods used in the present thesis and it is organized as follows: Section 4.1 describes the general LCLS computing environment to establish an overview of the hard- and software capabilities; Section 4.2 discusses common corrections and the combination of raw pnCCD images; Section 4.3 goes over used phase-retrieval algorithms and discusses the image resolution; Section 4.4 considers the contribution of scattering from the X-ray pump–X-ray probe pulses; Section 4.5 discusses simulations of 2D projections of spheres and corresponding diffraction patterns; and the Section 4.6 evaluates several hit-finding methods.

## 4.1 The computing environment at LCLS

All data taken at LCLS are stored in the LCLS computing environment, where the data can also be analyzed. The reason for this is the vast amount of data that are generated by LCLS and the instruments. Let us conservatively estimate the data produced by the LAMP end-station. Usually, the LAMP end-station has two pnCCD detectors that operate at a 120 Hz frame rate. Each image is in a 32 bit-per-pixel format such that an image is approximately 4 MB in size. So, every minute the front & rear pnCCD produce approximately 60 GB of data or 700 GB per 12 h shift. The handling of these data is indicated in Figure 4.1. The DAQ readout nodes send the data traffic via Ethernet to a short-term cache and fast feedback (FFB) layer. While the data are being transferred, online monitoring nodes are able to “see” a fraction of the live (online) data and run analysis. With a delay of a few tens of seconds, the FFB nodes can be used to run analysis on the full data stream using parallelization. The FFB nodes can only be used during the beamtime. Eventually, the data are moved to normal hard-drives (offline), where the data files are managed by an integrated Rule-Oriented Data System (iRODS). The data are stored in .XTC file containers and it can also be accessed from outside SLAC (Router & ESNET). The stored data have certain storage quotas and times. In brief, there is a six month short-term storage without quota limitations and a two-year medium-term storage with a storage quota of 10 TB. After that, the data are automatically stored for at least ten years on magnetic tape (long-term storage) and can be restored upon request. A web interface is provided by the DAQ group to simplify and automate the data-handling and logging process. The short- and medium-term

#### 4 Methods

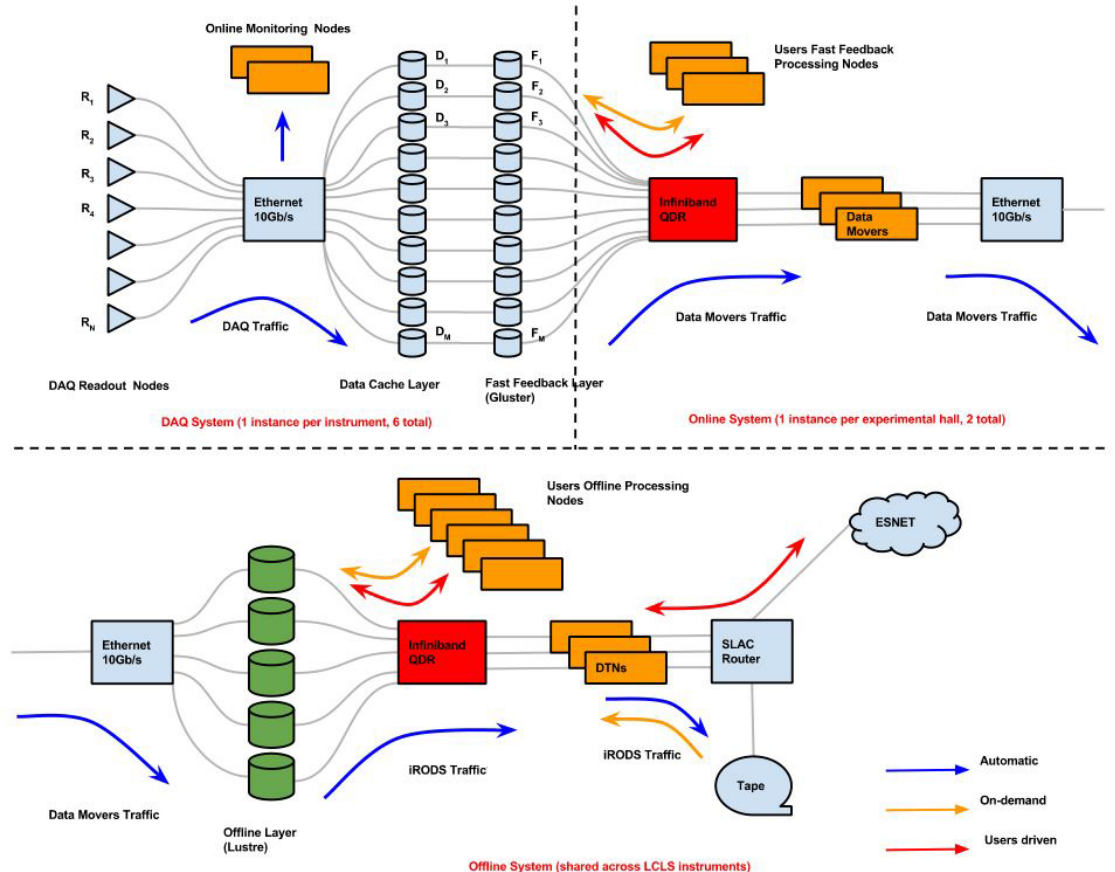


Figure 4.1: Diagram of the computing environment at LCLS and DAQ traffic. The recorded data is exchanged through Ethernet and after digitization, is stored on a cache and FFB cluster, where psana computer have access to the online environment during the experiment. Eventually, the data is moved to the more permanent offline environment, where data can be analyzed on psana computers or through a load sharing facility. Adapted from [178].

storage solutions can also be used to analyze the data using the Psana<sup>1</sup> software package [179] to access data and to perform computations on the psana computer cluster with over 1000 CPU cores. A load sharing facility (LSF) allows the scheduling of batch jobs including parallelization. The psana-framework has a python script interface. The python script calls functions within the psana-framework that are programmed in C(++)<sup>1</sup>, for example, detector calibrations. Psana allows parallelization via Message Passing Interface (MPI) and it is therefore possible to analyze many events (LCLS pulses) simultaneously. Also complex analysis is able to be processed at the rate of the incoming data using MPI, when the FFB is used. Python scripts can be written for “online” or “offline” analysis and are of similar syntax.

For LCLS-II [178], the analysis and data-access scheme is designed to be similar to Figure 4.1 with the exception of the online monitoring nodes. It is therefore recommended to build analysis schemes that are based on psana and use the FFB for online analysis, which can then be adapted easily for offline analysis as well. A quick introduction on how to use psana can be found at <https://confluence.slac.stanford.edu/display/PSDM/LCLS+Data+Analysis> (from February 2017).

## 4.2 pnCCD photon detectors

Before the pnCCD detectors can be used to take data, it is good practice to record dark reference images. These reference images allow software corrections to the raw detector image in order to reduce detector artifacts, such as electronic noise. Since these corrections are standard, the LCLS detector and DAQ group has implemented a calibration manager tool<sup>2</sup> (calibman) that provides the necessary algorithms and helps with the procedure of applying image corrections and more. We discuss the two most-often used software corrections next. The first, corrects for the electronic noise pedestals (levels) of each pixel, and, the second, accounts for common modes, e.g., artifacts from the read-out electronics that appear, for the pnCCD, mostly in columns.

The effects of applying these corrections are illustrated in Figure 4.2 through a set of histograms. The histogram bins are showing ADU values from dark pnCCD images in highest gain. The green curve shows the ADU values of a raw detector image where no corrections have been applied and the electronic noise response from the chip has a standard deviation of  $\sigma_r = 136$  ADU. Note, that there is also a significant offset of the distribution from 0 ADU to  $\mu_r = 1515$  ADU. The blue curve shows the same data but is using the pedestal corrections found in cal-

---

<sup>1</sup>Psana is an acronym for Photon Science Analysis.

<sup>2</sup>The calibration manager tool calibman can be found in the psana software package. More information under <https://confluence.slac.stanford.edu/display/PSDM/Calibration+Management+Tool> (Oct 2016)

## 4 Methods

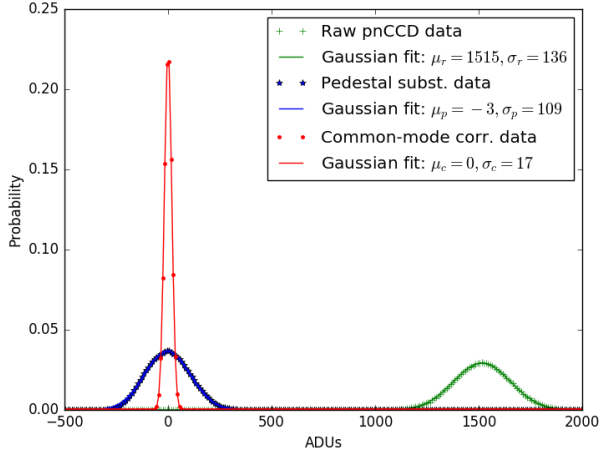


Figure 4.2: ADU histograms from electronic noise of dark pnCCDs in highest gain mode. The green plus symbols reflect a histogram of ADU values from raw electronic noise of pnCCD pixel. The noise is set off zero at  $\mu_r = 1515$  ADU and has a standard deviation  $\sigma_r = 136$  ADU. The same data shifts to the blue stars after applying a pedestal subtraction and the noise distribution has  $\mu_p = -3$  ADU and  $\sigma_p = 109$  ADU. For the red data points, the common-mode corrections have been applied and the distribution has  $\mu_c = 0$  ADU and  $\sigma_c = 17$  ADU.

ibman. The pedestal corrections reduce the noise slightly to  $\sigma_p = 109$  ADU, and as expected, the pedestal corrections drastically move the normal distribution to be centered around  $\mu_p = -3$  ADU. Finally, the red curve is also the same data than the green curve but includes pedestal and common-mode corrections. The corrected read-out modes drastically improve the standard deviation to  $\sigma_c = 17$  ADU and slightly move the mean to  $\mu_c = 0$  ADU.

As a guideline, the pedestal corrections should always be used to account for the mean offset. The common-mode calibration, however, should be tested before applying. The algorithm that determines common-modes needs to find a baseline and therefore needs at least one pixel with no signal in each row and column [180]. In single-particle imaging experiments, the detector is usually illuminated in most pixel. In this case, the common-mode correction algorithm may treat real signal as noise and fail to find a common baseline.

In the present thesis, pedestal and common-mode correction has always been applied on the front detectors, as only few pixel hold signal. The rear pnCCD uses the pedestal correction but corrects common-modes only above a certain, conservative threshold. See Figure 4.3 for the visible effect on front detector (large, top/bottom arrays) and rear detector (small, centered array).

### 4.2.1 Combining multiple pnCCD detectors

In order to maximize resolution, it is most useful to combine the front and rear pnCCD detector images from a single-shot into one larger image. While this is a simple task in itself, it becomes more complex when the combined images need to undergo a phase-retrieval process that use fast Fourier transformations (FFTs). In fact, it has not yet been shown in single-particle imaging that it is possible to retrieve a real space image from multiple detectors in different planes. The reason for this is that, so far, there was little incentive for merging multiple detectors. The combination of light-source, end-station, and sample size (compare, e.g., Reference [13]) means that little signal is detected at large scattering angles. With the intensities provided by LCLS and the single-particle imaging capabilities of the LAMP end-station, objects that are smaller than a hundred nanometer in diameter can be studied. This setup scatters significant signal at larger scattering angles that multiple pnCCD detector planes can be used. The combination of front and rear pnCCD detector images has three advantages: one, covering larger scattering angles increases the resolution; two, multiple detectors can be operated in different gains, which virtually increases the dynamic range of the combined system; and three, the signal-to-noise of the combined system is improved.

Let us now describe the process of combining multiple detector images from a single-shot, while simultaneously preparing them for the inverse problem of phase-retrieval. This basically requires two steps: one, the intensity normalization for the detectors that are in different gains and positions; and two, the pixel projection and down-sampling, which is here from the rear pnCCD plane to the front pnCCD plane. The discussion below follows the code shown in Appendix 1. The input for the following procedure are two pnCCD images. The images should be pedestal corrected and, if applicable, common-mode corrected (see Section 4.2). Analysis of the electronic noise results in a cutoff or offset between signal-to-noise for each image (see Figure 2.14a and 4.2). At this step it is also convenient to account for different detector gain settings,  $gain_{front,rear}$ , using Table 3.2 and the detector distances from the interaction region,  $distance_{front,rear}$ , to equalize the measured intensities. The following equation corrects the signal from the rear pnCCD to the front pnCCD plane

$$I(pixel_X, pixel_Y)_{normalized} = I(pixel_X, pixel_Y) \cdot \frac{gain_{front}}{gain_{rear}} \cdot \frac{distance_{rear}^2}{distance_{front}^2}, \quad (4.1)$$

$pixel_X$  and  $pixel_Y$  being the length of the pixel array from the beam along the X- and Y-axis, respectively. The pnCCD front top and bottom module are placed in an enlarged array to reflect

#### 4 Methods

the real geometry in the plane of the front pnCCD. We can now transform the rear pnCCD data to this pixel-constructed geometry. Let us use the earlier introduced scattering angle,  $\Theta$ , in  $X$ - and  $Y$ -axis separately

$$\Theta_{X,Y} = \arctan\left(\frac{\text{pixel}_{X,Y} \cdot a}{\text{distance}_{\text{rear}}}\right), \quad (4.2)$$

where  $a$  is the pixel size along one dimension. We can further generalize the matter and attribute a scattering vector  $\vec{Q}$  to each pixel, with the entries in  $X$ - and  $Y$ -axis separately again

$$Q_{X,Y} = 4\pi \frac{\sin\left(\frac{\Theta_{X,Y}}{2}\right)}{\lambda}, \quad (4.3)$$

with  $\lambda$  being the wavelength of the scattered photons. Now, we can add the signal from the rear pnCCD to the enlarged array, while using the generalized coordinates  $\vec{Q}$ . In this generalized downsampling process, the arithmetic mean of the downsampled pixel is used, which is why a normalization factor needs to be carried. The downsampling of the rear pnCCD and placement in the enlarged array ensures the new pixel size matches the one from the front pnCCD. This allows Fast Fourier Transformation (FFT) algorithms to use the array. The usage of FFT algorithms is of great interest to reduce computing times in iterative phase-retrieval algorithms.

An example of a combined diffraction image from a spherical xenon cluster of  $\sim 50$  nm radius is shown in Figure 4.3. The front pnCCD detector was set to slightly overlap with the rear pnCCD detector along the  $Y$ -axis, but the front detector was set  $\sim 365$  mm closer to the interaction region along the  $Z$ -axis. As described above, the rear pnCCD modules have been projected into the front pnCCD plane and in this process, the detector appears smaller on the combined image. The red circles are a help for the eye to align the modules and show that the diffraction pattern overlaps. In this exemplary data, the front pnCCD was operated in highest gain  $\frac{1}{1}$  and the rear pnCCD was operated in lowest gain  $\frac{1}{256}$ .

A good way of checking the continuity of the merged data is through the radial intensity profiles of the diffraction images (see Section 4.3.3). Figure 4.4 shows the radial intensity profile of the spherically symmetric diffraction image over 5 orders of magnitude above the noise level. The red curve illustrates the expected scattering intensity of a spherical object using Equation (2.38) and (2.41). The red curve showcases the validity of the detected signal up to the edges of the front pnCCD, where little signal is present. There are also some discrepancies from the red curve on the transition from the rear to front pnCCD, which are due to the shadow projected from the front onto the rear pnCCD and the resulting lack of signal.

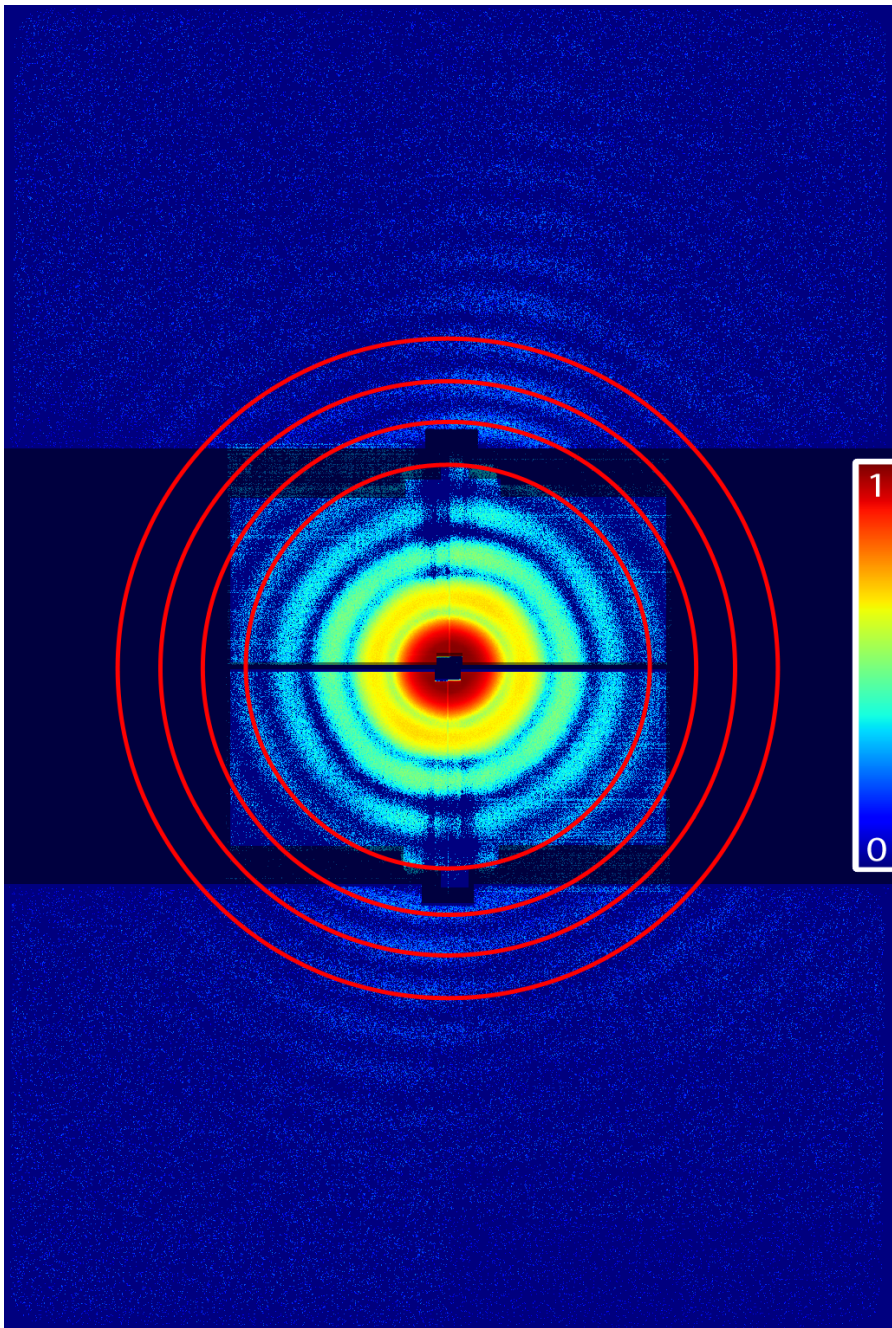


Figure 4.3: A combined pnCCD image using the full image of the front pnCCD and a down-sampled image of the rear pnCCD. The red circles in the image are drawn to visualize the alignment of the detectors. As described in the text, the intensities in the image are normalized and corrected for different electronic gains and distance to specific detectors. The black areas are not covered by the pnCCDs and are therefore masked out.

## 4 Methods

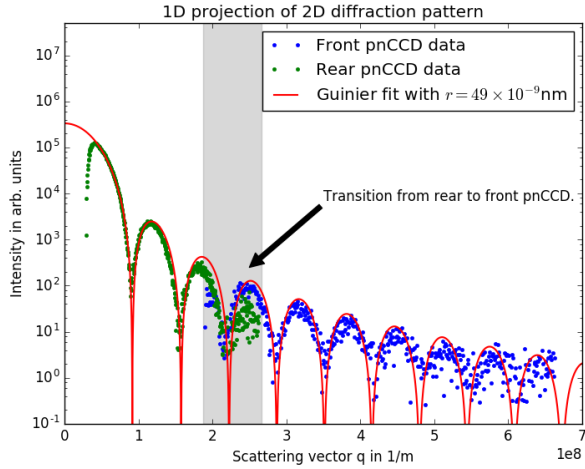


Figure 4.4: Spherical projection of 2D diffraction image onto 1D. The data points are from the rear pnCCD (green points) and the front pnCCD (blue points) have been combined. The gray shaded area shows the transition area from rear to front detector. The red curve is a simulated scattering curve from an ideal sphere (see Equation (2.41)). The amplitude of the red curve has been fitted to the data points and it agrees well with the data.

### 4.3 Phase retrieval from a single diffraction pattern

The diffractive imaging measures the continuous intensity distribution of an object in reciprocal space and the phase information is lost (see Section 2.3.2). Iterative algorithms can retrieve this lost information because there are only limited sets of phases that uniquely reproduce the diffraction image [181, 182]. To fully recover the original function, i.e., real and complex values of the imaged object, the diffraction image must be oversampled [183]. Here, the *Nyquist-Shannon sampling theorem* says that a Fourier transformed object,  $A(\vec{Q})$ , of size  $X$  can be fully recovered if its sampling rate is at least at the Nyquist rate of  $\frac{1}{2X}$  – with an *oversampling* of two. Since, we measure the intensity distribution,  $I(\vec{Q})$ , and not the scattered amplitude distribution,  $A(\vec{Q})$ , this rate must be adapted to  $\frac{1}{4X}$ . The Nyquist rate can be translated into a minimum pixel-size in real-space that samples  $I(\vec{Q})$  using the following relation between a discrete Fourier transformation and pixel length along one dimension,  $\Delta_r$  [184]. We note

$$\Delta_r \leq \frac{\lambda L}{4X}, \quad (4.4)$$

with the wavelength  $\lambda$ , the length from the interaction region to the detector  $L$ , and the object length along one dimension  $X$ . This means that larger objects require a more frequent sampling

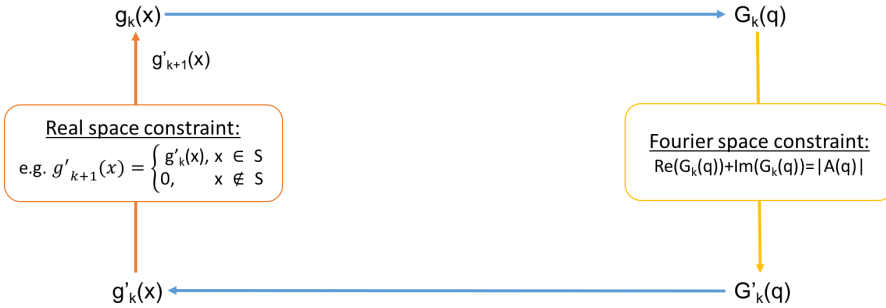


Figure 4.5: Principle of a phase retrieval algorithm. The real space object  $g_k(x)$  is Fourier transformed to  $G_k(q)$ . The function  $G_k(q)$  is altered to fit the constraints set in Fourier space and becomes  $G'_k(q)$ .  $G'_k(q)$  is inverse Fourier transformed to  $g'_k(x)$ . After fulfilling the real space constraints the iterative starts again using  $g'_{k+1}(x)$ . After [185].

of the scattered intensity distribution. If a large, micrometer-sized object is imaged under typical experimental parameters, where  $\lambda = 1.5 \text{ nm}$ ,  $L = 0.371 \text{ m}$ , and  $X = 100 \text{ nm}$ , the detector pixel-size must be  $\Delta_r \leq 1.39 \text{ mm}$  along each pixel dimension to fully recover the particle's projected electron density. In the present experiment, the pnCCD pixel-area of  $75 \mu\text{m} \times 75 \mu\text{m}$  samples also the largest measured objects sufficiently.

### 4.3.1 Principle of phase retrieval

To recover the phase from an oversampled diffraction pattern and thus reconstruct an image of the object, iterative algorithms have been developed [185]. Figure 4.5 illustrates such an iterative algorithm, where the image of an object  $g_k(x)$  is Fourier transformed to reciprocal space  $G_k(q)$  and then inverse transformed again resulting in  $g_{k+1}(x)$ , while sufficing certain constraints.

The constraints are rather strictly defined in the reciprocal space as they have to reproduce the actual measurement  $I = A \cdot A^*$ , which is sometimes called the modulo constraint. The criteria that need to be met in real space can be chosen more freely. Generally, the recovered object should be physical, i.e., should be of a certain (known) size. One can introduce a support structure  $S$  that meets the physical constraints and can therefore be used to, for example, zero outlying values. Throughout the iterations, the functions  $g_k(x)$  evolve and eventually converge into a solution. If one uses the above criterion, one can show that the error between the reconstructions and the actual measurement continuously reduces, which is why it is commonly referred to as error-reduction algorithm [186].

Parameter	Setting
Starting Guess	random phases
Autocorrelation Selection	threshold
Autocorrelatlon Threshold	0.04
Phasing method beta	0.9
Beta range	0 - $\infty$
Enforce positivity	false
Enforce real	false
Perturb weak reflections	false
Phasing algorithm	raar
Blur	12 - 0.7
Blur range	0 - 12000
Center image	false
Object area	0.0022 - 0.0019
Object area range	0-8000
Support update algorithm	area

Table 4.1: Typical parameters used in the Hawk software package. The object area depends strongly on the actual particle size and thus varies.

### 4.3.2 2D reconstructions and image resolution

#### Hawk program for 2D image phase retrieval

For all image reconstructions in 2D, the Hawk software package [187] has been used. Hawk is available under the GNU General Public License<sup>3</sup> and can be downloaded with installation instructions from <https://github.com/FXIhub/hawk>. In previous efforts to retrieve a real-space image from FEL based coherent diffractive imaging, Hawk has been used successfully in several reconstructions ranging from viruses [13, 15] to other few-hundred-nanometer-sized objects [188] but has not yet been used to recover the real space image from rare-gas cluster. The usage of the program is straight-forward in three steps. First, the diffraction images are transformed into the “.cxi” format, which uses HDF5 as base and adopts a variety of other rules to have a uniform format for SPI data-files [189]. Second, diffraction images are prepared in *Hawk’s editor*, where particular effort has to be made to create a pixel mask. The mask prevents shadowed or otherwise faulty pixels from introducing unphysical signals into the reconstruction algorithm. The software suite automatically interpolates between masked pixel regimes, which is acceptable over the length of a few pixels in one direction. Third, *Hawk’s phaser* can be used to iteratively retrieve the phase from the “.cxi” intensity file. Typical parameters for the program can be found in Table 4.1. These parameters are found iteratively and typically require running

---

<sup>3</sup>Hawk copyright: <https://github.com/FXIhub/hawk/blob/master/Copyright>

the phase retrieval of one object various times. This also results in significant demands to the computing environment and it is highly recommended to run the calculations based on a graphics processing unit (GPU), thus making use of Hawk's Nvidia CUDA® support<sup>4</sup>. Therefore, it is worth emphasizing that the *RAAR algorithm* [190] in combination with initially strong *blurs*, the extension of the *phasing beta range*, and a proper determination of the *object area* resulted in useful reconstructions of clusters using Hawk. Note, that the object area size differs from particle to particle and is a sensitive parameter. After  $\sim 15\,000$  iterations, the real space object typically converges.

### Resolution enhancement through combination of rear and front pnCCD

While there is no complete consensus on how to define resolution in a coherent diffractive imaging pattern and the resulting reconstruction, there are various good estimates [15, 191, 192]. A simple and conservative method to define resolution in a diffraction pattern is Abbe's criterion, which comes from microscopy and calculates the minimal resolvable feature size in a diffraction pattern. The fundamental limit that the minimal resolvable feature size is dependent on the wavelength has also given us the inspiration to build short-wavelength machines such as the free electron laser and new synchrotron light sources.

For Abbe's criterion, we must first verify that we are in the far field by fulfilling the following requirement [184]

$$\frac{X^2}{\lambda L} \ll 1 \quad (4.5)$$

with the wavelength of the X-rays  $\lambda$ , the distance to the detector  $L$ , and the object size  $X$ . In this work, the criterion is met.

In the far field, Abbe's criterion can be written down as

$$d_r = \frac{\lambda}{2n \sin(\frac{\Theta}{2})}, \quad (4.6)$$

with the minimal resolvable feature size  $d_r$ , the refractive index  $n$  and the half scattering angle  $\frac{\Theta}{2}$ . The scattering angle is restricted by either the active detector area, which goes back to the typical understanding of a numerical aperture, or the signal intensity up to certain angles. The latter is in interplay with the photon wavelength and object scattering cross-sections.

---

<sup>4</sup>Nvidia is a company that designs GPUs and provides software that interfaces with their chips, such as "CUDA", which is a parallel computing platform.

#### 4 Methods

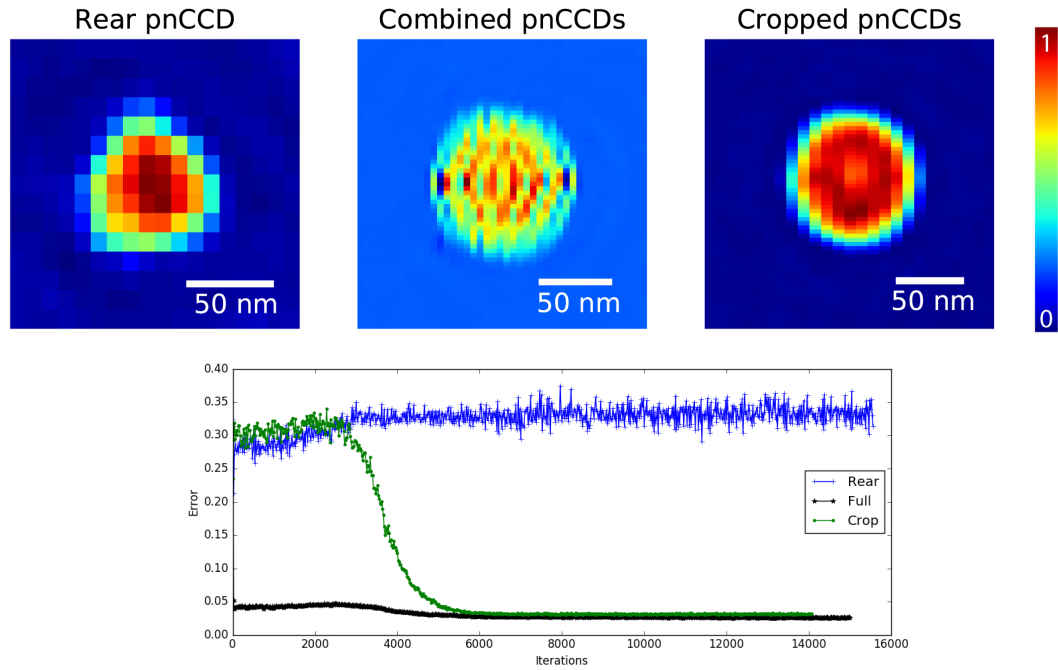


Figure 4.6: Illustration of resolution enhancement due to detector combination. The diffraction pattern in Figure 4.3 of a Xe-cluster has been reconstructed to illustrate several cases. Top left: Rear pnCCD data only reconstruction yields a non-spherical object; error criterion shows no convergence (see bottom graph). Top middle: Front & rear pnCCD data results in a spherical object but missing areas next to the rear pnCCD disturb the reconstruction process, such that the electron density becomes unphysical. Top right: A rectangular cropped diffraction image using areas with significant photon signal enables a physical reconstruction.

### 4.3 Phase retrieval from a single diffraction pattern

In the far field, we can use the following relation to determine the actual size of a pixel,  $\Delta_s$ , in a recovered real space image of an object. We note [184]

$$\Delta_s = \frac{\lambda L}{N\Delta_d}, \quad (4.7)$$

with  $L$  being the length from the interaction region to the detector,  $\Delta_d$  being the linear detector pixel size, and  $N$  being the side length of the discrete detector array.

Figure 4.6 top shows several reconstructions of a xenon cluster at  $\lambda = 1$  nm using different portions of the diffraction pattern in Figure 4.3. If just the rear pnCCD is used for reconstructions, a maximum scattering angle of  $\Theta \approx 4.2^\circ$  is recorded, which results in a minimal resolvable feature size of  $d_r \approx 14$  nm. However, in the present data a shadow from the front detector is cast on the rear detector. This reduces the maximum scattering angle in the image **Rear pnCCD** that can be found in the top left panel of Figure 4.6 to  $\Theta \approx 3.8^\circ$  and thus the resolution to  $d_r \approx 15$  nm. The pixel size is  $\sim 10$  nm  $\times$   $\sim 12$  nm. The image **Combined pnCCDs** of Figure 4.6 uses the whole data including the empty areas next to the rear pnCCD. The image shows an unphysical electron density distribution, which originates from the empty areas next to the rear pnCCD data. In these areas, which have been masked out, the interpolation along the  $Y$ -axis and the extrapolation along the  $X$ -axis fails. The next image labeled **Cropped pnCCDs** in Figure 4.6 uses data in its full extent along the  $Y$ -axis but is cropped along the  $X$ -axis such that the blank areas are excluded. The reconstruction converges into an object that appears physical. The maximum scattering angle here is  $\Theta \approx 9.2^\circ$  and the resolution thus  $d_r \approx 6$  nm. The pixel-size here is  $\sim 10$  nm  $\times$   $\sim 3$  nm.

This is a factor  $\sim 5$  improvement over common cited studies in single particle imaging [13] and still a factor  $\sim 3$  better than [193], where measured diffraction patterns have been “computationally purified”. The resolution enhancement due to the combination of detectors can be exploited further using expand-maximze-compress (EMC) algorithms [194]. EMC algorithms arrange multiple diffraction patterns according to their orientation and are thus able to compute averaged 3D diffraction patterns of a few hundred diffraction images of identical objects. When conducting an experiment in the LAMP end-station, the missing areas next to the rear pnCCDs could be populated in such an averaged diffraction image since the object is imaged at random orientations. Ultimately, this allows 3D reconstructions of nanoparticles with nanometer resolution<sup>5</sup>.

---

<sup>5</sup>Depending on the position of the front pnCCD.

### 4.3.3 1D projections and phase reconstructions

The main goal of reconstructions in this thesis is to recover an image of the object while it undergoes the nanoplasma formation and expansion. The effects of the nanoplasma evolution on the spherically symmetric cluster can be considered isotropic [21]. It is thus useful to display diffraction patterns and projected electron densities in one dimension to simplify the comparison of the transient states. A 1D representation of the data allows furthermore the comparison to analytical models. To reduce the 2D diffraction data to 1D the program shown in Appendix 2 has been employed. It is based on MATLAB, which efficiently iterates through pixel arrays. The input for this program are pedestal-calibrated diffraction images that have a true image center defined. Key elements of the algorithm are: iterating through every pixel, filtering signal from noise, disregarding missing areas, determining the scattering angle of every pixel, and adding signal over  $|\vec{Q}|$ , while normalizing the data over the pixel number. To recover the object in real space, an algorithm has been designed to perform phase retrieval on the 1D data. The algorithm follows the fundamental scheme described in Section 4.3.1 and is shown in Appendix 3. Thereby, the real space data of the object is forced to be real and positive, which is also the error criterion in real space. The difference to the measured data yields the error criterion in Fourier space. The algorithm allows monitoring of the Fourier and real space error, the phase and the actual Fourier and real space images. The iterative algorithm is aborted when the error criterion meets a predetermined threshold.

## 4.4 Impact of the X-ray pump–X-ray probe on diffraction pattern

For the X-ray pump–X-ray probe diffractive imaging experiment of this thesis, both pulses contribute to the scattering image. But, in this thesis experiment, only the diffraction image from the probe-pulse is interesting. This is why the pump-pulse was set to  $\sim 10\%$  of the overall pulse energy, and therefore, the pump-pulse did not contribute significantly to the diffraction image. However, in order to simulate the effects of the pump-pulse to the diffraction image, a 1D simulation is conducted using electron densities of spheres,  $\rho(R)$ . At our present resolution the cluster can be well-simulated using spheres (see Section 2.3.2). To simulate the radiation damage that is induced by the pump-pulse, the spheres are allowed to undergo a surface softening. This can be simulated by an exponential decay according to the model described in [21], although, it should be noted that more recent theoretic investigations show that the electron density expansion

#### 4.4 Impact of the X-ray pump–X-ray probe on diffraction pattern

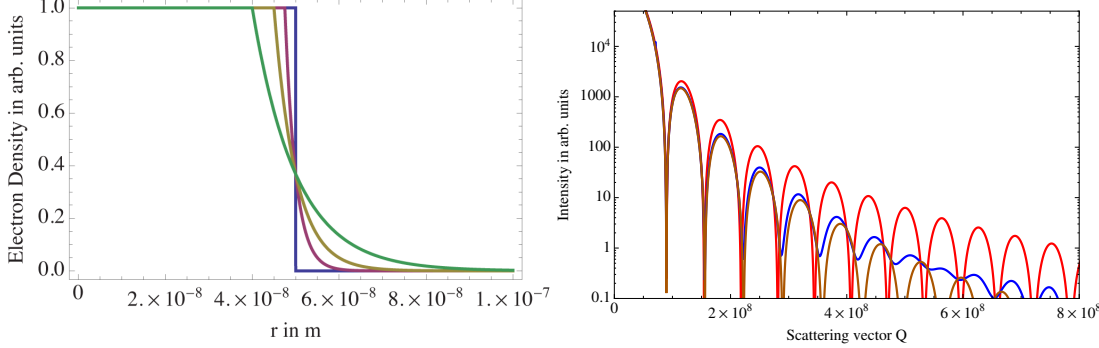


Figure 4.7: Electron density of spheres that show surface softening (left) and resulting scattering patterns (right). In the right panel, the red line is the scattering of an intact sphere, the brown line is the scattering of an expanding sphere with  $k = 5 \text{ nm}$ , and the blue line shows the combined scattering of an intact and expanding sphere that has been pumped with 10 % and probed with 90 % of the overall pulse energy.

can be better estimated using a Fermi-function [125]. We write,

$$\rho(R, k) = \begin{cases} 1 & \text{for } r - k \geq R \geq 0, \\ e^{\frac{(r-k)-R}{k}} & \text{for } r > R - k, \end{cases} \quad (4.8)$$

where  $r$  is the cluster radius,  $R$  is the distance from the center of the cluster, and  $k$  an expansion parameter such that

$$\int_0^\infty \rho(R, k) dR = r, \quad \text{if } 0 < k < r. \quad (4.9)$$

The electron density can then be Fourier transformed into reciprocal space using the transformation in 1D due to the symmetry. With the spatial frequencies,  $Q$ , we may note [115]

$$I(Q) = I_0 F^2(Q) = I_0 \left( \int_0^\infty \rho(R, k) \frac{\sin(QR)}{QR} 4\pi R^2 dR \right)^2, \quad (4.10)$$

where an incident beam has the intensity  $I_0$ . This 1D simulation enables us to simulate electron densities of intact and expanding clusters and we can Fourier transform these electron densities into reciprocal space to compare it to measured diffraction images. The left panel of Figure 4.7 shows the electron densities for  $r = 50 \text{ nm}$  and  $k = (0, 2.5, 5, \text{ and } 10) \text{ nm}$ . The right panel of Figure 4.7 showcases corresponding cases of expanding spheres in reciprocal space. The red line is the scattering of a solid sphere,  $F_{\text{intact}}^2$ , with  $r = 50 \text{ nm}$  and  $k = 0 \text{ nm}$ . The brown curve is the scattering of an expanding sphere,  $F_{\text{expanding}}^2$ , with  $r = 50 \text{ nm}$  and  $k = 5 \text{ nm}$ . Lastly,

#### 4 Methods

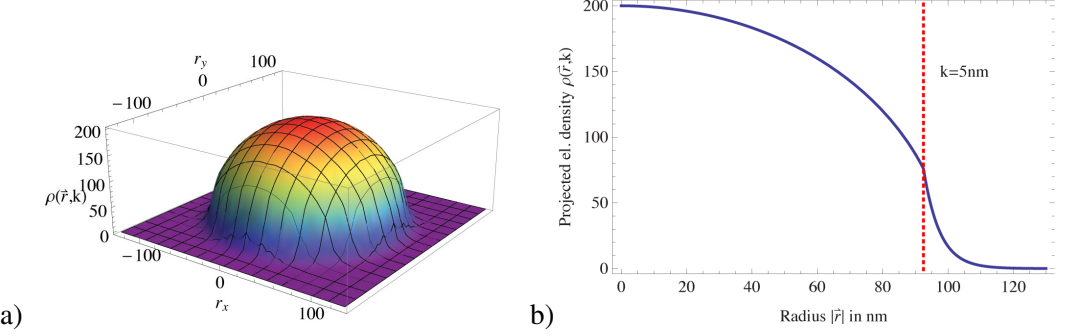


Figure 4.8: a) Electron density of a  $R \approx 100$  nm expanding sphere with  $k = 5$  nm, projected onto a 2D plane. b) Blue curve, spherical projection of the 2D simulation to 1D. Red dashed line, point of expanding density at  $k = 5$  nm.

the blue curve is comparable to the case of this experiment. Here, the electron densities of an intact and expanding sphere were Fourier transformed and multiplied with the incident beam intensities corresponding to the pump- and probe-pulse. So, 10 % of the overall intensity,  $I_0$ , is in the pump-pulse and 90 % is in the probe-pulse. The transformation in reciprocal space thus reads,  $I_0 F^2 \rightarrow 10\% \cdot I_0 F_{\text{intact}}^2 + 90\% \cdot I_0 F_{\text{expanding}}^2$ . Here, the pump-pulse affects the diffraction pattern at high  $Q$ -values and decreases the fringe contrast. However, the added signal from the pump-pulse remains within the noise level of  $I(Q) < 1$  ADU. For this assessment, the simulated incident beam intensities,  $I_0$ , and cluster radius,  $r$ , have been fitted to match the experimental data of Figure 4.4.

#### 4.5 2D electron density and diffraction image simulations

For the interpretation of the HeXe-cluster data that are discussed in the following chapter, 2D simulations were performed. These simulations model sphere-based electron densities of clusters and core–shell systems, and compute corresponding diffraction patterns. The simulations can be compared to the measured diffraction images or the reconstructed real-space images of HeXe-clusters. The results of the simulations support the analysis of experimentally measured data and the simulations furthermore allow the modeling of several thought-experiments, such as simulating various structures of the core–shell systems and comparing it to the experimental data. The 2D data of the simulations can optionally be reduced to 1D using a spherical integration (see Section 4.3.3) to be compared to the experimental data or analytical models. The clusters and core–shell systems are approximated using spheres, which is an acceptable estimation of the icosahedral cluster structure at the current resolution. The simulations are discussed in detail below.

For the core–shell systems in this thesis, the simulated spheres should reflect the recorded HeXe-clusters (see Figure 5.16) and should therefore be adjustable in density, have various radii, be placed at varying locations, and should be allowed to exhibit a surface softening. Similar to Section 4.4 and Reference [21] can we express the electron density of a single sphere that has been projected onto a 2D plane using the formalism

$$\rho(\vec{R}, k) = \begin{cases} 2\sqrt{r^2 - |\vec{R}|^2} \cdot \rho_0 & , \text{ for } r - \frac{3k}{2} \geq |\vec{R}| \geq 0, \\ 2\sqrt{r^2 - |\vec{R}|^2} \cdot \rho_0 e^{\frac{(r - \frac{3k}{2}) - |\vec{R}|}{k}} & , \text{ for } r > |\vec{R}| - \frac{3k}{2}, \end{cases} \quad (4.11)$$

with  $\rho_0$  being the density,  $r$  being the cluster radius, and  $k$  an expansion parameter. In the 2D projection of the particle, the exponential surface softening was modified to fulfill

$$\int_0^\infty \rho(|\vec{R}|, k) d\vec{R} = r, \quad \text{if } 0 < k < r. \quad (4.12)$$

This sphere can be positioned arbitrarily in a 2D array, which simulates the real space image, using  $\vec{R} \rightarrow \vec{R} - \vec{R}_0$ , with  $\vec{R}_0$  being the center of mass of the sphere. From here, it is simple to construct the desired real space core-shell system. The electron densities of multiple spheres consisting of arbitrary radii and densities can be added together onto the 2D array. In these simulations, the density  $\rho_0$  was set to  $\rho_{0,\text{helium}} = 1$  for liquid helium and  $\rho_{0,\text{xenon}} = \frac{3.640}{0.1412} \approx 25.8$  for xenon, with the numerator of the fraction for  $\rho_{0,\text{xenon}}$  is the density of bulk xenon in g/cm<sup>3</sup> and the denominator is the density for liquid helium in g/cm<sup>3</sup>. Multiple spheres were arranged on a large array of  $\sim 1500 \times \sim 1500$ , which is comparable to the combined pnCCD image array size. The array is then Fourier transformed using MATLAB’s function *fft2*, the output is rearranged using the function *fftshift*, and squared.

As an example of a simulation, Figure 4.9 shows a comparison of the analytical derived scattering of a sphere (see Equation (2.41)) with a radius of  $r = 202$  nm (black, dashed line) and the scattering of the 2D simulations that has been reduced to 1D (green, solid line). The red curve is the envelope of the functions or Porod’s law. The developed simulation agrees well with the analytical scattering, when  $k = 0$ .

## 4.6 Data filtering

As described in Section 4.1, LCLS produces large amounts of data with a variety of shot-to-shot intensity and therefore a data range. To analyze comparable events, the data have to be filtered, which is often referred to as *hit-finding* [52, 106, 195]. Typical for single particle imaging is to

## 4 Methods

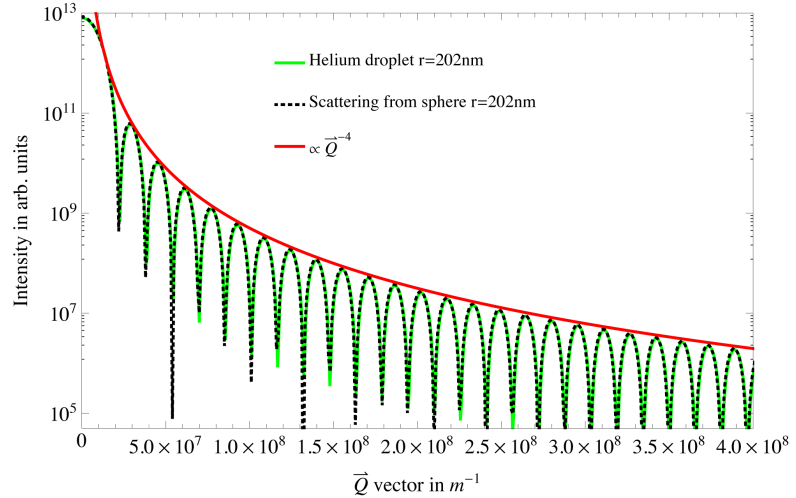


Figure 4.9: Comparison of analytical scattering from a sphere of radius  $r = 202$  nm (black curve), Equation (2.41), and scattering of a sphere of radius  $r = 202$  nm from 2D simulations projected onto 1D (green, dashed curve). The envelope of scattering intensity of a sphere (Porod's law) is  $\propto |\vec{Q}|^{-4}$  (red curve). The analytical scattering and developed simulations agree well with each other.

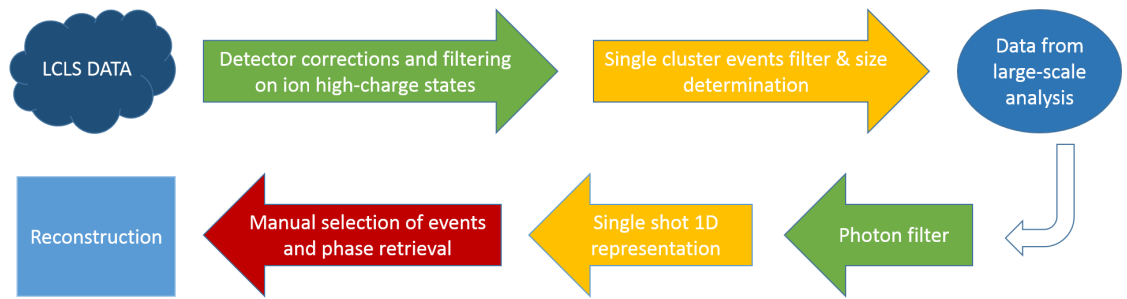


Figure 4.10: Schematic of data treatment and hit-finding procedures.

filter on events, where many photons have been captured by the detector. The difficulty for this work is that the sample dynamically evolves due to the pump-pulse. Figure 5.8 showcases some of these dynamic processes in Xe-clusters and the data show that as the Xe-clusters undergo a nanoplasma expansion the scattered intensity decreases (details described later in Section 5.2.1). This can be extrapolated to an extreme, where a cluster that has been intensely hit undergoes a nanoplasma expansion and therefore produces barely any signal on the front pnCCD. Fortunately, a cluster that has been intensely hit results in ion high-charge states and we can make full use of the coincident detection of diffraction image and time-of-flight trace. Figure 4.10 shows a flow chart of the data treatment. Initially, the data have been automatically filtered on ion high charge states using the time-of-flight signal. This resulted in several hundred to thousands events per pump-probe delay step. These hits were semi-automatically filtered on single cluster hits, which also allowed determining their size using the first maxima as described in Section 2.3.2. This reduced the data significantly to, for example, 350 single Xe-cluster events over all delay steps. Some results of this procedure for Xe-clusters are shown in Figure 5.8 and the data shows that Xe-cluster exhibit a linear average-Xe-cluster-radius increase of  $\sim 20\%$  over the course of the first 800 fs (see more in Section 5.2.1).

To perform phase retrieval and to solve the inverse problem, bright hits containing many photons are required. Therefore, another filter has been implemented that automatically filters for events with much scattered intensity. The  $\sim 30$  remaining diffraction images of single Xe-cluster events per delay step have then been semi-automatically displayed in a 1D representation and compared to the scattering of a sphere. Now, events containing dynamics became obvious and the brightest hits that show signs of X-ray radiation damage have been selected manually for phase-retrieval. The phase-retrieval is an intractable process that not always resulted in physical recovery of the object, which lead to further exclusion of events. The He- and HeXe-cluster data have been treated in the same way as the above discussed example of Xe-clusters.



## 5 Results and discussion

Data from previous experiments [20–22], where diffraction images and time-of-flight data were recorded in coincidence, show that the diffraction images carry transient information about the nanoplasma formation and expansion. The time-of-flight spectra contain valuable information about the atomic ionization as well as expansion dynamics from large ionized clusters and are therefore briefly discussed first in Section 5.1. The scattering response of the clusters to intense X-ray pulses is discussed in the following in Section 5.2.

For the hasty reader the organization of the subsections may be helpful: Section 5.1.1 discusses the time dependent response of Xe-atoms and -clusters to X-ray pump–X-ray probe beams in the ion TOF data. Section 5.1.2 continues the ion TOF data discussion on superfluid He- and mixed HeXe-clusters. Section 5.2.1 covers the scattering response of pristine Xe-clusters. Section 5.2.2 discusses the nanoplasma expansion of He-clusters in intense X-rays. Section 5.2.3 addresses the agglomeration of heterogeneous HeXe-clusters and introduces the plum-pudding cluster model. Section 5.2.4 discusses sample damage in HeXe-clusters using 2D-simulations. Section 5.2.5 compares radiation damage of Xe-, He- and HeXe-clusters in intense X-rays to each other.

The X-ray pulse parameters of this study are summarized in Table 3.1 on Page 48. It should be noted again that the split of the multipulse energy is 10 % in the pump-pulse and 90 % in the probe-pulse. This allows us to neglect the contributions of the pump-pulse to the scattering images (see Section 4.4).

### 5.1 Ion time-of-flight X-ray pump–X-ray probe data

#### 5.1.1 Time-dependent response of Xe-atoms and -clusters to intense X-rays

For the interpretation of the dynamic data from Xe- and HeXe-clusters it is first important to establish how individual atoms respond to a X-ray pump–X-ray probe experiment. Ion time-of-flight traces of atomic xenon at various time delays  $\Delta t = (0, 120, 250, 400, \text{ and } 800)$  fs and X-ray pump-pulse only data are shown in Figure 5.1. All TOF traces below are averages of the  $\sim 10\%$  most intense hits of the respective run. The time-of-flight data indicate a resonant-like

## 5 Results and discussion

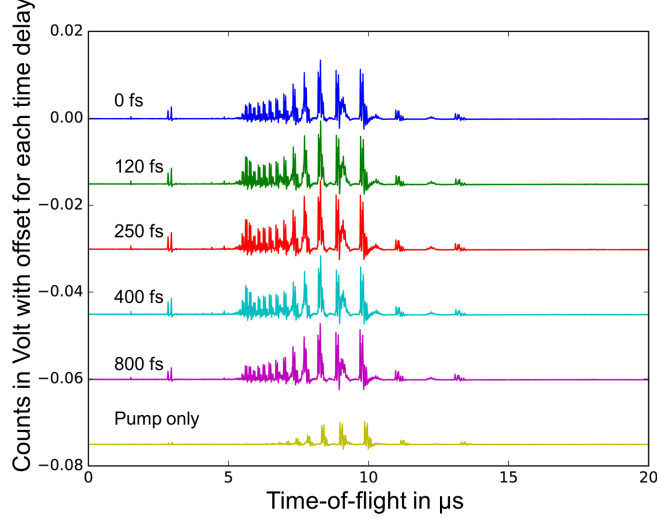


Figure 5.1: Time-resolved answer of xenon atoms in TOF mass spectroscopy. The Xe-atom response to the X-ray pump–X-ray probe pulses from LCLS shows a resonant behavior in the high-charge states that peak at  $\sim 250$  fs (see also Figure 5.2).

behavior in the time-domain as the atomic xenon high-charge states peak at  $\Delta t \approx 250$  fs with a clear increase. This is also shown in Figure 5.2, where the total high-charge state ion-yield for Xe-atoms between the TOF range (5.13 to 6.50)  $\mu$ s is plotted as a function of the time delay,  $\Delta t$ . The charge-state composition is highly dependent on the X-ray absorption process. For highly intense X-ray pulses, absorption is a complicated process involving multi-photon core-hole excitations and decay processes. Further theoretic investigations are needed to explain the spectra in more detail [114, 118]. However, this resonant-like effect could be related to intensity-induced X-ray transparency [19, 121]. In this thesis experiment, the xenon 3d-subshell is efficiently photoionized by the X-ray pump-pulse. The resulting electron-holes in the 3d-subshell are typically repopulated on the few femtoseconds timescale due to the Auger decay, but the increasingly ionized atoms have also increasingly longer hole lifetimes, for example, previous studies show that  $\text{Ne}^{8+}$  has core-hole lifetimes of  $\sim 230$  fs [19] making the atom increasingly transparent during the vacancy lifetime. In the present case, the absorption of photons from the probe-pulse is suppressed for delays  $\Delta t \leq 120$  fs because of this transparency. When the delay is  $\Delta t = 250$  fs, the xenon 3d-subshell repopulates and the probe-pulse can efficiently photoionize the 3d-subshell again. But, why does the charge state distribution not level out for later delays  $\Delta t > 250$  fs? When the strongly pumped atom does not absorb energy near saturation, decay processes catch up and the nanoplasma dissipates energy in surrounding media. Subsequent recombination then could lead to less intense high-charge state populations.

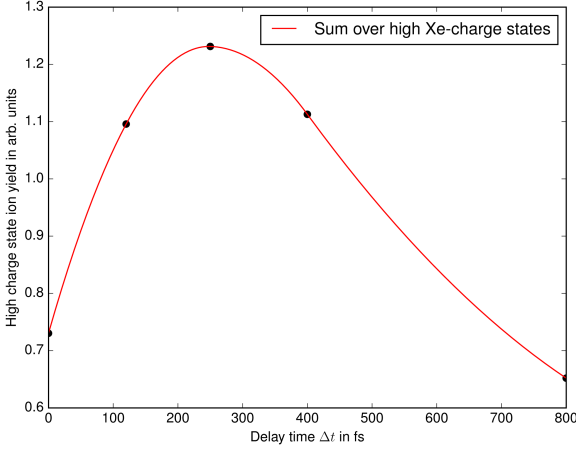


Figure 5.2: The total of the high-charge state ion-yield for Xe-atoms between the TOF range ( $5.13$  to  $6.50$ )  $\mu$ s or ( $\sim \text{Xe}^{17+}$  to  $\text{Xe}^{10+}$ ) as a function of the time delay,  $\Delta t$ . The atomic Xe-ion TOF data show resonant behavior. As the time delay is varied in the range  $\Delta t = (0$  to  $800$ ) fs, the high-charge states of atomic Xe-ions peak at  $\sim 250$  fs.

The response of clusters to highly intense X-ray radiation is more complex. Size-dependent ionization [121, 196] and recombination in the nanoplasma [197] alter the sample’s ionization pathways. Ion time-of-flight traces of Xe-clusters are displayed in Figure 5.3. The time delay has been set to  $\Delta t = (0, 60, 120, 250, 400,$  and  $800)$  and also the pump only data is shown. The mean radius of the initially injected Xe-clusters are  $\sim 61$  nm but they will expand by  $\sim 20\%$  over a  $\Delta t$  range of (0 to 800) fs as discussed later in Section 5.2.1. Unlike the atomic xenon data, the Xe-clusters show no clear resonant-like effect. The Xe-cluster data indicate a weak time-dependence of ionization and with increasing  $\Delta t$ , the high-charge states overall increase. This can be attributed to the expanding cluster. During the expansion, the cluster potential lowers [122] and the electron transition dynamics become more complex [198]. To describe the time-dependent ionization of clusters in detail, a theoretic investigation that is beyond the scope of this thesis is needed and ongoing [118].

### 5.1.2 Time-resolved response of He- and HeXe-clusters in intense X-rays

He-droplets exhibit a weak response to the X-ray pump–X-ray probe delay similar to the Xe-cluster. Figure 5.4 shows ion time-of-flight data of pristine He-cluster at pump–probe delays  $\Delta t = (0, 250,$  and  $800)$  fs. The pristine He-droplets have an average radius of  $r_{\text{He}} \approx 810$  nm that has been derived from the cluster growth scaling laws (see Section 2.2.1). The data show an overall similar behavior regardless of the delay  $\Delta t$ , although minor changes in the charge fragmentation

## 5 Results and discussion

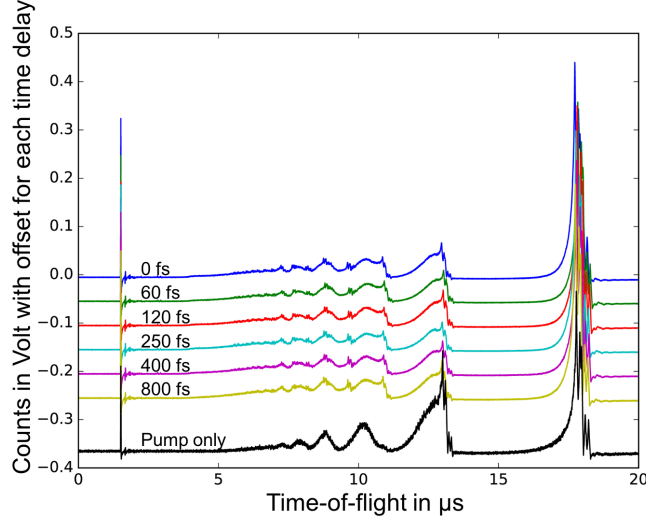


Figure 5.3: Time-resolved answer of xenon clusters in TOF mass spectroscopy. Unlike the atomic response, Xe-clusters show no clear resonance and overall have a weak time dependence.

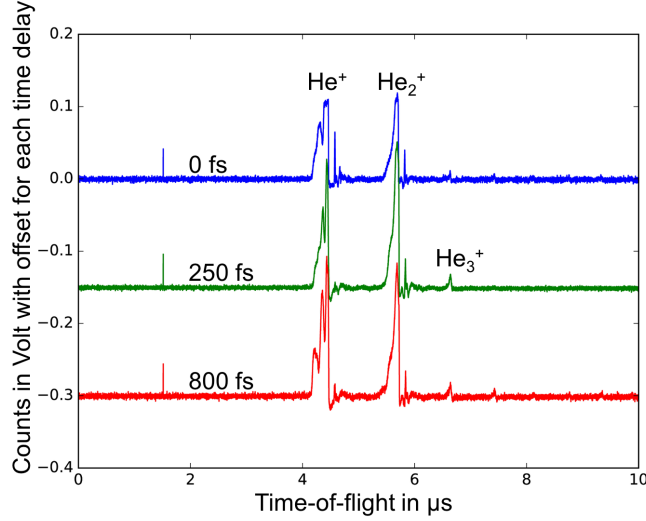


Figure 5.4: Ion time-of-flight traces of He-cluster with a radius of  $r_{\text{He}} \approx 810 \text{ nm}$ . Although minor changes in the charge fragmentation are observed, we shall note that there are no  $\text{He}^{2+}$  ions in this data. The absorption cross-section of helium are too low to lead to doubly-charged states [118].

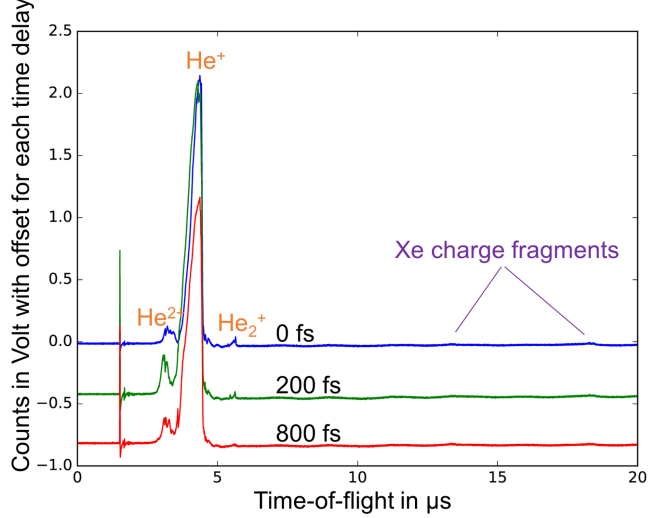


Figure 5.5: Ion TOF spectra of HeXe-cluster with radius  $r \approx 600\text{ nm}$  and a Xe-doping level of  $\sim 0.6\%$ . Only negligible contributions from Xe-charge-fragments are observed. Conversely, doubly-charged  $\text{He}^{2+}$ -ions are detected and the kinetic energy release of the He-peaks varies. With increasing delay time, the He-ions reveal a time-dependence.

distribution can be seen. The He-data is shown for comparison to the HeXe-cluster data presented below. For the comparison, it is important to note that the TOF traces indicate no contribution of doubly-charged helium atoms. The lack of double-charged helium can be explained by the comparably low absorption cross-sections of helium (see Table 2.3) [118].

Next, HeXe-cluster with a radius of  $r_{\text{He}} \approx 600\text{ nm}$  and a  $\sim 0.6\%$  doping level of xenon are discussed. For clarity, this is measured through the helium depletion measurement, which was discussed in Section 2.2.2. At this doping level, the helium depletion is  $\sim 62\%$ . The TOF spectra are shown in Figure 5.5 for the delays,  $\Delta t = (0, 200, \text{ and } 800)\text{ fs}$ . Most notable is the presence of  $\text{He}^{2+}$  ions and the strongly increased signal from  $\text{He}^+$  ions. But, only few xenon charge fragments are observed. This is counter-intuitive as the absorption cross-section from xenon is much larger than from helium (see Table 2.3). We can therefore hypothesize that ultrafast charge-transfer occurs between the Xe-particles and the He-droplets [34]. The He-droplet functions as electron reservoir for the Xe-clusters and therefore they can recombine. The neutral Xe-particles are not detected by the ion TOF spectrometer and barely any signal of Xe charge fragments is detected [30, 34]. The absence of Xe charge fragments indicates also the sample integrity of the Xe-particles. As we look at the longer delays  $\Delta t$ , it is interesting that the He-ion signals of the

## 5 Results and discussion

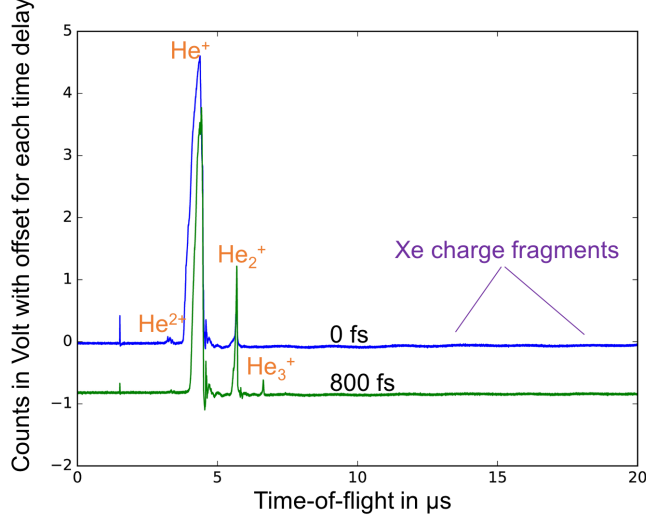


Figure 5.6: Ion TOF spectra of HeXe-cluster with radius  $r \approx 775$  nm and a  $\sim 0.06\%$  xenon doping level. These weaker doped HeXe-clusters show a lower  $\text{He}^{2+}$ -ion count and kinetic energy release. Barely any Xe-ions are detected.

HeXe-clusters show a strong time-dependence. Similar to the atomic xenon data, we observe that the He-ion signal shows a resonant-type behavior and at  $\Delta t = 200$  fs, the signals from  $\text{He}^{2+}$  and  $\text{He}^+$  peak. We can make use of the earlier discussion around the data shown in Figure 5.2 and 5.4 and conclude that this resonant-like behavior does not originate from the absorption and ionization dynamics of the He-droplet but rather from the Xe-atoms with which the He-droplet is doped. This allows us to hypothesize that there must be an ultrafast kinetic energy transfer process as charge-transfer alone does not explain the increase in kinetic energy of the He-ions [34, 199, 200]. For example, collisions could transfer energy from the Xe-particles to the He-droplet. This thought can be expanded and it is theoretically predicted that electron-electron collisions of trapped electrons in the cluster potential occur frequently [122]. These collisions could be responsible for this energy exchange. This indication of trapped electrons is interesting because these electrons damage the sample due to secondary collisional ionization [29] and we will discuss some implications for diffractive imaging below. Note that the He-dimer signal decreases steadily, which can be attributed to the nanoplasma formation. The weakly bound He-dimer bonds will break as a result of the ionization and increased kinetic energy, such that they contribute, for example, as  $\text{He}^+$ -ions to the TOF data.

If the He-ion composition is strongly driven by the doped Xe-atoms, one would expect a dependence on the Xe doping-level. Therefore, He-droplets with a radius of  $r \approx 775$  nm and a  $\sim 0.06\%$

doping are discussed next. This is a  $\sim 10$  times less doping than the above discussed data and the  $\text{He}^{2+}$ -ion signal should therefore be less intense and broad to support the hypothesis. For completeness, the helium depletion is  $\sim 13\%$ . Figure 5.6 shows the ion TOF data at delays  $\Delta t = (0 \text{ and } 800) \text{ fs}$ . We note, again, the presence of  $\text{He}^{2+}$  ions and an increased signal from  $\text{He}^+$  ions. Although the He-droplet is larger, the  $\text{He}^{2+}$ -ion peak is clearly less intense and less broad than the above data with stronger Xe-doping. Xe-ions are barely detected. These data support the hypothesis that the Xe-particles drive the He-ionization through the above discussed processes. The detection of the initially photoionized xenon is more suppressed than in the above data through recombination effects and a larger electron reservoir. By varying the time delays  $\Delta t$ , the height of each He-ion peak shifts and a time-dependence is clearly visible. The  $\text{He}^{2+}$  and  $\text{He}^+$  states become less intense, but a stark increase in  $\text{He}_2^+$  and  $\text{He}_3^+$  peaks is observed. This could be a sign of a less violent nanoplasma expansion, where charge fragments not fully disintegrate into their atomic components, i.e.,  $\text{He}^{2+}$ -ions, than in the above strongly doped data.

In summary, pristine He-droplets show little time-dependence as  $\Delta t$  is varied and mostly singly-charged  $\text{He}^+$ - and  $\text{He}_2^+$ -ions are measured. If the He-droplets are doped with xenon, doubly-charged  $\text{He}^{2+}$ -ions are detected, the kinetic energy release is stronger, and the time-of-flight data reveal a He-ion time-dependence that is comparable to the one of Xe-atoms. As the Xe-doping is decreased, the presence of  $\text{He}^{2+}$  ions becomes less frequent. This HeXe-cluster data indicates that the ionization dynamics of the He-ions are driven by the encapsulated Xe-atoms. A charge transfer from the initially photoionized Xe-atoms to the He-droplet is likely the dominating process leading to these TOF traces. This has also been shown previously theoretically [30] and in static studies [34, 199, 200]. If the HeXe-cluster TOF data is compared to the pristine Xe-cluster TOF data, it becomes obvious that the Xe-particles preserve their integrity better when they are encapsulated in a He-cluster [34, 199, 200].

## 5.2 Scattering response of rare-gas clusters

### 5.2.1 Structural damage in Xe-clusters induced by intense X-rays

XFELs can create high-quality diffraction images from single particles. All diffraction images carry transient information of the sample during the pulse [20]. In a pump-probe experiment, time-resolved structural information can be extracted from the diffraction images, such as the surface softening of the nanoplasma [21]. This thesis experiment follows the X-ray induced nanoplasma expansion up to 800 fs for the first time. To start out, 30 to 60 diffraction images per delay step from Xe-clusters are analyzed (see Section 4.6) and their radius is determined. This leads to a high-throughput evaluation of several hundred clusters, whereby Equation (2.41) is

## 5 Results and discussion

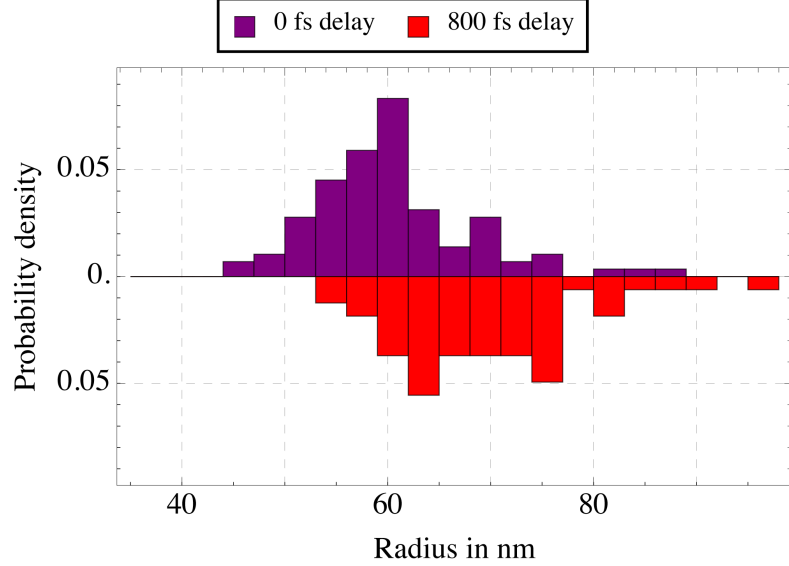


Figure 5.7: Size evaluation of  $\sim 30$  single Xe-cluster hits per time delay  $\Delta t$  step. At  $\Delta t = 0$  fs, the size distribution follows in approximation an expected log-normal distribution. At  $\Delta t = 800$  fs the distribution broadens and shifts towards larger radii due to the nanoplasma transition.

exploited to automatically fit diffraction images.

Supersonic gas jets always produce a distribution of cluster sizes (see Section 2.2.1). Such a distribution of cluster radii is shown in Figure 5.7 for the X-ray pump–X-ray probe time delays,  $\Delta t = (0 \text{ and } 800)$  fs. The size distribution of Xe-clusters follows a log-normal distribution [201] and for  $\Delta t = 0$  fs, the mean cluster radius is 61 nm. When the imaging pulse is delayed by  $\Delta t = 800$  fs, the mean cluster-radius increases to 74 nm and the size-distribution becomes broad. This can be clearly attributed to the nanoplasma expansion. The Xe-cluster size distribution may become more broad due to a distribution of the pump-pulse power density. Shot-to-shot fluctuations result in different nanoplasma expansion speeds,  $v_{\text{exp}}$ , as discussed below.

A summary of the of the Xe-cluster radii increase over several pump–probe delay steps can be found in Figure 5.8. The mean radii and standard deviations of the log-normal distributions are plotted for  $\Delta t = (0, 120, 250, 400, \text{ and } 800)$  fs and fitted linearly. These data suggest that the nanoplasma expansion speed,  $v_{\text{exp}}$ , is rather constant over the observation window. Theoretical studies of nanoparticles [26, 29, 35] predict that the expansion speed indeed becomes constant after a few ten femtoseconds, which the system needs to thermalize. We can determine the expansion speed using the mean increase of cluster-radii over  $\Delta t = (0 \text{ and } 800)$  fs and note

## 5.2 Scattering response of rare-gas clusters

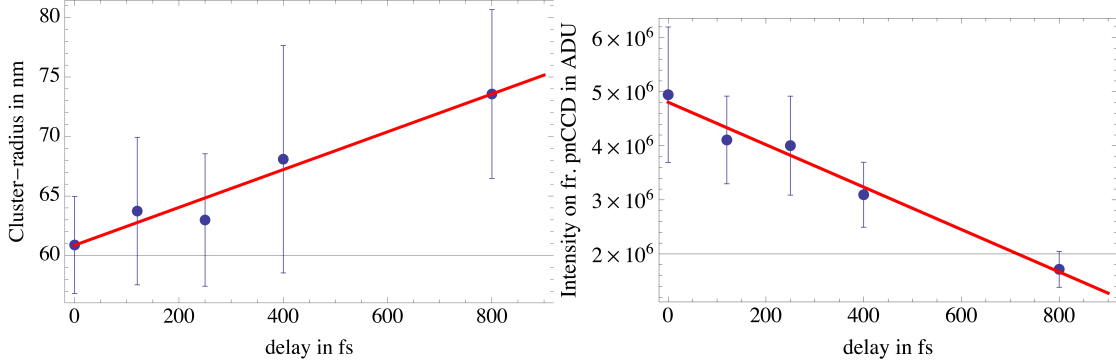


Figure 5.8: Average xenon cluster size of intense hits as a function of pump–probe delay  $\Delta t$  (left panel). Average intensity on the front pnCCD of intense single-shot hits from single Xe-cluster as a function of the pump–probe delay  $\Delta t$  (right panel).

$v_{\text{exp}} \approx 15\,250 \text{ m s}^{-1}$ . This indicates that Xe-nanoparticles that are irradiated with typical LCLS pulses undergo a violent and rapid explosion.

We can use the expansion speed to estimate the electron temperature of the nanoplasma, as it has been done similarly before [52]. Thereby, we should note that the electron gas of the nanoplasma thermalizes with the ions on the few femtoseconds time-scale and follows a Maxwell-Boltzmann distribution [122]. If we now find a temperature for the Maxwell-Boltzmann distribution that has the expansion speed,  $v_{\text{exp}}$ , as mean velocity, we can estimate the electron temperature to be  $\sim 125 \text{ eV}$ . This compares to temperatures that can be found inside the sun.

We can also compare the electron temperature to a similar NIR pump–X-ray probe nanoplasma study on Xe-clusters [21], where electron temperatures of  $\sim 200 \text{ eV}$  have been found. The difference in electron temperature and expansion speed is attributed to the difference between the NIR and X-ray pump-pulse parameters and the corresponding absorption cross-sections. The NIR pump-pulse has a wavelength of 800 nm, a focal spot size of  $1600 \mu\text{m}^2$ , and power densities of  $\sim 10^{15} \text{ W cm}^{-2}$  [21]. The X-ray pump-pulse in this study has a wavelength of 1.5 nm and power densities of  $\sim 2 \cdot 10^{16} \text{ W cm}^{-2}$ . The NIR strong-field absorption cross-section of a xenon atom can be estimated to be  $\sim 30 \text{ Mb}$  using the above power densities (from Reference [37, p. 1826]), and the X-ray absorption cross-section for atomic xenon is  $\sim 3 \text{ Mb}$  (from Figure 2.13). Let us perform a very simplified cross-section estimation similar to Equation (2.2) using 25 nm radius Xe-clusters. Given the above parameters, this estimation indicates that a Xe-cluster would absorb  $\sim 93 \text{ keV}$  in the NIR and  $\sim 79 \text{ keV}$  in the X-ray wavelength region. The relative absorbed energy in X-ray versus NIR is  $\frac{79 \text{ keV}}{93 \text{ keV}} \approx 85 \%$ . This relative difference can be compared to the relative difference in electron temperatures of the X-ray– vs. the NIR–study, which is  $\frac{125 \text{ eV}}{200 \text{ eV}} \approx 63 \%$ .

## 5 Results and discussion

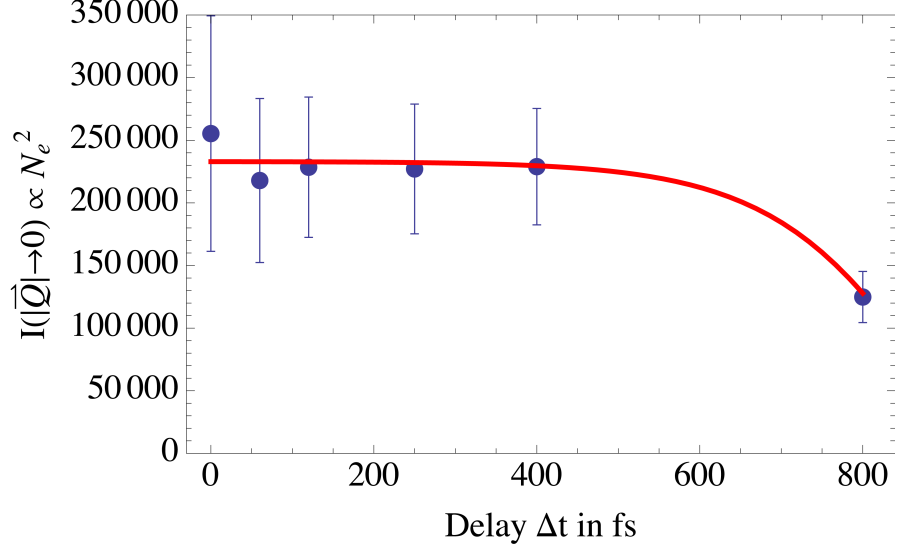


Figure 5.9: Scattered intensity  $I_0$  in arb. units at  $\vec{Q} \rightarrow 0$  of Xe-clusters. This is proportional to the total number of scatterers squared,  $N_e^2$ . The red curve is a guide for the eye (see Section 5.2.1).

Given this estimate, it is clear why the electron temperature in the NIR study is higher than in the here presented X-ray study. It is noted that, for example, transient scattering factors and cluster cooling processes [37] do play a significant role in this absorption process, which do vary the actual absorbed energies drastically [37] and are disregarded in this simplified estimate.

Let us continue by looking at the time-dependent behavior of electrons. During the pulse the cluster is increasingly ionized, the Coulomb potential deepens, and eventually electrons from photoionization processes are efficiently trapped [122]. On a larger timescale, the cluster or now nanoplasma expands, the Coulomb potential lowers again, and the thermalized electrons can escape the potential (see Section 2.4.1). The diffraction images carry, in principle, information about the total number of coherent scatterers and we can therefore estimate the number of electrons in the cluster over  $\Delta t$ . The single-shot diffraction pattern analysis from above also determines the intensity of the forward scattering (see Section 2.3.2), which is proportional to

$$I(\vec{Q} \rightarrow 0) \propto N_e^2, \quad (5.1)$$

where  $I$  is the distribution of the scattered intensity as a function of the scattering vector  $\vec{Q}$ , and  $N_e$  is approximately the number of electrons - as discussed in Section 2.3.2. We also assume that the coherent forward-scattering of the most intense LCLS hits is comparable on a shot-to-shot

basis [52]. Using Equation (2.41), Figure 5.9 shows the intensity  $I(\vec{Q} \rightarrow 0)$  as a function of the time delay,  $\Delta t$  (blue dots). Even considering the large error bars that originate from the standard deviation of the intensity distribution from the single-shot diffraction images, the data show a more rapid evaporation of electrons between (400 to 800) fs than between (0 to 400) fs. For the total time delay range of  $\Delta t = (0 \text{ to } 800)$  fs, the number of scattering electrons decreases on average by  $\sim 26\%$  (see Figure 5.9), while the Xe-clusters increase in radius by  $\sim 20\%$  (see Figure 5.8). In a simple electro-static model [91, 123], the potential of the plasma can be described by a homogeneously charged and expanding sphere. The kinetic energy of electrons that are trapped in this potential may be described using a Maxwell-Boltzmann distribution. In this case, the trapped electrons can escape the cluster potential depending on their kinetic energy and the potential depth. The hypothesis is that electrons are efficiently trapped at first, but the expansion of the cluster lowers the potential allowing the trapped electrons to escape. With the in this study measured cluster sizes and expansion speeds, this simplified model cannot reproduce the data points of Figure 5.9. Using the above stated expansion speed, electron temperature, and cluster-size, this simplified model indicates no loss of electrons in the given time window of 800 fs. In order for this model to fit the data,  $\sim 10$  times larger expansion speeds,  $v_{\text{exp}}$ , would have to be used (see red line in Figure 5.9). This could be a signature of anisotropic effects in the nanoplasm expansion [125, 202]. More data, particularly at longer time delays, would be needed to develop an accurate model.

The scattering and TOF data so far indicate that Coulomb trapped electrons may play a significant role in the nanoplasm. Trapped electrons damage the sample via secondary collisional ionization [29]. The key driver releasing trapped electrons is the nanoplasm expansion that lowers the Coulomb potential [122]. It should be noted that trapped electrons also contribute to the diffraction image. In a thought-experiment, where a single-particle imaging (SPI) experiment is performed using comparably long X-ray pulses of  $\sim 100$  fs, trapped electrons can be treated non-relativistic such that they contribute coherently to the diffraction image [203]. The delocalization of the trapped electrons and the widening of the cluster potential well reduce the contrast of diffraction images. This kind of radiation damage occurs on the timescale of Coulomb trapping and Figure 5.9 indicates that the Coulomb trapping is efficient upon the first time-resolved data points with delays comparable to the pulse length in this thought experiment. Therefore,  $\sim 100$  fs long pulses - as they are sometimes used at LCLS to perform SPI experiments - carry information of trapped electrons. This is a form of radiation damage and is described in Reference [27]. In this Reference, computational methods are presented and predicted to compensate for such damage.

## 5 Results and discussion

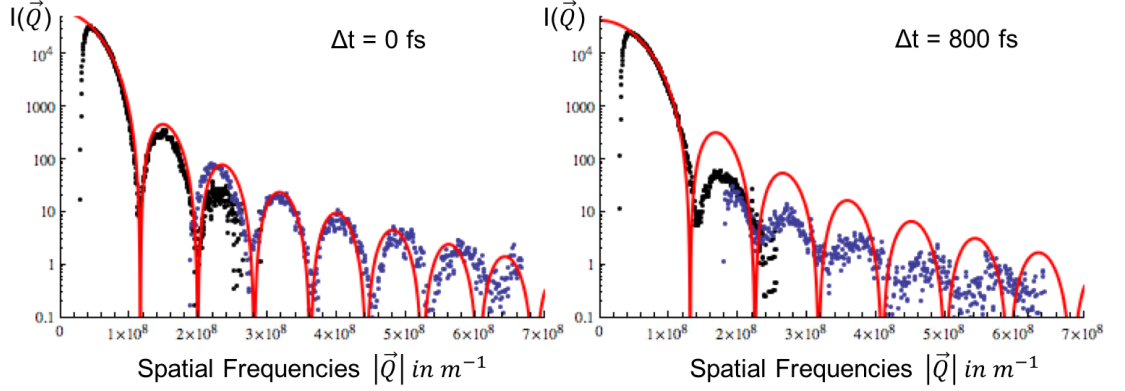


Figure 5.10: Single-shot diffraction patterns of single Xe-clusters at certain pump–probe delays  $\Delta t$ . The red curve simulates the scattering of a sphere, the black data points are from the rear pnCCD detector and the blue data points are from the front pnCCD. The nanoplasma expansion manifests in the scattering intensity  $I$  at high spatial-frequencies  $|\vec{Q}|$ , where  $I$  decreases as described in [21].

We may also analyze the Xe-clusters on a shot-to-shot basis. Similar to previous studies [20, 21, 55] radial projections of the measured diffraction patterns reveal structural information of the nanoplasma. In particular an optical pump–X-ray probe study on Xe-clusters [21] revealed that Xe-clusters exhibit a surface softening. Here, an electron density model similar to the one described in Section 4.5 was established and the model was fitted to the diffraction pattern. The surface expansion thereby manifested in the diffraction pattern as a decline of the scattering intensity distribution at higher spatial frequencies. The analysis from above already indicated this in the right panel Figure 5.8, where the average scattering intensity on the front pnCCD detector was measured as a function of  $\Delta t$ . To show similarities to this optical pump–X-ray probe study, radial projections of single-shot diffraction patterns from single Xe-clusters are shown in Figure 5.10. The figure shows a red line, which is the scattering from a sphere as per Equation (2.38) and (2.41) fitted onto the low- $|\vec{Q}|$  signal of the zeroth diffraction order using the radius and the incident beam intensity variables. The black data points are projected from the rear pnCCD and the blue data points are projected from the front pnCCD using the projection method described in Section 4.2.1. For  $\Delta t = 0$  fs, the scattering of the Xe-cluster can be well approximated with the scattering of a sphere. The “spherical fit” (red line) agrees well with the data points up to scattering angles of  $\Theta \approx 9^\circ$  or  $|\vec{Q}| \approx 6.8 \cdot 10^8 \text{ m}^{-1}$ . However, it should be noted that this comparison becomes less good at very large scattering angles due to deviations of the cluster from a perfect sphere. Above scattering angles of  $\sim 10^\circ$ , the flat detector surface should be accounted for [20], but it plays a negligible role in this thesis experiment. As the time delay  $\Delta t$

## 5.2 Scattering response of rare-gas clusters

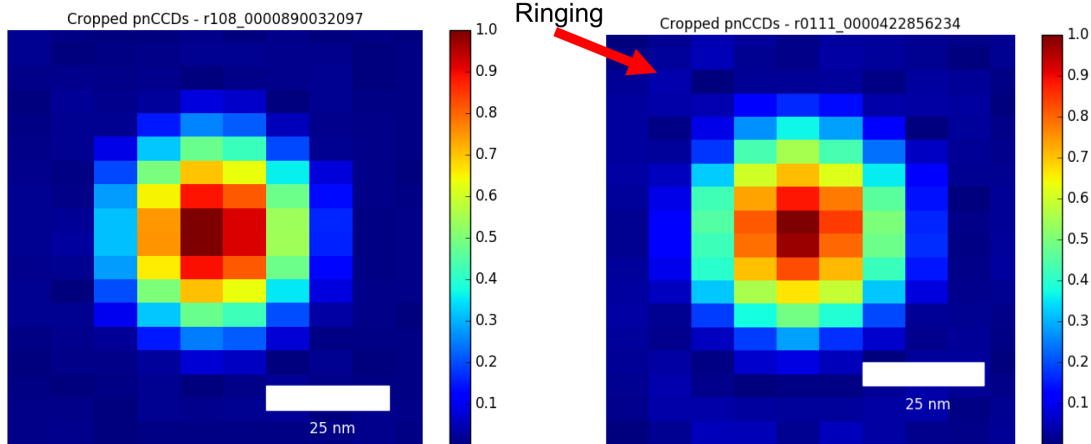


Figure 5.11: Single-shot 2D reconstructions of diffraction patterns from single Xe-clusters. The left image shows a  $\sim 25$  nm radius Xe-cluster at a pump–probe delay  $\Delta t = 0$  fs. The cluster has a spherical or arguably icosahedral electron density distribution that is distinct compared to the background. The right image shows a  $\sim 25$  nm radius Xe-cluster at a time delay  $\Delta t = 800$  fs that shows a similar shape. Possibly due to the loss of scatterers (see Figure 5.9) the signal-to-noise ratio decreases and a ringing appears that is likely generated by the support structure in the iterative process.

increases, the large- $|\vec{Q}|$  scattering signal decreases and the scattering of a plain sphere does not fit the scattering well anymore. The surface softening model from Section 4.5 generally fits the data well, which indicates that an X-ray induced nanoplasma is also undergoing a surface softening comparably to previous studies [21, 204]. Note that the X-ray pump–X-ray probe considerations from Section 4.4 would minimize the effect of a decreased scattering at large scattering angles.

To move beyond modeling diffraction patterns, reconstruction algorithms (see Section 4.3) are employed to directly investigate electron density profiles. Figure 5.11 shows 2D reconstructions of single Xe-clusters for the pump–probe delay  $\Delta t = 0$  fs (left) and  $\Delta t = 800$  fs (right). The clusters appear generally spherical. Both clusters have a radius of  $r \approx 25$  nm. It is noted that the reconstructions therefore constitute some of the smallest objects recovered with diffraction imaging at the time of writing. The minimal resolvable feature size in these images is  $\sim 14$  nm  $\times$   $\sim 6$  nm along the  $X \times Y$ -axis (see Section 4.3.2) and therefore, the real-space images are the highest-resolution reconstructions achieved at the time of writing. The reconstruction at  $\Delta t = 800$  fs shows a subtle ringing around the actual cluster, which is likely an artifact of the spherical support structure. This ringing becomes visible due to a lower signal-to-noise ratio, which could be due to the described loss of electrons in the interaction region and the therefore overall less scattered light. Due to the current instrumentation-based resolution limitations, a

## 5 Results and discussion

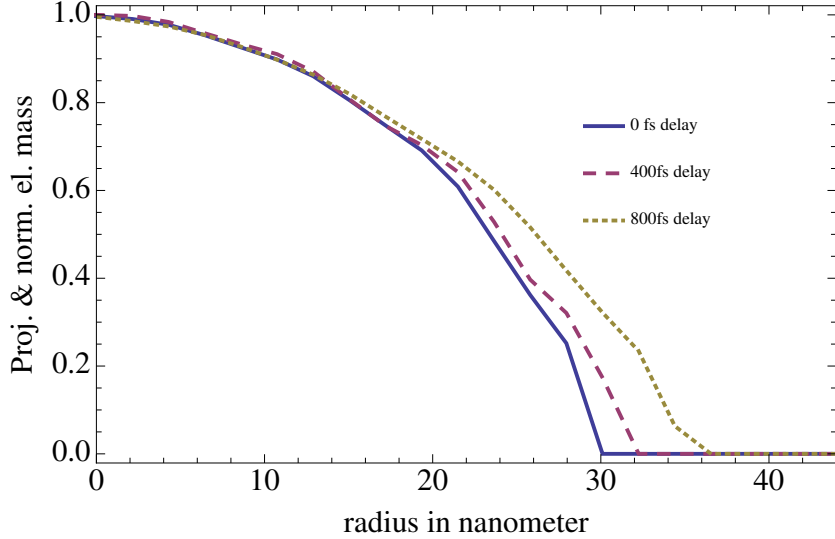


Figure 5.12: Single-shot 1D reconstruction of Xe-clusters at various time delays  $\Delta t$ . The figure shows the projected and normalized el. mass as a function of the radius, i.e., the electron density. These real-space images of a nanoplasma transition show that, at first, outer atomic layers are shed off, here imaged at  $\Delta t = 400$  fs. And over time, more inner atomic layers follow, here imaged at  $\Delta t = 800$  fs.

nanoplasma expansion, i.e., the earlier discussed 20 % increase in Xe-cluster radius, are difficult to reveal in a 2D reconstruction. Also, 2D reconstructions of nanoparticles that have a size of few ten nanometers are challenging and the number of successful 2D reconstructions is low. An alternative approach is to perform 1D reconstructions of the centro-symmetric diffraction images, which have a better signal-to-noise ratio.

1D real-space electron density reconstructions of single Xe-clusters are shown in Figure 5.12 (see Section 4.3.3). The 1D reconstructions show normalized and projected electron density from single xenon cluster at time delays  $\Delta t = (0, 400, \text{ and } 800)$  fs. At  $\Delta t = 0$  fs, the electron density follows the density projection of a sphere (compare Figure 4.8). With a delay of  $\Delta t = 400$  fs, an expansion of the outer atomic layers of the cluster is observed. At  $\Delta t = 800$  fs, outer layers continue to expand and inner atomic layers start to follow. Over the time delay sequence  $\Delta t = (0 \text{ to } 800)$  fs, the cluster radius expands  $\sim 20\%$ , or from  $r \approx (30 \text{ to } 36)$  nm. This sequence of events gives insight into the shape of the Xe-cluster as it undergoes the nanoplasma expansion and directly shows surface softening of the cluster. This expansion is similar to the modeled surface softening of Reference [21] and theoretically predictions, e.g., Reference [29].

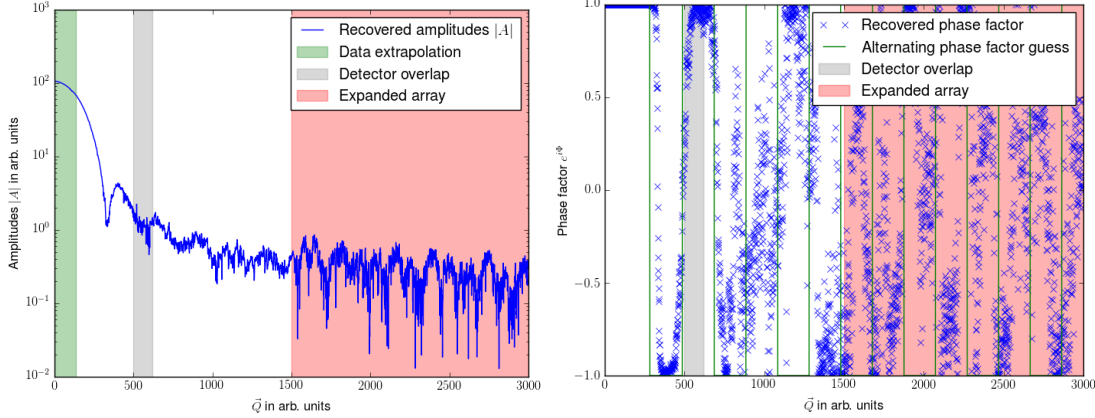


Figure 5.13: The left panel shows the recovered amplitudes  $|A|$  and the right panel shows the phase factor of the 1D phase retrieval. The green and red background indicates the space where initial data points were extrapolated. The gray area discloses the detector overlap. See Section 4.3.3 for more details.

For the sake of completeness of these 1D reconstructions, the recovered modulo of the amplitude,  $|A|$ , and the recovered phase factor are shown in Figure 5.13 for the data at  $\Delta t = 800$  fs. The amplitudes  $|A|$  have been replaced in the space with white background. The data with the green background are interpolated using the anticipated scattering of a sphere. The grayed area indicates the pnCCD detector overlap and the red background data are extrapolated from the scattering of a sphere. The red area therefore artificially increases the resolution. The data points of the k-times iterated Fourier-space function  $G'_k(\vec{Q})$  in the white area were replaced with the original data set while  $G_k(\vec{Q})$  was allowed to evolve freely in the remaining area. The phase factor retrieval starts with an initial guess of alternating signs per diffraction ring of the sphere and then evolves freely. One can see how the recovered phase factor is alternating as one would expect from the scattering of a sphere [115].

### 5.2.2 X-ray induced damage in pristine He-cluster

He-droplets have been subject to previous static investigations at the AMO instrument of the LCLS. After injection via a cryogenic cooled source (see Section 3.4) the superfluid He-cluster [79] form interesting quantum states [205, 206]. Particularly the analysis of their shape shows that droplets form as spheres but also as ellipses [153]. The ellipticity of a He-droplet relates to its rotational speed. It has been found that rotational speeds of superfluid He-droplets can go beyond the classical stability limits. They are stabilized by quantum vortices, which form inside the He-droplet [14]. For this thesis, only He-droplets that have a spherical form have been selected to avoid quantum vortices. It also enables us to use the symmetry in the diffraction

## 5 Results and discussion

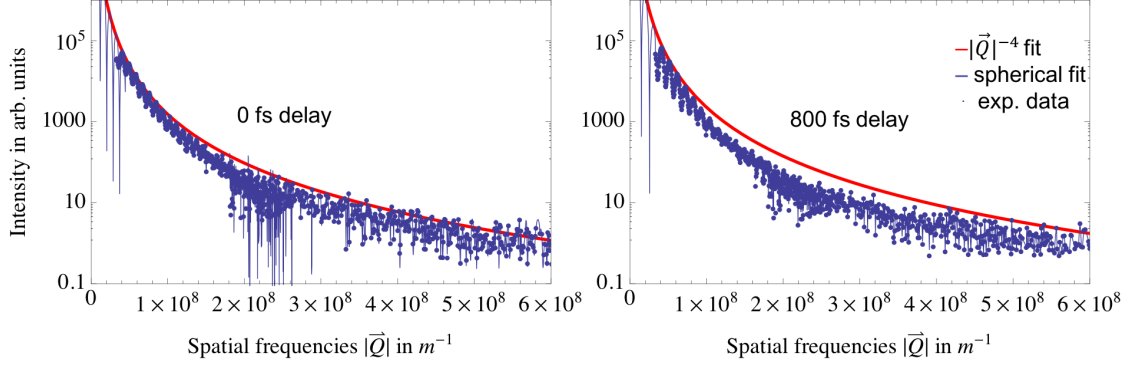


Figure 5.14: Single-shot diffraction images of pristine He-droplets at various  $\Delta t$  spherically projected into 1D.

patterns as above and perform a 1D analysis of the diffraction patterns. Single-shot diffraction images of He-droplets are shown in Figure 5.14. The He-droplets have a radii of  $r \approx (379$  and  $302)$  nm, at time delays  $\Delta t = (0$  and  $800)$  fs, respectively. For clarity, only the experimental data (blue points), spherical extrapolation at low  $|\vec{Q}|$ -values (blue line) and the envelope of the spherical extrapolation function (red line) are shown. For  $\Delta t = 0$  fs, the local maxima of the experimental data agree well with the envelope function up to very high  $|\vec{Q}|$  at the edge of the detector. This indicates an intact He-droplet, as shown in more detail in Section 5.2.1 for Xe-clusters. For a time delay of  $\Delta t = 800$  fs, the diffraction pattern of the droplet shows that the local maxima between  $|\vec{Q}| \approx (1$  to  $4) \cdot 10^8$  m $^{-1}$  are well below the envelope, this indicates X-ray induced sample damage and is similar to the surface softening discussed above. However, the surface softening of this droplet is less severe as in the Xe-clusters (compare Section 5.2.5). A phenomenological approach to explain the difference in sample damage is that the absorption cross-section of the helium atoms is much smaller than the one of xenon (see Section 2.3).

### 5.2.3 Condensation of xenon in helium cluster: Plum-pudding type cluster

When this thesis experiment was designed there was the hypothesis that Xe-atoms inside the He-droplets agglomerate to one compact structure with solid density. While it was known that for weak doping levels, the Xe-atoms condense to clusters with multiple centers [14, 207] it was hypothesized that higher Xe-doping levels favor the formation of a single Xe-cluster inside the He-droplet. This is called a xenon core–helium shell system. Figure 5.15 shows a typical diffraction pattern of a HeXe-cluster at 0.5 % Xe-doping level. The diffraction image immediately indicates a more complex structure of the Xe-particles within a spherical He-droplet than possible with a single Xe-core. A first step is therefore to investigate the morphology of Xe-clusters in He-droplets in more detail and create a model for the complex structure of HeXe-cluster. For

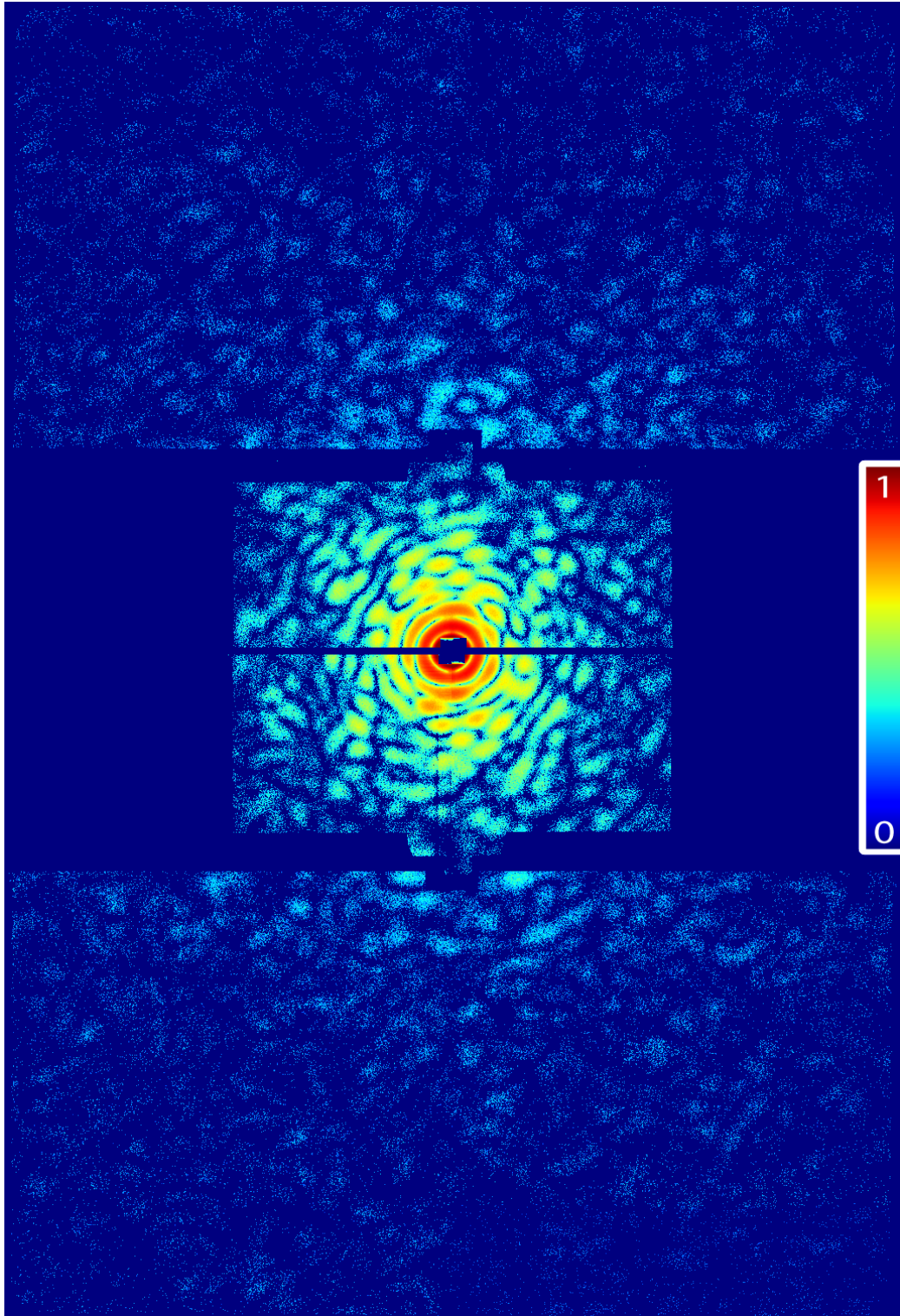


Figure 5.15: Diffraction image of a HeXe-cluster that has a radius of  $r \approx 210$  nm and a Xe-doping level of  $\sim 0.5\%$ . The image indicates a complex structure of Xe-particles within a spherical He-droplet. The corresponding real-space reconstruction is shown in Figure 5.16.

## 5 Results and discussion

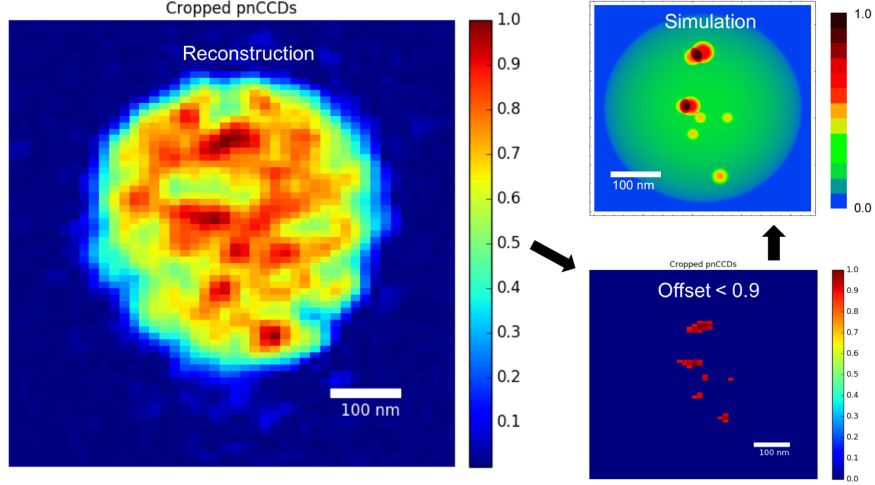


Figure 5.16: From a HeXe-cluster reconstruction to a simulated electron density. The real-space reconstruction of a HeXe-cluster has a radius of  $r \approx 210$  nm and a Xe-doping level of  $\sim 0.5\%$  (left). The normalized intensity map is offset (bottom right image) and mimicked by 2D electron density simulations (top right image). The electron density indicates a Xe-cluster arrangement inside the He-droplet of the plum-pudding few scatterers case as discussed in Figure 5.17.

this, we can state two competing hypotheses: one, xenon atoms condense to one large cluster within a helium droplet; and two, multiple smaller Xe-clusters form within a droplet. Let us call hypothesis two a *plum-pudding core–shell system*<sup>1</sup> that we can further divide into a case of few scatterers and many scatterers.

To investigate this hypothesis, real-space reconstructions from single-shot diffraction images of HeXe-clusters are analyzed first. The left panel of Figure 5.16 shows a reconstruction of a HeXe-cluster that has a radius of  $r \approx 210$  nm and a Xe-doping level of  $\sim 0.5\%$ . The reconstruction indicates a plum-pudding arrangement, where a few Xe-clusters (intense, dark red spots) are randomly distributed within the He-droplet (less intense, green to orange area). In the bottom right panel of Figure 5.16, the normalized intensity map from the reconstruction is offset to guide the eye to dense centers. These dense centers can be used to model an electron density in the 2D-simulations that are discussed in Section 4.5. The top right panel of Figure 5.16 shows the modeled electron densities. These simulated electron densities can be Fourier transformed into reciprocal space and ultimately be compared to the measured data.

---

<sup>1</sup>The name plum-pudding model comes from J.J. Thomson's model of the atom in 1904 and has here been reused to describe the arrangement of Xe-particles in He-droplets.

## 5.2 Scattering response of rare-gas clusters

To verify the success of the HeXe-reconstruction and to further test the above stated hypothesis, several core-shell simulations are discussed next. Figure 5.17 shows the discussed core–shell scenarios along with their Fourier-space representations in 1D. The simulated He-droplet has a radius of  $r_{\text{He}} \approx 125 \text{ nm}$  and a constant Xe-doping level of  $\sim 20\%$ . As comparison, the yellow, dashed line in the figure describes the scattered intensity distribution of this sphere and the red line is its envelope function. The figure depicts an artistic representation of the actual simulated electron densities from the core–shell systems on the left side. On the right side, the Fourier transformed data reveal that the agglomeration of the Xe-particles within the He-droplet dominates the scattering pattern (purple curve). This is due to the Xe-cluster density being  $\sim 25.8$  times larger than the density of liquid He-droplets and the resulting scattering factors that were discussed in Table 2.4. In the one-scatterer case with a single centered scattering center (see Figure 5.17a),  $N_{\text{sc}}$ , the purple curve consists of a large modulation in the diffraction image, which comes from the Xe-core and a small, more intense modulation that comes from the He-shell. The small modulation is similar to the yellow, dashed line and at low spatial-frequencies, where the He-droplet dominates the signal on the diffraction image. At large spatial-frequencies, the modulation from the Xe-cluster is more prominent. Ultimately, this is related to the size and density of each cluster, which is discussed in more detail below. In the few scatterers case with  $N_{\text{sc}} = 8$  scattering centers (see Figure 5.17b), the diffraction pattern (purple line) at low spatial-frequencies  $|\vec{Q}|$  is still dominated by the He-shell and at high spatial-frequencies  $|\vec{Q}|$  by the Xe-cores. However, the diffraction image appears to contain a more complex structure at large  $|\vec{Q}|$ -values due to the delocalized scatterers. Also, the average scattering intensity is well above the envelope of the scattering of a sphere (red line). The exact location of the few scattering centers has a small effect to the 1D projection of the 2D diffraction image, as long as the scattering centers are distributed throughout the He-droplet. In the many scatterers case with  $N_{\text{sc}} = 100$  (see Figure 5.17c), the scattering centers are randomly distributed within the He-droplet. The Xe-clusters are significantly reduced in size to match the constant xenon doping level of  $\sim 20\%$ . For the shape of the HeXe-cluster, the small clusters appear similar to a constant electron density increase, which is why the scattering is similar to the scattering of a sphere (yellow, dashed line) at low-to-mid  $|\vec{Q}|$ -values. Only at large spatial frequencies,  $|\vec{Q}|$ , which carry signal of high-resolution, the small Xe-particle structures are revealed and start to dominate the pattern.

The cases of the one scatterer and the many scatterers case show a rather simple structure in reciprocal space and are thus not able to reproduce a scattering image as the one shown in Figure 5.15. Only the few scatterers case results in a complex structure in reciprocal space. HeXe reconstructions and electron density simulations indicate that HeXe-clusters agglomerate to a plum-pudding core–shell system with a few scattering centers.

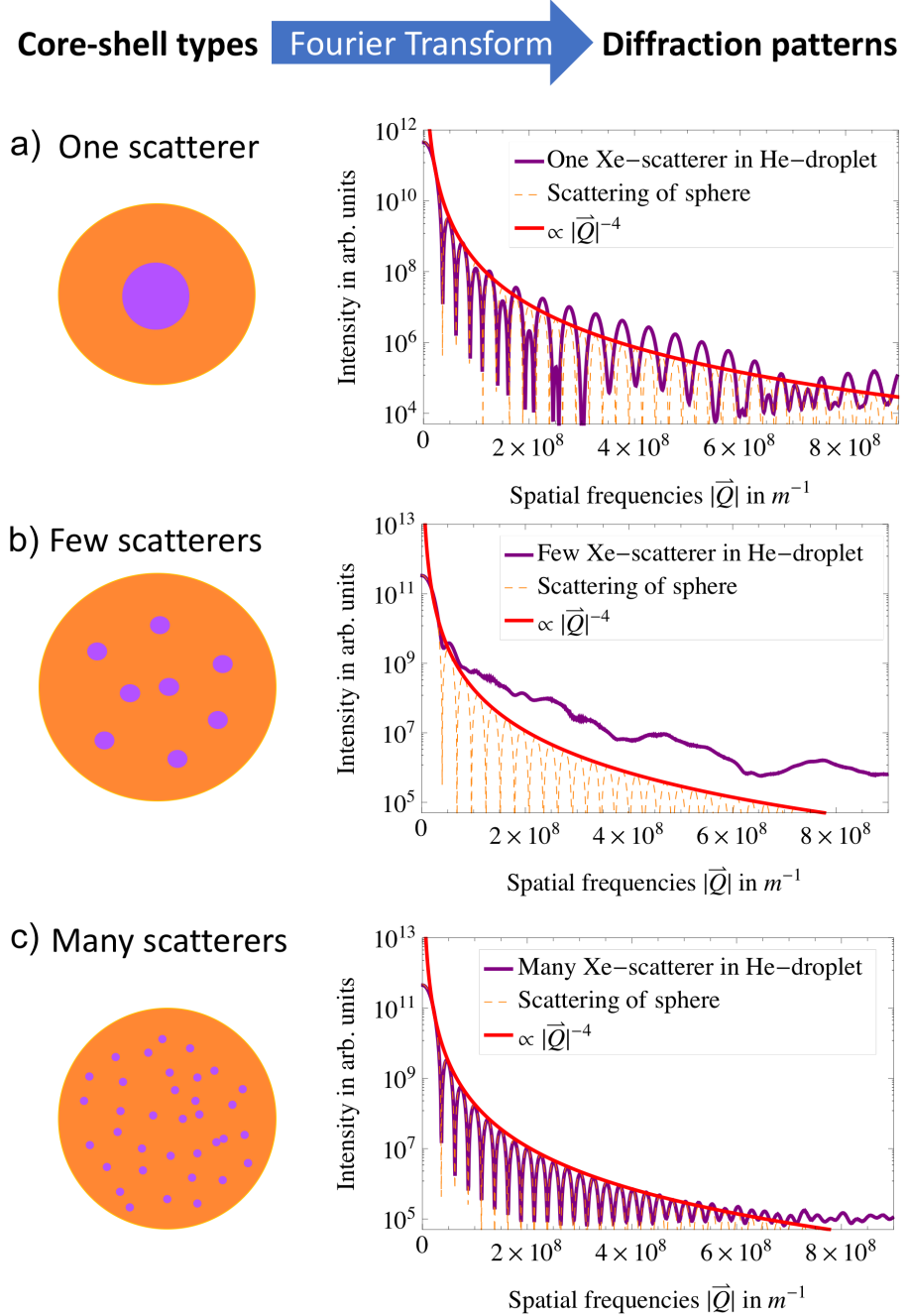


Figure 5.17: Hypothetical arrangements of Xe-clusters in superfluid He-droplets (left) and corresponding 1D diffraction patterns (right). The He-droplet has a radius of  $\sim 125$  nm and the Xe-doping level is  $\sim 20\%$ . The case of one xenon scattering center  $N_{sc} = 1$  (top), few scatterers  $N_{sc} = 8$  (middle), and many scatterers  $N_{sc} = 100$  (bottom) are shown. The scattering pattern is dominated by the signal from the He-droplet at low spatial frequencies, but at large  $|\vec{Q}|$ -values the signal is dominated by the Xe-clusters. This is mostly due to the size of the Xe-clusters; smaller scattering centers are resolved at larger scattering angles.

As we have seen above, the Xe-clusters dominate the diffraction pattern at least at large angles. Particularly the size of the Xe-clusters plays a major role at which spatial frequencies the Xe-clusters start to dominantly contribute. Let us quantify this finding with an estimation. For this, we can make use of Abbe's criterion (see Equation (4.6)) and the wave-vector definition (see Equation (2.32)). In vacuum, we can note the minimal resolvable feature size  $d$  as

$$d = \frac{2\pi}{|\vec{Q}_r|}, \quad (5.2)$$

with  $|\vec{Q}_r|$  being the spatial frequency relating to  $d$ . The feature size corresponds to the radius as  $d \approx 2r$ . This relation connects the radius of Xe-clusters to a certain point  $|\vec{Q}_r|$  in reciprocal space, where the Xe-clusters start to dominantly contribute to the diffraction image. The estimation via this relation works well for the one-scatterer case, where  $r_{\text{Xe}} \approx 15 \text{ nm}$ . However, as the structures become more complex with dense scattering centers throughout the cluster, the contributions to the spatial frequencies become more complex, for example, spatial frequencies originate not only from the size of the dense scattering centers but also their distances to the edges of the droplet and also the distances to other dense scattering centers. Thus, for the few scatterers case, the radii are estimated to be  $\sim 3$  times larger than in the actual simulation. This is similar in the many scatterers case. Here, the spatial frequency domain even more complex due to the many particles, their size variety and distances to surrounding objects such that the estimation overestimates the radii by a factor  $\sim 10$ . If ones desire is to determine the size of an embedded particle, which is a useful feature particularly to test the sample injection process, this can be done easily if just one particle is embedded in the center of the droplet. As multiple particles are embedded in a single He-droplet, this size estimation becomes less accurate.

#### 5.2.4 Understanding sample damage in the plum-pudding type clusters

This section investigates the surface softening in plum-pudding type HeXe-clusters. In a first step, 2D simulations are discussed in detail to go over possible sample damage scenarios. In a second step, the 2D simulations are compared to the measured data. Figure 5.18 shows a simulated diffraction pattern from the plum-pudding type electron density shown in Figure 5.16. The He-droplet has a radius  $r_{\text{He}} = 210 \text{ nm}$  and a strong Xe-doping of  $\sim 20\%$  to amplify the effects of the sample damage in the diffraction pattern. The figure shows several sample damage scenarios and the effects of this damage to the diffraction pattern. As described in Section 4.5, the modeled radiation damage is comparable to a surface softening. The blue, solid curve describes the scenario, where all spheres, i.e., clusters, are intact and no X-ray induced dynamics are

## 5 Results and discussion

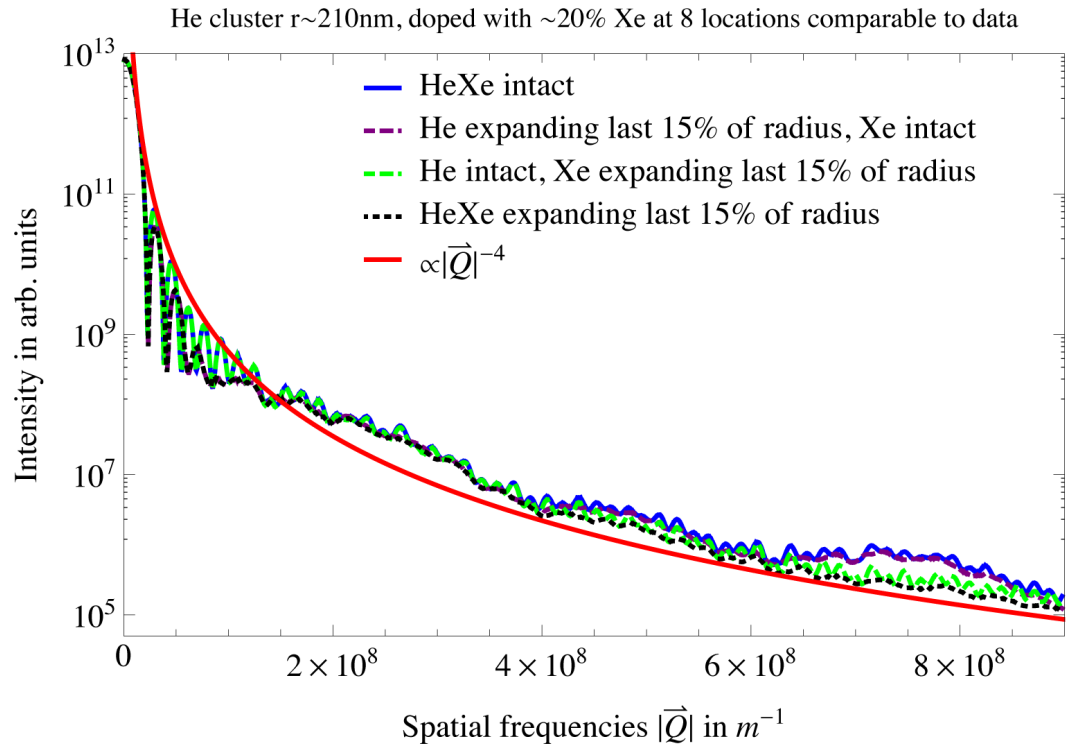


Figure 5.18: Simulated structural damage scenarios in simulated HeXe-clusters diffraction images. In reciprocal space: The blue curve shows the helium droplet as well as Xe-clusters intact. The purple, dashed curve shows an expanding He-droplet, leaving the Xe-clusters intact. The green, dashed curve leaves the He-droplet intact but shows expanding He-clusters. The black, dashed curve shows both cluster types expanding. The red curve is the envelope of the scattering of a sphere fitted to the zeroth order. The electron density arrangement from Figure 5.16 was used for these simulations and the electron density expansion introduced via Equation (4.11).

## 5.2 Scattering response of rare-gas clusters

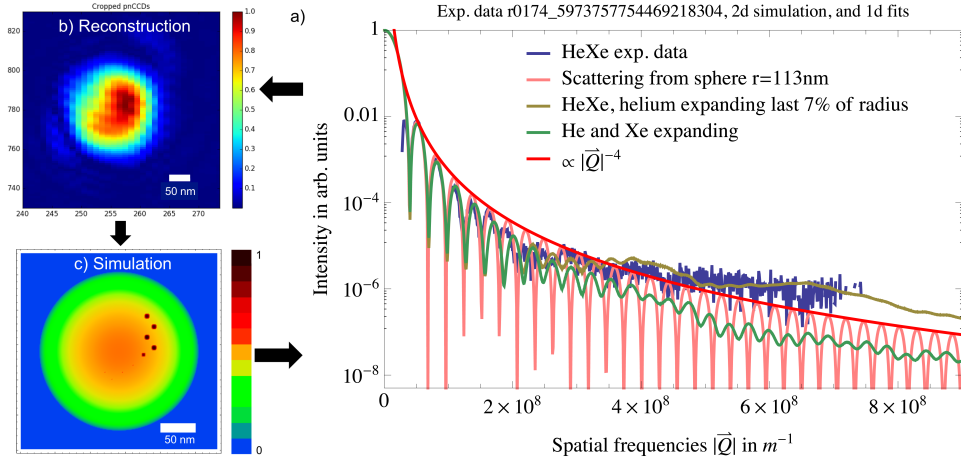


Figure 5.19: Matching experimental data of HeXe-clusters with  $r_{\text{He}} \approx 113$  nm at  $\Delta t = 800$  fs and simulations. a) The measured diffraction pattern has been projected to 1D (blue curve). b) From the same data, a 2D reconstruction of the HeXe-cluster is performed. c) The reconstruction is used to construct the simulated electron densities. These are then Fourier transformed and compared to the experimental data in a). Here, several simulated cases are shown and labeled in the legend of a). The simulation of an expanding He-droplet with an intact Xe-cluster fit the experimental data best (yellow curve).

present. The purple, dashed curve shows the case where the last 15 % in units of the He-droplet radius,  $r_{\text{He}}$ , expands but the Xe-cluster are intact. Conversely, the green, dashed curve shows the effect, where the last 15 % of the radius from Xe-clusters,  $r_{\text{Xe}}$ , expand but the He-shell stays intact. Lastly, the case, where all spheres are expanding in the last 15 % of their radii. It can be clearly seen that each scenario leaves a distinct fingerprint. In other words, the expansion of the large He-droplet affects low spatial frequencies and the expansion of small Xe-clusters affects high spatial-frequencies. The vast size difference of the Xe-clusters to the He-droplet, which are  $r_{\text{Xe}} = (25, 22, 20, 18, 17, 14, 14,$  and  $13.5)$  nm versus  $r_{\text{He}} = 210$  nm, allow a separation between the spatial frequency contributions in the diffraction pattern. This separation is related to the estimation made in Section 5.2.3. It is interesting to note how independently the He- and Xe-contributions affect their parts in the diffraction pattern. Let us use these insights to compare the 2D-simulations to the measured diffraction patterns. Figure 5.19 matches the experimental diffraction data and simulations: The blue curve in Figure 5.19a) is the measured diffraction data projected to 1D; Figure 5.19b) shows the corresponding HeXe-cluster reconstruction in 2D; Figure 5.19c) shows a 2D electron density model that has been constructed to match the 2D reconstruction; and again Figure 5.19a) shows the 1D diffraction patterns from the simulated electron densities. These experimental data have been taken at a time delay  $\Delta t = 800$  fs. The

## 5 Results and discussion

HeXe-cluster has a radius  $r_{He} \approx 113$  nm. The dense spots in the reconstruction have been simulated with 9 Xe-clusters of radii  $r_{Xe} = (4, 4, 4, 4, 3, 0.5, 0.5, 0.5, \text{ and } 0.5)$  nm. These radii of the simulated Xe-clusters have been determined iteratively such that a Xe-doping level of  $\sim 0.5\%$  was reached in the simulations – for clarity, the experimental Xe-doping level is also  $\sim 0.5\%$ . In the diffraction pattern, the scattering of a sphere with a radius  $r = 113$  nm (pink line) and its envelope (red line) are shown as a comparison. The yellow curve is a simulated diffraction pattern that shows an expanding He-droplet, where the last 7 % of the shell is exponentially expanding, while the Xe-clusters stay intact. The green curve shows the simulated diffraction pattern, where the He-droplet is expanding at the last 7 % of its radius and - to make the dependency clear - 90 % of the Xe-clusters outer radii are expanding. The simulations show a very good agreement with the expanding He-droplet at low spatial-frequencies  $|\vec{Q}|$ . At high frequencies, only the yellow curve that uses intact Xe-clusters in the simulation reproduces the measured diffraction pattern well.

The above HeXe-cluster simulations show that sample damage leaves a distinct feature in the diffraction pattern corresponding to either the expanding He-droplet or the expanding Xe-clusters. The measured diffraction pattern is fitted best using the electron density model of an expanding He-droplet and intact Xe-clusters. This indicates that helium acts as sacrificial layer slowing the nanoplasma expansion of the Xe-clusters, as xenon is the dominant photon absorber. Charge and kinetic energy transfer [30, 34] from the Xe-cluster to the He-droplet, as discussed in more detail in Section 5.1.2, could lead to a surface softening He-droplet but intact Xe-clusters. It should be noted, however, that sample damage in the Xe-clusters could be still possible but may not be detectable due to current resolution limitations.

### 5.2.5 Sacrificial layers: Comparison of sample damage in HeXe-cluster

Now that we have discussed the distinct features of sample damage in plum-pudding type HeXe-clusters in Section 5.2.4, we can analyze the scattering response of HeXe-cluster in another way. In a first step, this section compares the measured scattering response of HeXe-clusters at  $\Delta t = 0$  fs to the response at  $\Delta t = 800$  fs. And in a second step, the HeXe-clusters are compared to the time-resolved scattering response of pristine He- and Xe-clusters.

Starting with the HeXe-clusters, single-shot diffraction images of HeXe-cluster with radii  $r_{He} \approx (116 \text{ and } 113.5)$  nm, at time delays  $\Delta t = (0 \text{ and } 800)$  fs, respectively, are shown in Figure 5.20. The experimental data for  $\Delta t = 800$  fs is the same as in Figure 5.19. The black dots are data points from the rear pnCCD and the blue dots are data points from the front pnCCD. The pink, dashed curve is the scattering from a sphere fitted to the first order of diffraction and the red curve

## 5.2 Scattering response of rare-gas clusters

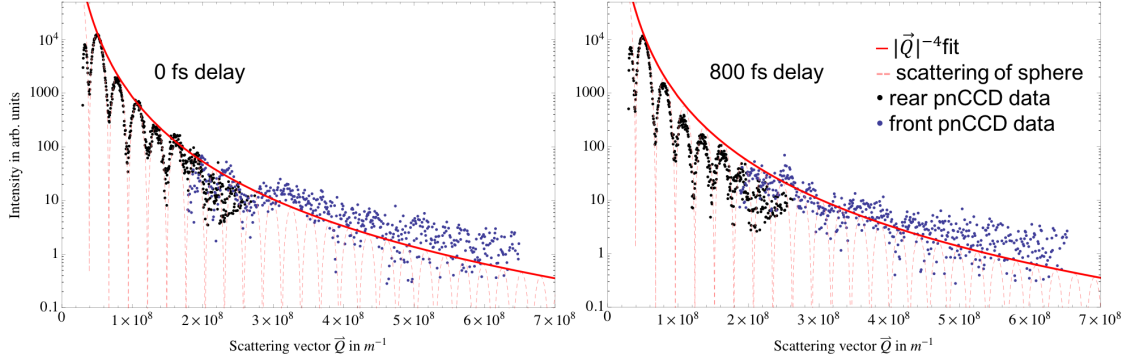


Figure 5.20: Single-shot diffraction pattern of HeXe-cluster at time delays  $\Delta t = (0 \text{ and } 800) \text{ fs}$ .

At  $\Delta t = 0 \text{ fs}$ , the diffraction pattern follows the scattering pattern of a sphere at low spatial-frequencies but stays well above the envelope function  $|\vec{Q}|^{-4}$  at high spatial-frequencies. At  $\Delta t = 800 \text{ fs}$ , the scattering curve deviates from the scattering pattern of a sphere at low spatial-frequencies indicating X-ray induced damage to the He-shell structure. At high spatial frequencies, the signal changes little compared to the  $\Delta t = 0 \text{ fs}$  data, which indicates that the Xe is undamaged.

is its envelope. For  $\Delta t = 0 \text{ fs}$ , the rear pnCCD data points agree well with the scattering of intact He-droplets (compare to pink, dashed line). The data points from the front detector lay well above the scattering envelope function of the sphere, which corresponds to the scattering of intact Xe-clusters (compare Section 5.2.4). For  $\Delta t = 800 \text{ fs}$  - as already discussed in Section 5.2.4 - the low spatial frequency intensity contributions agree well with the scattering of a damaged He-droplet, while the high spatial frequencies intensities can be best fitted with intact Xe-clusters. The single-shot events at  $\Delta t = (0 \text{ and } 800) \text{ fs}$  allow us now to identify their differences and the main difference is that the He-droplet's low spatial frequency contributions in the intensity distribution are reduced. The high spatial frequency contributions to the intensity distribution that originate dominantly from the Xe-clusters are affected little, as we will see in more detail below.

Let us quantify the intensity contributions at high spatial frequencies now in more detail to analyze potential sample damage of the embedded Xe-clusters. Previous studies have used a so-called R-factor (e.g., Reference [18, 136]) that successfully quantified effects of radiation damage in computer simulations. In the following, a comparison of the measured scattering versus the expected scattering is made and the results of this comparison are summarized in Table 5.1. To start with, let us analyze pristine He- and Xe-clusters first. The diffraction patterns of pristine He- or Xe-clusters can be easily compared to the scattering curve of a sphere. The scattering of a curve of a sphere is here denoted as the function  $i(\vec{Q})$ . We can also introduce

## 5 Results and discussion

**Measured scattering / expected scattering**

For sample	At time delay $\Delta t$	
	0 fs	800 fs
Xe-cluster	0.91	0.26
He-droplet	0.89	0.65
HeXe-cluster	1	1.33

Table 5.1: Relative comparison of measured scattering versus expected scattering for Xe-, He- and HeXe-cluster at large spatial frequencies.

a function  $h(\vec{Q})$  that interpolates between the data points of pristine He- and Xe-cluster. The relative difference of these functions at a certain time delay can be noted as  $\frac{\sum h(\vec{Q})}{\sum i(\vec{Q})}|_{\Delta t}^{\text{sample}}$ , with the sums over  $|\vec{Q}|$  running between  $(2.8 \text{ to } 6.4) \cdot 10^8 \text{ m}^{-1}$ . For Xe- and He-clusters at  $\Delta t = 0 \text{ fs}$ , we find values close to the expected scattering. The measured scattering divided by the expected scattering is  $91\%|_{\Delta t=0\text{fs}}^{\text{Xe}}$  and  $89\%|_{\Delta t=0\text{fs}}^{\text{He}}$ . The interpolating function underestimates the actual scattering by  $\sim 10\%$ , which gives us an idea of the uncertainty of this estimate. For the delay  $\Delta t = 800 \text{ fs}$ , the actual scattering is reduced due to the surface softening such that  $26\%|_{\Delta t=800\text{fs}}^{\text{Xe}}$  and  $65\%|_{\Delta t=800\text{fs}}^{\text{Xe}}$  (compare to Section 5.2.1 and 5.2.2). HeXe-clusters cannot directly be compared to the scattering of a sphere. However, we may compare similar single-shot events at different time delays to each other. The two single-shot events for  $\Delta t = (0 \text{ and } 800) \text{ fs}$  that are shown in Figure 5.20 represent similar single events, as they have the same incident beam intensity,  $I_0$ , in the  $I_0|\vec{Q}|^{-4}$  fit, a size difference of only  $\sim 2\%$ , and are produced at the same source and doping conditions. When comparing the interpolating functions  $h(\vec{Q})|_{\Delta t=800\text{fs}}^{\text{HeXe}}/h(\vec{Q})|_{\Delta t=0\text{fs}}^{\text{HeXe}}$  at different time delays  $\Delta t$ , 33 % more scattering at large  $|\vec{Q}|$ -values is measured. While the uncertainty in this shot-to-shot comparison is drastically higher, this estimate supports the finding that intensities at large spatial-frequencies are not reduced.

Summarizing, we find a reduction in scattering intensity at the spatial-frequencies  $|\vec{Q}| = (2.8 \text{ to } 6.4) \cdot 10^8 \text{ m}^{-1}$  of  $\sim 65\%$  in Xe-clusters and  $\sim 24\%$  in He-droplets 800 fs after the LCLS pump-pulse. These changes can be attributed to X-ray induced sample damage. If Xe-clusters are embedded in a He-droplet, no scattering reduction can be measured 800 fs after the pump-pulse. This indicates that embedded or tampered Xe-clusters exhibit no measurable sample damage at the current resolution. However, the He-droplet shows X-ray induced damage in the diffraction image. This indicates that in HeXe-clusters the He-droplet acts as sacrificial layer slowing indications of Xe-cluster sample damage in diffraction images. As discussed in previous sections in more detail, charge and kinetic energy transfer [30, 34] are likely responsible for the sample integrity of the dominantly absorbing Xe-clusters.

## 6 Summary and outlook

This work experimentally investigates the ionization and expansion dynamics of nanometer-sized samples in intense X-ray pulses using a novel X-ray pump–X-ray probe technique. During intense X-ray pulses from free-electron lasers (FELs) all nanometer-sized samples are transformed into a nanoplasma. The nanoplasma transformation consists of a rapid ionization and expansion of the illuminated sample, which is often referred to as sample damage [18, 122]. Sample damage is particular undesired in X-ray diffractive imaging, where typically the shape of a bio-molecule is determined. But, sample damage changes the shape of the imaged nanoparticles leading to false measurements. To avoid this, diffractive imaging uses the principle diffraction before destruction. The idea here is that a few femtosecond-long XFEL-pulse images a nanoparticle before it is destroyed. When nanoparticles are imaged with few femtosecond long X-ray pulses, enormous X-ray fluences of ( $10^{13}$  to  $10^{15}$ ) photons  $\mu\text{m}^{-2}$  are needed [24]. Currently existing and planned light sources will not reach these parameters. To reduce these light source requirements, sacrificial layers around the sample have been suggested to slow the sample damage process [30, 33] allowing longer XFEL pulse durations. To investigate the function of sacrificial layers, we compare pristine xenon clusters with xenon clusters that are embedded in a helium droplet. The He-droplet then acts as a sacrificial layer. This work provides strong evidence that the xenon clusters inside helium droplets show slowed X-ray induced damage processes.

For the experimental part of this thesis, the new soft X-ray imaging end-station LAMP was partly designed, built, and commissioned [10]. Using this new experimental setup, a coincident single particle imaging and time-of-flight mass spectroscopy method is employed [52]. Data from multiple imaging detectors are merged, which virtually increases the detector area and virtually extends the dynamic range of the detector system. This allows the measurement of diffraction images from nanoparticles with thus far unprecedented resolution. The superfluid He-droplets and solid Xe-clusters nanoparticles are formed through a supersonic gas expansion into the vacuum. The heterogeneous HeXe-clusters are generated through the pickup concept. To study the nanoplasma transformation of these samples, a novel, accelerator-based X-ray pump–X-ray probe technique is employed at the Linear Coherent Light Source [38]. This technique produces two time-delayed pulses. First, a pump-pulse on the order of  $\sim 2 \cdot 10^{16} \text{ W cm}^{-2}$  ignites

## 6 Summary and outlook

the nanoplasma; and second, a factor 10 stronger probe-pulse that images the nanoplasma transformation. The delayed pump–probe pulses enable a time-resolved study of the nanoplasma transformation in the thus far unreached range of (0 to 800) fs.

The experimental data shows that pristine Xe- and He-clusters exhibit a surface-softening in which first the outer atomic layers of the nanoparticle are “exploding” off the sample and inner-layers follow. Xe-clusters undergo a radial expansion that shows in diffraction images within the first delay step at  $\Delta t = 120$  fs. Over the course of 800 fs, the radial expansion manifests in a  $\sim 20\%$  increase of their initial average radius, which is  $r \approx 61$  nm. The Xe-nanoplasma is heated to electron temperatures of  $\sim 125$  eV. He-droplets exhibit similar but less violent sample damage. Heterogeneous HeXe-clusters likely agglomerate in a plum-pudding configuration. In this plum-pudding HeXe-cluster structure, multiple Xe-clusters condense within a larger He-droplet at different locations. When these mixed HeXe-clusters are pumped with intense X-rays from LCLS, Xe-clusters are dominantly absorbing the radiation. But, data show that Xe-clusters are barely ionized. The weak absorbing helium experiences stark ionization and the He-droplet shows signs of a surface-softening (see Figure 5.20). This indicates that the He-droplet functions as a sacrificial shell around the Xe-particles, which slows their surface-softening. However, X-ray induced damage that becomes detectable at higher resolutions may still be possible.

The results of this work are beneficial to a variety of fields. First, the works from References [21, 34] are expanded and this thesis includes reconstructions of nanoparticles and uses a time-resolved X-ray pump–X-ray probe technique to investigate the nanoplasma formation. Second, it was found through diffractive imaging that HeXe-cluster agglomerate in a plum-pudding structure. This potentially unique plum-pudding nano-structure of HeXe-clusters is an interesting and entirely extension of the typically considered core–shell model [29–34]. Third, the time-resolved data of HeXe-clusters indicates that the nanoplasma expansion of Xe-clusters is slowed within the He-droplet. Therefore, helium could be used as sacrificial layer material to slow the sample damage progression, although it is a low-Z material. This may be interesting for the single-particle imaging community, where it is foreseen that radiation damage will be a limiting factor for the ultimately achievable resolution [25]. Additionally, the imaging community will be able to take advantage of the improved LAMP detector geometry detecting larger scattering angles asynchronously and merged detector images described in this thesis. This method increases the previously obtained resolution in single-shot diffractive imaging by a factor  $\sim 5$  and virtually increases the dynamic range. The method will unfold its full potential when asymmetric diffraction images are combined with an expand-maximize-compress algorithm [194]. In principle, the algorithm allows an orientation and averaging of the asymmetric

diffraction images enabling sub nanometer-resolution 3D reconstructions. Finally, the X-ray pump–X-ray probe approach pioneered during this thesis experiment has already been extended to various other experiments, such as References [22, 50, 63, 150, 208], allowing entirely new insights previously unreachable.



# Appendix

## 1 Python code on combining detectors

Python code that has been used to combine pnCCD detectors.

```
# Imported Packages
import numpy as np

### Gaps between front top and bottom pnCCD to middle of rear pnCCD
gapTop =231                      # In pixel
gapBot =252                      # In pixel

### offset between rear and front pnCCDs
xShift =-1                         # In pixel

##### Things to adjust per run/experiment
pixelSizePnccd=75*10**-6          # Size of a pixel in meter.

distanceOfRearPnccd=0.74           # Distance IR to front pnCCD in meter
distanceOfFrontPnccd=0.36          # Distance IR to front pnCCD in meter
gainRearPnccd=1./64.               # Detector gain multiplier
gainFrontPnccd=1.                  # Detector gain multiplier

scatteredWaveLength=1.5*10**-9    # Wavelength of photons in meter

pathToHDF5=                        # Adapt to your needs

### Functions
# Phi - scattering angle
def PhiScatt(pixel, pixelSize, distanceToDetector):
    return np.arctan(pixel*pixelSize/distanceToDetector)

# Q-vector function
def qVector(pixel, pixelSize, distanceToDetector, waveLength):
    return 4.*np.pi*np.sin(PhiScatt(pixel, pixelSize,
                                     distanceToDetector)/2)/waveLength
```

## Appendix

```

#### Reading intensity files ,
intFrontTop= # Adapt to your needs
intRear= # Adapt to your needs
intFrontBottom= # Adapt to your needs

#### Intensity normalization and offset of electronic noise .
# Rear int. normalization
intRear=intRear*(1/gainRearPnccd)*(distanceOfRearPnccd**2)*
(1/distanceOfFrontPnccd**2)

# Offset
intRear[intRear < 15*(1/gainRearPnccd)*(distanceOfRearPnccd**2)*
(1/distanceOfFrontPnccd**2)]=0.0
intFrontTop[intFrontTop < 350]=0.0
intFrontBottom[intFrontBottom < 350]=0.0

#### Combining front detector
ztop=np.concatenate((intFrontTop,np.zeros
((gapTop+gapBot,1028)),intFrontBottom))

#### Combining rear with front detector
# Creating pixel to Q-vector correlation vectors
yRear, xRear =np.ogrid[(-len(intRear))/2:(len(intRear))/2 ,
-(len(intRear[0]))/2:(len(intRear[0]))/2]

# To transform Q-values from rear pnCCD to front pnCCD pixel values
qDiv=qVector(1, pixelSize=pixelSizePnccd ,
distanceToDetector=distanceOfFrontPnccd ,
waveLength=scatteredWaveLength)

# Spanning Q-space
y_comb=len(ztop)/2
x_comb=len(ztop[0])/2

qyRear=np.round(qVector(yRear, pixelSize=pixelSizePnccd ,
distanceToDetector=distanceOfRearPnccd ,
waveLength=scatteredWaveLength)/qDiv).astype(int) + y_comb
qxRear=np.round(qVector(xRear, pixelSize=pixelSizePnccd ,
distanceToDetector=distanceOfRearPnccd ,
waveLength=scatteredWaveLength)/qDiv).astype(int) + x_comb + xShift

# Keep track of per pixel additions to create mean intensities

```

```

norm=np.zeros(ztop.shape)

# Iterating over the array, slow but works
it=np.nditer(intRear, flags=['multi_index'])

while not it.finished:
    # read pixel transform coordinates
    y_idx = qyRear[it.multi_index[0],0]
    x_idx = qxRear[0,it.multi_index[1]]

    # add intensities and add to norm
    ztop[y_idx,x_idx] += it[0]
    norm[y_idx,x_idx] += 1

    it.itternext()

# Corrections to norm so not 1/0, seems inefficient but is fast enough.
norm -= 1
norm[norm<0]=0
norm += 1

### Combined mean intensities of front and rear detector.
ztop = ztop/norm

```

## 2 Matlab code on spherical integrations

Excerpt of the Matlab code that has been used to reduce 2D diffraction images to 1D arrays with the intensity as a function of the scattering vector  $\vec{Q}$ .

```

%&% CENTER OF HIT
x_center=xLen/2; % Actually Y-center
y_center=yLen/2; % Actually X-center
for r=(1:1500)
    %looping over points
    for y=(1:yLen)
        for x=(1:xLen)
            %check if in circle
            if (x - x_center)^2 + (y - y_center)^2 < r^2
                %norm
                rnorm(r)=rnorm(r)+1;
                % testing for noise/photons
                if rearpnccd(x,y)>0
                    circleSum(r)=circleSum(r)+rearpnccd(x,y);

```

## Appendix

```

        end
    elseif (x - x_center)^2 + (y - y_center)^2 == r^2
        %norm
        rnorm(r)=rnorm(r)+(1/2);
        % testing for noise/photons
        if rearpnccd(x,y)>0
            circleSum(r)=circleSum(r)+(rearpnccd(x,y)/2);
        end
    end
end
if rnorm(r)==0
    rnorm(r)=1;
end
if r==1
    plotSum(r)=circleSum(r)/rnorm(r);
elseif rnorm(r)-rnorm(r-1)>0
    plotSum(r)=(circleSum(r)-circleSum(r-1))/(rnorm(r)-rnorm(r-1));
else
    plotSum(r)=0;
end
end

```

## 3 Python code on 1D phase-retrieval

An excerpt of the python code that has been used to iteratively retrieve the complex fields of the diffraction pattern.

```

for i in range(1,160):
    print i # Keeps track of iterations
    # Fourier Transform to Fourier Space
    fourierSpace = np.fft.fft(realSpaceAdjusted)

    # Get Phase in Fourier Space
    phase = np.exp(np.angle(fourierSpace)*I)

    # Take absolute measurement and multiply with phase
    fourierSpaceAdjusted =
        abs(np.concatenate((target[0:len(phasedAmplitudes)],
                           fourierSpace[len(phasedAmplitudes):len(phasedAmplitudes)*3],
                           target[len(phasedAmplitudes)*3:len(target)]), axis=0))*phase

    # Calculate Error in Fourier Space

```

```
errorDiffraction = np.append(errorDiffraction ,
    np.std(np.abs(fourierSpace[0:len(phasedAmplitudes)]) -
        np.abs(target[0:len(phasedAmplitudes)])))

###  
# Fourier Transform to Real Space  
realSpace = np.fft.ifft(fourierSpaceAdjusted)  
realSpaceAdjusted = realSpace.real

# Set values to zero where object not expected  
realSpaceAdjusted[realSpaceAdjusted < 0] = 0

# Claculate error of Support  
errorSupport = np.append(errorSupport ,
    np.sum(np.abs(np.fft.ifftshift(realSpace)[0:len(realSpace)/2 -
        - 30])))
```



# Bibliography

- [1] W. C. Röntgen, *The Nobel Prize in Physics*, The Nobel Foundation, “In recognition of the extraordinary services he has rendered by the discovery of the remarkable rays subsequently named after him”, 1901.
- [2] K. M. G. Siegbahn, *The Nobel Prize in Physics*, The Nobel Foundation, “For his discoveries and research in the field of X-ray spectroscopy”, 1924.
- [3] M. von Laue, *The Nobel Prize in Physics*, The Nobel Foundation, “For his discovery of the diffraction of X-rays by crystals”, 1914.
- [4] S. W. H. Bragg and W. L. Bragg, *The Nobel Prize in Physics*, The Nobel Foundation, “For their services in the analysis of crystal structure by means of X-rays”, 1915.
- [5] M. Karplus, M. Levitt, and A. Warshel, *The Nobel Prize in Chemistry*, The Nobel Foundation, “For the development of multiscale models for complex chemical systems”, 2013.
- [6] R. J. Lefkowitz and B. K. Kobilka, *The Nobel Prize in Chemistry*, The Nobel Foundation, “For studies of G-protein-coupled receptors”, 2012.
- [7] W. Ackermann, G. Asova, V. Ayvazyan, A. Azima, N. Baboi, J. Bähr, V. Balandin, B. Beutner, A. Brandt, A. Bolzmann, et al., “Operation of a free-electron laser from the extreme ultraviolet to the water window,” *Nature Photonics* **1**, 336 (2007).
- [8] H. N. Chapman, P. Fromme, A. Barty, T. A. White, R. A. Kirian, A. Aquila, M. S. Hunter, J. Schulz, D. P. DePonte, U. Weierstall, et al., “Femtosecond x-ray protein nanocrystallography,” *Nature* **470**, 73 (2011).
- [9] P. Emma, R. Akre, J. Arthur, R. Bionta, C. Bostedt, J. Bozek, A. Brachmann, P. Bucksbaum, R. Coffee, F.-J. Decker, et al., “First lasing and operation of an ångstrom-wavelength free-electron laser,” *Nature Photonics* **4**, 641 (2010).
- [10] K. R. Ferguson, M. Bucher, J. D. Bozek, S. Carron, J.-C. Castagna, R. Coffee, G. I. Curiel, M. Holmes, J. Krzywinski, M. Messerschmidt, et al., “The Atomic, Molecular and Optical Science instrument at the Linac Coherent Light Source,” *Journal of Synchrotron Radiation* **22**, 492 (2015).

## Bibliography

- [11] C. Bostedt, S. Boutet, D. M. Fritz, Z. Huang, H. J. Lee, H. T. Lemke, A. Robert, W. F. Schlotter, J. J. Turner, and G. J. Williams, “Linac coherent light source: the first five years,” *Reviews of Modern Physics* **88**, 015007 (2016).
- [12] H. N. Chapman, A. Barty, M. J. Bogan, S. Boutet, M. Frank, S. P. Hau-Riege, S. Marchesini, B. W. Woods, S. Bajt, W. H. Benner, et al., “Femtosecond diffractive imaging with a soft-X-ray free-electron laser,” *Nature Physics* **2**, 839 (2006).
- [13] M. M. Seibert, T. Ekeberg, F. R. Maia, M. Svenda, J. Andreasson, O. Jonsson, D. Odic, B. Iwan, A. Rocker, D. Westphal, et al., “Single mimivirus particles intercepted and imaged with an x-ray laser,” *Nature* **470**, 78 (2011).
- [14] L. F. Gomez, K. R. Ferguson, J. P. Cryan, C. Bacellar, R. M. P. Tanyag, C. Jones, S. Schorb, D. Anielski, A. Belkacem, C. Bernando, et al., “Shapes and vorticities of superfluid helium nanodroplets,” *Science* **345**, 906 (2014).
- [15] T. Ekeberg, M. Svenda, C. Abergel, F. R. Maia, V. Seltzer, J.-M. Claverie, M. Hantke, O. Jonsson, C. Nettelblad, G. van der Schot, et al., “Three-Dimensional Reconstruction of the Giant Mimivirus Particle with an X-Ray Free-Electron Laser,” *Physical Review Letters* **114**, 098102 (2015).
- [16] I. Barke, H. Hartmann, D. Rupp, L. Flückiger, M. Sauppe, M. Adolph, S. Schorb, C. Bostedt, R. Treusch, C. Peltz, et al., “The 3D-architecture of individual free silver nanoparticles captured by X-ray scattering..,” *Nature Communications* **6**, 6187 (2015).
- [17] D. Rupp, “Ionization and plasma dynamics of single large xenon clusters in superintense xuv pulses,”  Thesis (Technische Universität Berlin, 2013).
- [18] R. Neutze, R. Wouts, D. van der Spoel, E. Weckert, and J. Hajdu, “Potential for biomolecular imaging with femtosecond x-ray pulses,” *Nature* **406**, 752 (2000).
- [19] L. Young, E. P. Kanter, B. Krassig, Y. Li, A. M. March, S. T. Pratt, R. Santra, S. H. Southworth, N. Rohringer, L. F. Dimauro, et al., “Femtosecond electronic response of atoms to ultra-intense X-rays,” *Nature* **466**, 56 (2010).
- [20] C. Bostedt, E. Eremina, D. Rupp, M. Adolph, H. Thomas, M. Hoener, A. R. B. de Castro, J. Tiggesbaumker, K. H. Meiwes-Broer, T. Laarmann, et al., “Ultrafast x-ray scattering of xenon nanoparticles: imaging transient states of matter,” *Physical Review Letters* **108**, 093401 (2012).
- [21] T. Gorkhover, S. Schorb, R. Coffee, M. Adolph, L. Foucar, D. Rupp, A. Aquila, J. D. Bozek, S. W. Epp, B. Erk, et al., “Femtosecond and nanometre visualization of structural dynamics in superheated nanoparticles,” *Nature Photonics* **10**, 93 (2016).

- [22] K. R. Ferguson, M. Bucher, T. Gorkhover, S. Boutet, H. Fukuzawa, J. E. Koglin, Y. Ku-magai, A. Lutman, A. Marinelli, M. Messerschmidt, et al., “Transient lattice contraction in the solid-to-plasma transition,” *Science Advances* **2**, e1500837 (2016).
- [23] G. Huldt, A. Szőke, and J. Hajdu, “Diffraction imaging of single particles and biomolecules,” *Journal of Structural Biology* **144**, 219 (2003).
- [24] S. P. Hau-Riege, R. A. London, G. Huldt, and H. N. Chapman, “Pulse requirements for x-ray diffraction imaging of single biological molecules,” *Physical Review E* **71**, 061919 (2005).
- [25] A. Aquila, A. Barty, C. Bostedt, S. Boutet, G. Carini, D. dePonte, P. Drell, S. Doniach, K. H. Downing, T. Earnest, et al., “The linac coherent light source single particle imaging road map,” *Structural Dynamics* **2**, 041701, 041701 (2015).
- [26] P. J. Ho, C. Knight, M. Tegze, G. Faigel, C. Bostedt, and L. Young, “Atomistic three-dimensional coherent x-ray imaging of nonbiological systems,” *Physical Review A* **94**, 063823 (2016).
- [27] H. M. Quiney and K. A. Nugent, “Biomolecular imaging and electronic damage using X-ray free-electron lasers,” *Nature Physics* **6**, 16 (2010).
- [28] C. H. Yoon, M. V. Yurkov, E. A. Schneidmiller, L. Samoylova, A. Buzmakov, Z. Jurek, B. Ziaja, R. Santra, N. D. Loh, T. Tschentscher, et al., “A comprehensive simulation framework for imaging single particles and biomolecules at the European X-ray Free-Electron Laser,” *Scientific Reports* **6**, 24791 (2016).
- [29] S. P. Hau-Riege, R. A. London, and A. Szoke, “Dynamics of biological molecules irradiated by short x-ray pulses,” *Physical Review E* **69**, 051906 (2004).
- [30] S. P. Hau-Riege, R. A. London, H. N. Chapman, A. Szoke, and N. Timneanu, “Encapsulation and Diffraction-Pattern-Correction Methods to Reduce the Effect of Damage in X-Ray Diffraction Imaging of Single Biological Molecules,” *Physical Review Letters* **98**, 198302 (2007).
- [31] Z. Jurek and G. Faigel, The effect of tamper layer on the explosion dynamics of atom clusters **50**, 35 (2008).
- [32] Z. Jurek and G. Faigel, The effect of inhomogenities on single-molecule imaging by hard XFEL pulses **86**, 68003 (2009).
- [33] S. P. Hau-Riege, S. Boutet, A. Barty, S. Bajt, M. J. Bogan, M. Frank, J. Andreasson, B. Iwan, M. M. Seibert, J. Hajdu, et al., “Sacrificial tamper slows down sample explosion in FLASH dffraction experiments,” *Physical Review Letters* **104**, 1 (2010).

## Bibliography

- [34] M. Hoener, C. Bostedt, H. Thomas, L. Landt, E. Eremina, H. Wabnitz, T. Laarmann, R. Treusch, A. R. B. de Castro, and T. Möller, “Charge recombination in soft x-ray laser produced nanoplasmas,” *Journal of Physics B* **41**, 181001 (2008).
- [35] A. Mikaberidze, U. Saalmann, and J. M. Rost, “Energy absorption of xenon clusters in helium nanodroplets under strong laser pulses,” *Physical Review A* **77**, 041201 (2008).
- [36] J. Bielecki and A. Ulmer, personal communication, Sept. 2016.
- [37] T. Fennel, K.-H. Meiws-Broer, J. Tiggesbaumker, P.-G. Reinhard, P. M. Dinh, and E. Suraud, “Laser-driven nonlinear cluster dynamics,” *Reviews of Modern Physics* **82**, 1793 (2010).
- [38] A. A. Lutman, R. Coffee, Y. Ding, Z. Huang, J. Krzywinski, T. Maxwell, M. Messerschmidt, and H. D. Nuhn, “Experimental demonstration of femtosecond two-color x-ray free-electron lasers,” *Physical Review Letters* **110**, 134801 (2013).
- [39] D. M. Mills, J. R. Helliwell, Å. Kvick, T. Ohta, I. A. Robinson, and A. Authier, “Report of the working group on synchrotron radiation nomenclature - Brightness, spectral brightness or brilliance?” *Journal of Synchrotron Radiation* **12**, 385 (2005).
- [40] J. Als-Nielsen and D. McMorrow, *Elements of modern x-ray physics* (John Wiley & Sons, Mar. 2011).
- [41] S. N. A. Laboratory, *LCLS Aerial Overlay*, (2009) <https://www.flickr.com/photos/slaclab/8577624017/>.
- [42] P. H. Bucksbaum, R. Coffee, and N. Berrah, “Chapter 5 - The First Atomic and Molecular Experiments at the Linac Coherent Light Source X-Ray Free Electron Laser,” in *Advances in atomic, molecular, and optical physics*, Vol. Volume 60 (Academic Press, 2011), pp. 239–289.
- [43] L. Young, personal communication, Feb. 10, 2017.
- [44] J. M. J. Madey, “Stimulated Emission of Bremsstrahlung in a Periodic Magnetic Field,” *Journal of Applied Physics* **42**, 1906 (1971).
- [45] A. Kondratenko and E. L. Saldin, “Generation of coherent radiation by a relativistic electron beam in an undulator\*,” *Particle Accelerators* **10**, 207 (1980).
- [46] R. Bonifacio, C. Pellegrini, and L. M. Narducci, “Collective instabilities and high-gain regime in a free electron laser,” *Optics Communications* **50**, 373 (1984).

- [47] N. Berrah, L. Fang, B. Murphy, T. Osipov, K. Ueda, E. Kukk, R. Feifel, P. van der Meulen, P. Salen, H. T. Schmidt, et al., “Double-core-hole spectroscopy for chemical analysis with an intense x-ray femtosecond laser,” *Proceedings of the National Academy of Sciences* **108**, 16912 (2011).
- [48] N. Rohringer, D. Ryan, R. A. London, M. Purvis, F. Albert, J. Dunn, J. D. Bozek, C. Bostedt, A. Graf, R. Hill, et al., “Atomic inner-shell x-ray laser at 1.46 nanometres pumped by an x-ray free-electron laser,” *Nature* **481**, 488 (2012).
- [49] M. Dell’Angela, T. Anniyev, M. Beye, R. Coffee, A. Fohlisch, J. Gladh, T. Katayama, S. Kaya, O. Krupin, J. LaRue, et al., “Real-Time Observation of Surface Bond Breaking with an X-ray Laser,” *Science* **339**, 1302 (2013).
- [50] A. Picón, C. S. Lehmann, C. Bostedt, A. Rudenko, A. Marinelli, T. Osipov, D. Rolles, N. Berrah, C. Bomme, M. Bucher, et al., “Hetero-site-specific X-ray pump-probe spectroscopy for femtosecond intramolecular dynamics,” *Nature Communications* **7**, 11652 (2016).
- [51] A. Rudenko, L. Inhester, K. Hansaki, X. Li, S. Robatjazi, B. Erk, R. Boll, K. Toyota, Y. Hao, O. Vendrell, et al., “Femtosecond response of polyatomic molecules to ultra-intense hard X-rays,” *Nature*, under review (2017).
- [52] T. Gorkhover, M. Adolph, D. Rupp, S. Schorb, S. W. Epp, B. Erk, L. Foucar, R. Hartmann, N. Kimmel, K. U. Kuhnel, et al., “Nanoplasma dynamics of single large xenon clusters irradiated with superintense x-ray pulses from the linac coherent light source free-electron laser,” *Physical Review Letters* **108**, 245005 (2012).
- [53] Z. Huang and K.-J. Kim, “Review of x-ray free-electron laser theory,” *Physical Review Special Topics - Accelerators and Beams* **10**, 034801 (2007).
- [54] K.-J. Kim, “Angular distribution of undulator power for an arbitrary deflection parameter K,” *Nuclear Instruments and Methods in Physics Research Section A* **246**, 67 (1986).
- [55] D. Rupp, *Ionization and plasma dynamics of single large xenon clusters in superintense XUV pulses* (Springer, 2016).
- [56] M. Bucher, K. R. Ferguson, T. Gorkhover, and C. Bostedt, “A transmissive single-shot soft x-ray spectrometer,” Unpublished study on feasibility of a spectrometer that is based on photoemission., 2017.
- [57] K.-J. Kim, Y. Shvyd’ko, and S. Reiche, “A proposal for an x-ray free-electron laser oscillator with an energy-recovery linac,” *Physical Review Letters* **100**, 244802 (2008).

## Bibliography

- [58] D. Ratner, R. Abela, J. Amann, C. Behrens, D. Bohler, G. Bouchard, C. Bostedt, M. Boyes, K. Chow, D. Cocco, et al., “Experimental demonstration of a soft x-ray self-seeded free-electron laser,” *Physical Review Letters* **114**, 054801 (2015).
- [59] L. B. Fletcher, H. J. Lee, T. Döppner, E. Galtier, B. Nagler, P. Heimann, C. Fortmann, S. LePape, T. Ma, M. Millot, et al., “Ultrabright x-ray laser scattering for dynamic warm dense matter physics,” *Nature Photonics* (2015) **10**. [10.1038/nphoton.2015.41](https://doi.org/10.1038/nphoton.2015.41).
- [60] J. Amann, W. Berg, V. Blank, F. J. Decker, Y. Ding, P. Emma, Y. Feng, J. Frisch, D. Fritz, J. Hastings, et al., “Demonstration of self-seeding in a hard-x-ray free-electron laser,” *Nature Photonics* **6**, 693 (2012).
- [61] E. Allaria, R. Appio, L. Badano, W. A. Barletta, S. Bassanese, S. G. Biedron, A. Borga, E. Busetto, D. Castronovo, P. Cinquegrana, et al., “Highly coherent and stable pulses from the fermi seeded free-electron laser in the extreme ultraviolet,” *Nature Photonics* **6**, 699 (2012).
- [62] K. R. Ferguson, M. Bucher, T. Gorkhover, and C. Bostedt, “Absorption spectroscopy on CO and CO<sub>2</sub> molecules,” Unpublished study on CO and CO<sub>2</sub> molecules using an ion time of flight spectrometer., 2014.
- [63] V. Kimberg, A. Sanchez-Gonzalez, L. Mercadier, C. Weninger, A. Lutman, D. Ratner, R. Coffee, M. Bucher, M. Mucke, M. Agaker, et al., “Stimulated x-ray raman scattering - a critical assessment of the building block of nonlinear x-ray spectroscopy,” *Faraday Discussions* **194**, 305 (2016).
- [64] J. C. Castagna, B. Murphy, J. Bozek, and N. Berrah, “X-ray split and delay system for soft x-rays at lcls,” *Journal of Physics: Conference Series* **425**, 152021 (2013).
- [65] S. P. Moeller, M. Yabashi, and S. P. Hau-Riege, eds., *Mirror-based soft x-ray split-and-delay system for femtosecond pump-probe experiments at LCLS*, Vol. 8504 (SPIE Proceedings, Oct. 2012), p. 850409.
- [66] N. Berrah, L. Fang, B. F. Murphy, E. Kukk, T. Y. Osipov, R. Coffee, K. R. Ferguson, H. Xiong, J.-C. Castagna, V. S. Petrovic, et al., “Two mirror X-ray pulse split and delay instrument for femtosecond time resolved investigations at the LCLS free electron laser facility,” *Optics Express* **24**, 11768 (2016).
- [67] A. Marinelli, D. Ratner, A. Lutman, J. Turner, J. Welch, F.-J. Decker, H. Loos, C. Behrens, S. Gilevich, A. Miahnahri, et al., “High-intensity double-pulse x-ray free-electron laser,” *Nature Communications* **6**, [cc7369](https://doi.org/10.1038/ncomms7369) (2015).

- [68] C. E. Liekhus-Schmaltz, I. Tenney, T. Osipov, A. Sanchez-Gonzalez, N. Berrah, R. Boll, C. Bomme, C. Bostedt, J. D. Bozek, S. Carron, et al., “Ultrafast isomerization initiated by X-ray core ionization,” *Nature Communications* **6**, 8199 (2015).
- [69] P. Emma, K. Bane, M. Cornacchia, Z. Huang, H. Schlarb, G. Stupakov, and D. Walz, “Femtosecond and subfemtosecond x-ray pulses from a self-amplified spontaneous-emission-based free-electron laser,” *Physical Review Letters* **92**, 074801 (2004).
- [70] H. Haberland, ed., *Clusters of atoms and molecules*, Vol. 52, Chemical Physics (Springer, 1994), 444 pp.
- [71] W. Miehle, O. Kandler, T. Leisner, and O. Echt, “Mass spectrometric evidence for icosahedral structure in large rare gas clusters: Ar, Kr, Xe,” *The Journal of Chemical Physics* **91**, 5940 (1989).
- [72] B. W. van de Waal, “Icosahedral, decahedral, fcc, and defect-fcc structural models for Ar-N clusters, n=500 - how plausible are they?” *The Journal of Chemical Physics* **98**, 4909 (1993).
- [73] N. V. Krainyukova, “The crystal structure problem in noble gas nanoclusters,” *Thin Solid Films* **515**, 1658 (2006).
- [74] D. Lippmann, W. C. Schieve, and C. Canestaro, “Clustering time dependence in molecular dynamics: A kinetic model,” *The Journal of Chemical Physics* **81**, 4969 (1984).
- [75] W.H. Zurek and W.C. Shieve, “Multistep Clustering and Nucleation,” *Journal of Physical Chemistry* **84**, 1479 (1980).
- [76] J. M. Soler, N. García, O. Echt, K. Sattler, and E. Recknagel, “Microcluster growth: transition from successive monomer addition to coagulation,” *Physical Review Letters* **49**, 1857 (1982).
- [77] J. Farges, M. F. de Feraudy, B. Raoult, and G. Torchet, “Structure and temperature of rare gas clusters in a supersonic expansion,” *Surface Science* **106**, 95 (1981).
- [78] J. Gspann, “On the phase of metal clusters,” in *Metal clusters*, edited by F. Träger and G. zu Putlitz (Apr. 1986), pp. 43–45.
- [79] L. F. Gomez, E. Loginov, R. Sliter, and A. F. Vilesov, “Sizes of large He droplets,” *Journal of Chemical Physics* **135**, 154201 (2011).
- [80] D. R. Miller, *Free jet sources*, edited by G. Scoles (Oxford University Press, Inc., 1988) Chap. 2, pp. 14–53.
- [81] I. Yamada, J. Matsuo, N. Toyoda, and A. Kirkpatrick, “Materials processing by gas cluster ion beams,” *Materials Science and Engineering: R: Reports* **34**, 231 (2001).

## Bibliography

- [82] J. Wörmer, M. Joppien, and T. Möller, “Mass determination of free van der Waals clusters from absorption and scattering measurements,” *Chemical Physics Letters* **182**, 632 (1991).
- [83] O. F. Hagena, “Cluster Formation in Expanding Supersonic Jets: Effect of Pressure, Temperature, Nozzle Size, and Test Gas,” *The Journal of Chemical Physics* **56**, 1793 (1972).
- [84] O. F. Hagena, “Nucleation and growth of clusters in expanding nozzle flows,” *Surface Science* **106**, 101 (1981).
- [85] O. F. Hagena, “Condensation in free jets: Comparison of rare gases and metals,” *Zeitschrift für Physik D Atoms, Molecules and Clusters* **4**, 291 (1987).
- [86] S. Schorb, “Size-dependent ultrafast ionization dynamics of nanoscale samples in intense femtosecond x-ray free-electron laser pulses,” Thesis (Technische Universität Berlin, 2012).
- [87] U. Buck and R. Krohne, “Cluster size determination from diffractive He atom scattering,” *The Journal of Chemical Physics* **105**, 5408 (1996).
- [88] F. Dorchies, F. Blasco, T. Caillaud, J. Stevefelt, C. Stenz, A. S. Boldarev, and V. A. Gasilov, “Spatial distribution of cluster size and density in supersonic jets as targets for intense laser pulses,” *Physical Review A* **68**, 023201 (2003).
- [89] O. F. Hagena, “Cluster ion sources (invited),” *Review of Scientific Instruments* **63**, 2374 (1992).
- [90] A. M. Bush, A. J. Bell, J. G. Frey, and J.-M. Mestdagh, “Rayleigh Scattering of Laser and Synchrotron Radiation from Pulsed Free Jets of Ar n and (N<sub>2</sub>O) n Clusters,” *The Journal of Physical Chemistry A* **102**, 6457 (1998).
- [91] M. Arbeiter and T. Fennel, “Ionization heating in rare-gas clusters under intense XUV laser pulses,” *Physical Review A* **82**, 1 (2010).
- [92] D. Rupp, M. Adolph, L. Flückiger, T. Gorkhover, J. P. Müller, M. Müller, M. Sauppe, D. Wolter, S. Schorb, R. Treusch, et al., “Generation and structure of extremely large clusters in pulsed jets,” *Journal of Chemical Physics* **141**, 044306 (2014).
- [93] L. S. Bartell, “Diffraction studies of clusters generated in supersonic flow,” *Chemical Reviews* **86**, 491 (1986).
- [94] D. Rupp, M. Adolph, T. Gorkhover, S. Schorb, D. Wolter, R. Hartmann, N. Kimmel, C. Reich, T. Feigl, A. R. B. de Castro, et al., “Identification of twinned gas phase clusters by single-shot scattering with intense soft x-ray pulses,” *New Journal of Physics* **14**, 055016 (2012).

- [95] T. E. Gough, M. Mengel, P. A. Rowntree, and G. Scoles, “Infrared spectroscopy at the surface of clusters: SF<sub>6</sub> on Ar,” *The Journal of Chemical Physics* **83**, 4958 (1985).
- [96] M. Hartmann, R. E. Miller, J. P. Toennies, and A. Vilesov, “Rotationally Resolved Spectroscopy of SF<sub>6</sub> in Liquid Helium Clusters: A Molecular Probe of Cluster Temperature,” *Physical Review Letters* **75**, 1566 (1995).
- [97] K. R. Ferguson, “Crystal structure determinations of xenon nanoparticles and x-ray induced transient lattice contraction in the solid-to-plasma transition,”  PhD thesis (Stanford University, Feb. 2016).
- [98] G. P. Williams, ed., *X-ray data booklet* (Lawrence Berkeley National Laboratory, Apr. 2009).
- [99] R. Pugliese and G. Paolucci, *Atomic calculation of photoionization cross-sections and asymmetry parameters*, (Aug. 2016) <https://vuo.elettra.eu/services/elements/WebElements.html>.
- [100] J. Yeh and I. Lindau, “Atomic subshell photoionization cross sections and asymmetry parameters: 1 ≤ Z ≤ 103,” *Atomic Data and Nuclear Data Tables* **32**, 1 (1985).
- [101] J.-J. Yeh, *Atomic calculation of photoionization cross-sections and asymmetry parameters* (Gordon & Breach Science Publ.; AT&T Bell Laboratories, 1993).
- [102] R. Cowan, *Los Alamos Atomic Physics Codes*, Los Alamos National Laboratory, (2016) <http://aphysics2.lanl.gov/tempweb/lanl/> (visited on 02/09/2017).
- [103] R. D. Cowan, *The theory of atomic structure and spectra* (University of California Press, Sept. 11, 1981), 650 pp.
- [104] W. Demtröder, *Experimentalphysik 3: Atome, Moleküle und Festkörper* (Springer, 2005).
- [105] M. Bucher, K. R. Ferguson, G. T., and B. C., “The LAMP endstation in the AMO instrument at the Linac Coherent Light Source,” Unpublished study on the LAMP endstation with focus on the pnCCD detectors., 2017.
- [106] L. Foucar, “CFEL–ASG Software Suite (CASS): usage for free-electron laser experiments with biological focus,” *Journal of Applied Crystallography* **49**, 1336 (2016).
- [107] B. Rudek, S. K. Son, L. Foucar, S. W. Epp, B. Erk, R. Hartmann, M. Adolph, R. Andritschke, A. Aquila, N. Berrah, et al., “Ultra-efficient ionization of heavy atoms by intense x-ray free-electron laser pulses,” *Nature Photonics* **6**, 858 (2012).
- [108] M. Krause, F. Stevie, L. Lewis, T. Carlson, and W. Moddeman, “Multiple excitation of neon by photon and electron impact,” *Physics Letters A* **31**, 81 (1970).

## Bibliography

- [109] V. Schmidt, “Auger spectrum of neon following 1s ionization,” in *Electron spectrometry of atoms using synchrotron radiation*: (Cambridge University Press, May 1997), pp. 73–94.
- [110] C. Buth, R. Santra, and L. S. Cederbaum, “Impact of interatomic electronic decay processes on Xe 4d hole decay in the xenon fluorides,” *The Journal of Chemical Physics* **119**, 10575 (2003).
- [111] J. P. Briand, P. Chevallier, M. Tavernier, and J. P. Rozet, “Observation of K Hypersatellites and KL Satellites in the X-Ray Spectrum of Doubly K-Ionized Gallium,” *Physical Review Letters* **27**, 777 (1971).
- [112] D. Coster and R. D. L. Kronig, “New type of Auger effect and its influence on the X-ray spectrum,” *Physica* **2**, 13 (1935).
- [113] M. M. Y. Berezin and S. Achilefu, “Fluorescence Lifetime Measurements and Biological Imaging,” *Chemical Reviews* **110**, 2641 (2011).
- [114] P. J. Ho, C. Bostedt, S. Schorb, and L. Young, “Theoretical Tracking of Resonance-Enhanced Multiple Ionization Pathways in X-ray Free-Electron Laser Pulses,” *Physical Review Letters* **113**, 253001 (2014).
- [115] A. Guinier and G. Fournet, *Small-angle scattering of x-rays* (John Wiley & Sons, New York, 1955).
- [116] I. A. Vartanyants and I. K. Robinson, “Partial coherence effects on the imaging of small crystals using coherent x-ray diffraction,” *Journal of Physics: Condensed Matter* **13**, 10593 (2001).
- [117] S. K. Sinha, E. B. Sirota, S. Garoff, and H. B. Stanley, “X-ray and neutron scattering from rough surfaces,” *Physical Review B* **38**, 2297 (1988).
- [118] P. J. Ho, personal communication, Feb. 2017.
- [119] M. F. Hantke, T. Ekeberg, and F. R. N. C. Maia, “Condor : a simulation tool for flash X-ray imaging,” *Journal of Applied Crystallography* **49**, 1356 (2016).
- [120] D. Attwood, *Soft X-Rays and Extreme Ultraviolet Radiation: Principles and Applications* (Cambridge University Press, 2012).
- [121] S. Schorb, D. Rupp, M. L. Swiggers, R. N. Coffee, M. Messerschmidt, G. Williams, J. D. Bozek, S.-I. Wada, O. Kornilov, T. Möller, et al., “Size-dependent ultrafast ionization dynamics of nanoscale samples in intense femtosecond X-ray free-electron-laser pulses,” *Physical Review Letters* **108**, 233401 (2012).

- [122] M. Arbeiter and T. Fennel, “Rare-gas clusters in intense VUV, XUV and soft x-ray pulses: signatures of the transition from nanoplasma-driven cluster expansion to Coulomb explosion in ion and electron spectra,” *New Journal of Physics* **13**, 053022 (2011).
- [123] T. Ditmire, T. Donnelly, A. M. Rubenchik, R. W. Falcone, and M. D. Perry, “Interaction of intense laser pulses with atomic clusters,” *Physical Review A* **53**, 3379 (1996).
- [124] C. Bostedt, M. Adolph, E. Eremina, M. Hoener, D. Rupp, S. Schorb, H. Thomas, A. R. B. de Castro, and T. Möller, “Clusters in intense FLASH pulses: ultrafast ionization dynamics and electron emission studied with spectroscopic and scattering techniques,” *Journal of Physics B* **43**, 194011 (2010).
- [125] C. Peltz, C. Varin, T. Brabec, and T. Fennel, “Time-resolved x-ray imaging of anisotropic nanoplasma expansion,” *Physical Review Letters* **113**, 1 (2014).
- [126] H. Wabnitz, L. Bittner, A. R. B. de Castro, R. Döhrmann, P. Gürtler, T. Laarmann, W. Laasch, J. Schulz, A. Swiderski, K. von Haeften, et al., “Multiple ionization of atom clusters by intense soft X-rays from a free-electron laser,” *Nature* **420**, 482 (2002).
- [127] T. Laarmann, A. R. B. de Castro, P. Gürtler, W. Laasch, J. Schulz, H. Wabnitz, and T. Möller, “Interaction of Argon clusters with intense VUV-laser radiation: The role of electronic structure in the energy-deposition process,” *Physical Review Letters* **92**, 143401 (2004).
- [128] C. Bostedt, H. Thomas, M. Hoener, E. Eremina, T. Fennel, K. H. Meiwes-Broer, H. Wabnitz, M. Kuhlmann, E. Plönjes, K. Tiedtke, et al., “Multistep ionization of argon clusters in intense femtosecond extreme ultraviolet pulses,” *Physical Review Letters* **100**, 12 (2008).
- [129] T. Laarmann, M. Rusek, H. Wabnitz, J. Schulz, A. R. B. de Castro, P. Gürtler, W. Laasch, and T. Möller, “Emission of thermally activated electrons from rare gas clusters irradiated with intense VUV light pulses from a free electron laser,” *Physical Review Letters* **95**, 3 (2005).
- [130] C. Bostedt, H. Thomas, M. Hoener, T. Möller, U. Saalmann, I. Georgescu, C. Gnadtke, and J. M. Rost, “Fast electrons from multi-electron dynamics in xenon clusters induced by inner-shell ionization,” *New Journal of Physics* **12**, 083004 (2010).
- [131] M. Lezius, S. Dobosz, D. Normand, and M. Schmidt, “Explosion Dynamics of Rare Gas Clusters in Strong Laser Fields,” *Physical Review Letters* **80**, 261 (1998).

## Bibliography

- [132] E. Springate, N. Hay, J. W. G. Tisch, M. B. Mason, T. Ditmire, M. H. R. Hutchinson, and J. P. Marangos, “Explosion of atomic clusters irradiated by high-intensity laser pulses: scaling of ion energies with cluster and laser parameters,” *Physical Review A* **61**, 063201 (2000).
- [133] E. K. Curwood, H. M. Quiney, and K. A. Nugent, “Determining electronic damage to biomolecular structures in x-ray free-electron-laser imaging experiments,” *Physical Review A* **87**, 053407 (2013).
- [134] D. Rupp, L. Flückiger, M. Adolph, T. Gorkhover, M. Krikunova, J. P. Müller, M. Müller, T. Oelze, Y. Ovcharenko, B. Röben, et al., “Recombination-Enhanced Surface Expansion of Clusters in Intense Soft X-Ray Laser Pulses,” *Physical Review Letters* **117**, 153401 (2016).
- [135] S. Schorb, T. Gorkhover, J. P. Cryan, J. M. Glownia, M. R. Bionta, R. N. Coffee, B. Erk, R. Boll, C. Schmidt, D. Rolles, et al., “X-ray–optical cross-correlator for gas-phase experiments at the linac coherent light source free-electron laser,” *Applied Physics Letters* **100**, 121107 (2012).
- [136] S. P. Hau-Riege and H. N. Chapman, “Modeling of the damage dynamics of nanospheres exposed to x-ray free-electron-laser radiation,” *Physical Review E* **77**, 1 (2008).
- [137] J. Küpper, S. Stern, L. Holmegaard, F. Filsinger, A. Rouzée, A. Rudenko, P. Johnsson, A. V. Martin, M. Adolph, A. Aquila, et al., “X-ray diffraction from isolated and strongly aligned gas-phase molecules with a free-electron laser,” *Physical Review Letters* **112**, 083002 (2014).
- [138] F. R. N. C. Maia, T. Ekeberg, N. Timneanu, D. van der Spoel, and J. Hajdu, “Structural variability and the incoherent addition of scattered intensities in single-particle diffraction,” *Physical Review E* **80**, 031905 (2009).
- [139] B. Ziaja, H. N. Chapman, R. Santra, T. Laarmann, E. Weckert, C. Bostedt, and T. Möller, “Heterogeneous clusters as a model system for the study of ionization dynamics within tampered samples,” *Physical Review A* **84**, 033201 (2011).
- [140] K. von Haeften, A. R. B. de Castro, M. Joppien, L. Moussavizadeh, R. von Pietrowski, and T. Möller, “Discrete visible luminescence of helium atoms and molecules desorbing from helium clusters: the role of electronic, vibrational, and rotational energy transfer,” *Physical Review Letters* **78**, 4371 (1997).

- [141] R. von Pietrowski, K. von Haeften, T. Laarmann, T. Möller, L. Museur, and A. V. Kanaev, “Electronic and geometric structure of doped rare-gas clusters: surface, site and size effects studied with luminescence spectroscopy,” *The European Physical Journal D* **38**, 323 (2006).
- [142] F. Stienkemeier and K. K. Lehmann, “Spectroscopy and dynamics in helium nanodroplets,” *Journal of Physics B* **39**, R127 (2006).
- [143] D. Buchta, S. R. Krishnan, N. B. Brauer, M. Drabbels, P. O’Keeffe, M. Devetta, M. Di Fraia, C. Callegari, R. Richter, M. Coreno, et al., “Charge Transfer and Penning Ionization of Dopants in or on Helium Nanodroplets Exposed to EUV Radiation,” *The Journal of Physical Chemistry A* **117**, 4394 (2013).
- [144] B. Richter and S. C. C. Ting, *The Nobel Price in Physics*, The Nobel Foundation, “For their pioneering work in the discovery of a heavy elementary particle of a new kind”, 1976.
- [145] J. I. Friedman, H. W. Kendall, and R. E. Taylor, *The Nobel Price in Physics*, The Nobel Foundation, “For their pioneering investigations concerning deep inelastic scattering of electrons on protons and bound neutrons, which have been of essential importance for the development of the quark model in particle physics”, 1990.
- [146] M. L. Perl and F. Reines, *The Nobel Price in Physics*, The Nobel Foundation, “For pioneering experimental contributions to lepton physics”, 1995.
- [147] C. Bostedt, J. D. Bozek, P. H. Bucksbaum, R. N. Coffee, J. B. Hastings, Z. Huang, R. W. Lee, S. Schorb, J. N. Corlett, P. Denes, et al., “Ultra-fast and ultra-intense x-ray sciences: first results from the Linac Coherent Light Source free-electron laser,” *Journal of Physics B* **46**, 164003 (2013).
- [148] A. Munke, J. Andreasson, A. Aquila, S. Awel, K. Ayyer, A. Barty, R. J. Bean, P. Berntsen, J. Bielecki, S. Boutet, et al., “Coherent diffraction of single Rice Dwarf virus particles using hard X-rays at the Linac Coherent Light Source,” *Scientific Data* **3**, 160064 (2016).
- [149] A. Sanchez-Gonzalez, T. R. Barillot, R. J. Squibb, P. Kolorenč, M. Agaker, V. Averbukh, M. J. Bearpark, C. Bostedt, J. D. Bozek, S. Bruce, et al., “Auger electron and photoabsorption spectra of glycine in the vicinity of the oxygen K-edge measured with an X-FEL,” *Journal of Physics B* **48**, 234004 (2015).
- [150] C. S. Lehmann, A. Picon, C. Bostedt, A. Rudenko, A. Marinelli, D. Moonshiram, T. Osipov, D. Rolles, N. Berrah, C. Bomme, et al., “Ultrafast x-ray-induced nuclear dynamics in diatomic molecules using femtosecond x-ray-pump-x-ray-probe spectroscopy,” *Physical Review A* **94**, 1 (2016).

## Bibliography

- [151] M. J. MacDonald, T. Gorkhover, B. Bachmann, M. Bucher, S. Carron, R. N. Coffee, R. P. Drake, K. R. Ferguson, L. B. Fletcher, E. J. Gamboa, et al., “Measurement of high-dynamic range x-ray Thomson scattering spectra for the characterization of nano-plasmas at LCLS,” *Review of Scientific Instruments* **87**, 11E709 (2016).
- [152] E. Gamboa, B. Bachmann, D. Kraus, M. MacDonald, M. Bucher, S. Carron, R. Coffee, R. Drake, J. Emig, K. Ferguson, et al., “Dual crystal x-ray spectrometer at 1.8 keV for high repetition-rate single-photon counting spectroscopy experiments,” *Journal of Instrumentation* **11**, P08015 (2016).
- [153] C. Bernardo, R. M. P. Tanyag, C. Jones, C. Bacellar, M. Bucher, K. R. Ferguson, D. Rupp, M. P. Ziemkiewicz, L. F. Gomez, A. S. Chatterley, et al., “Shapes of rotating superfluid helium nanodroplets,” *Physical Review B* **95**, 064510 (2017).
- [154] J. D. Bozek, “AMO instrumentation for the LCLS X-ray FEL,” *The European Physical Journal Special Topics* **169**, 129 (2009).
- [155] C. Behrens, F. J. Decker, Y. Ding, V. A. Dolgashev, J. Frisch, Z. Huang, P. Krejcik, H. Loos, A. Lutman, T. J. Maxwell, et al., “Few-femtosecond time-resolved measurements of x-ray free-electron lasers,” *Nature Communications* **5**, 3762 (2014).
- [156] S. Moeller, J. Arthur, A. Brachmann, R. Coffee, F. J. Decker, Y. Ding, D. Dowell, S. Edstrom, P. Emma, Y. Feng, et al., “beamlines and diagnostics at LCLS,” *Nuclear Instruments and Methods in Physics Research Section A* **635**, S6 (2011).
- [157] S. P. Hau-Riege, R. M. Bionta, D. D. Ryutov, R. A. London, E. Ables, K. I. Kishiyama, S. Shen, M. A. McKernan, D. H. McMahon, M. Messerschmidt, et al., “Near-Ultraviolet Luminescence of N<sub>2</sub> Irradiated by Short X-Ray Pulses,” *Physical Review Letters* **105**, 043003 (2010).
- [158] W. F. Schlotter, J. J. Turner, M. Rowen, P. Heimann, M. Holmes, O. Krupin, M. Messerschmidt, S. Moeller, J. Krzywinski, R. Soufli, et al., “The soft x-ray instrument for materials studies at the linac coherent light source x-ray free-electron laser,” *Review of Scientific Instruments* **83**, 043107 (2012).
- [159] R. Soufli, M. Fernández-Perea, S. L. Baker, J. C. Robinson, E. M. Gullikson, P. Heimann, V. V. Yashchuk, W. R. McKinney, W. F. Schlotter, and M. Rowen, “Development and calibration of mirrors and gratings for the soft x-ray materials science beamline at the Linac Coherent Light Source free-electron laser,” *Applied Optics* **51**, 2118 (2012).
- [160] G. L. Dakovski, P. Heimann, M. Holmes, O. Krupin, M. P. Miniti, A. Mitra, S. Moeller, M. Rowen, W. F. Schlotter, and J. J. Turner, “The soft x-ray research instrument at the linac coherent light source,” *Journal of Synchrotron Radiation* **22**, 498 (2015).

- [161] L. Strüder, S. Epp, D. Rolles, R. Hartmann, P. Holl, G. Lutz, H. Soltau, R. Eckart, C. Reich, K. Heinzinger, et al., “Large-format, high-speed, X-ray pnCCDs combined with electron and ion imaging spectrometers in a multipurpose chamber for experiments at 4th generation light sources,” Nuclear Instruments and Methods in Physics Research Section A **614**, 483 (2010).
- [162] J. Turner, personal communication, June 2, 2016.
- [163] P. Kirkpatrick and A. V. Baez, “Formation of optical images by X-rays.,” Journal of the Optical Society of America **38**, 766 (1948).
- [164] L. Juha, S. Bajt, and R. A. London, eds., *X-ray laser-induced ablation of lead compounds*, Vol. 8077, Damage to VUV, EUV, and X-ray Optics III 807718 (SPIE Proceedings, May 2011), p. 807718.
- [165] J. Chalupský, P. Bohacek, V. Hajkova, S. P. Hau-Riege, P. A. Heimann, L. Juha, J. Krzywinski, M. Messerschmidt, S. P. Moeller, B. Nagler, et al., “Comparing different approaches to characterization of focused x-ray laser beams,” Nuclear Instruments and Methods in Physics Research Section A **631**, 130 (2011).
- [166] R. Hartmann, W. Buttler, H. Gorke, S. Herrmann, P. Holl, N. Meidinger, H. Soltau, and L. Strüder, “A high-speed pnCCD detector system for optical applications,” Nuclear Instruments and Methods in Physics Research Section A **568**, 118 (2006).
- [167] I. Ordavo, S. Ihle, V. Arkadiev, O. Scharf, H. Soltau, A. Bjeoumikhov, S. Bjeoumikhova, G. Buzanich, R. Gubzhokov, A. Günther, et al., “A new pnCCD-based color X-ray camera for fast spatial and energy-resolved measurements,” Nuclear Instruments and Methods in Physics Research Section A **654**, 250 (2011).
- [168] L. Strüder, U. Briel, K. Dennerl, R. Hartmann, E. Kendziorra, N. Meidinger, E. Pfeffermann, C. Reppin, B. Aschenbach, W. Bornemann, et al., “The European Photon Imaging Camera on XMM-Newton: The pn-CCD camera,” Astronomy & Astrophysics **365**, L18 (2001).
- [169] P. Krejcik, S. Allison, R. Akre, K. Kotturi, M. Browne, J. Dusatko, W. White, D. Rogind, A. Gromme, L. Dalesio, et al., *Timing and Synchronization at the LCLS*, tech. rep. SLAC-PUB-12593, presented at 8th European Workshop on Beam Diagnostics and Instrumentation for Particle Accelerators (SLAC National Accelerator Laboratory, June 2007).
- [170] W. E. Stephens, “Pulsed mass spectrometer with time dispersion,” in Proceedings of the american physical society (June 1946), p. 691.

## Bibliography

- [171] K. K. Murray, R. K. Boyd, M. N. Eberlin, G. J. Langley, L. Li, and Y. Naito, “Definitions of terms relating to mass spectrometry (IUPAC Recommendations 2013),” *Pure and Applied Chemistry* **85**, 1515 (2013).
- [172] T. Osipov, personal communication, Aug. 13, 2013.
- [173] G. Doumy, C. Roedig, S.-K. Son, C. I. Blaga, A. D. DiChiara, R. Santra, N. Berrah, C. Bostedt, J. D. Bozek, P. H. Bucksbaum, et al., “Nonlinear atomic response to intense ultrashort x rays,” *Physical Review Letters* **106**, 083002 (2011).
- [174] J. M. Liu, “Simple technique for measurements of pulsed gaussian-beam spot sizes,” *Optics Letters* **7**, 196 (1982).
- [175] B. Henke, E. Gullikson, and J. Davis, *X-Ray interactions: photoabsorption, scattering, transmission, and reflection at E = 50-30,000 eV, Z = 1-92*, 1993.
- [176] J. Chalupský, J. Krzywinski, L. Juha, V. Hájková, J. Cihelka, T. Burian, L. Vyšín, J. Gaudin, A. Gleeson, M. Jurek, et al., “Spot size characterization of focused non-Gaussian X-ray laser beams,” *Optics Express* **18**, 27836 (2010).
- [177] J. Chalupský, T. Burian, V. Hájková, L. Juha, T. Polcar, J. Gaudin, M. Nagasono, R. Sobierajski, M. Yabashi, and J. Krzywinski, “Fluence scan: an unexplored property of a laser beam,” *Optics express* **21**, 26363 (2013).
- [178] A. Perazzo, *LCLS Data Analysis Strategy*, tech. rep. (SLAC National Accelerator Laboratory, Feb. 2016).
- [179] D. Damiani, M. Dubrovin, I. Gaponenko, W. Kroeger, T. J. Lane, A. Mitra, C. P. O’Grady, A. Salnikov, A. Sanchez-Gonzalez, D. Schneider, et al., “Linac Coherent Light Source data analysis using psana,” *Journal of Applied Crystallography* **49**, 672 (2016).
- [180] M. F. Hantke and L. Foucar, personal communication, June 2016.
- [181] Y. Bruck and L. Sodin, “On the ambiguity of the image reconstruction problem,” *Optics Communications* **30**, 304 (1979).
- [182] R. Bates, *Fourier phase problems are uniquely solvable in more than one dimension, 1. Underlying theory*, Stuttgart, 1981.
- [183] D. Sayre, “Some implications of a theorem due to Shannon,” *Acta Crystallographica* **5**, 843 (1952).
- [184] G. J. Williams, H. M. Quiney, A. G. Peele, and K. A. Nugent, “Fresnel coherent diffractive imaging: treatment and analysis of data,” *New Journal of Physics* **12**, 035020 (2010).
- [185] J. R. Fienup, “Phase retrieval algorithms: a comparison,” *Applied Optics* **21**, 2758 (1982).

- [186] J. R. Fienup, “Reconstruction of an object from the modulus of its Fourier transform,” *Optics letters* **3**, 27 (1978).
- [187] F. R. N. C. Maia, T. Ekeberg, D. van der Spoel, and J. Hajdu, “Hawk: the image reconstruction package for coherent X-ray diffractive imaging,” *Journal of Applied Crystallography* **43**, 1535 (2010).
- [188] M. M. Seibert, S. Boutet, M. Svenda, T. Ekeberg, F. R. N. C. Maia, M. J. Bogan, N. Timneanu, A. Barty, S. Hau-Riege, C. Caleman, et al., “Femtosecond diffractive imaging of biological cells,” *Journal of Physics B* **43**, 194015 (2010).
- [189] F. R. Maia, “The coherent x-ray imaging data bank,” *Nature Methods* **9**, 854 (2012).
- [190] D. R. Luke, “Relaxed averaged alternating reflections for diffraction imaging,” *Inverse Problems* **21**, 37 (2005).
- [191] J. Geilhufe, C. Tieg, B. Pfau, C. M. Günther, E. Guehrs, S. Schaffert, and S. Eisebitt, “Extracting depth information of 3-dimensional structures from a single-view X-ray Fourier-transform hologram,” *Optics Express* **22**, 24959 (2014).
- [192] H. N. Chapman, A. Barty, S. Marchesini, A. Noy, S. P. Hau-Riege, C. Cui, M. R. Howells, R. Rosen, H. He, J. C. H. Spence, et al., “High-resolution ab initio three-dimensional x-ray diffraction microscopy,” *Journal of the Optical Society of America A* **23**, 1179 (2006).
- [193] M. F. Hantke, D. Hasse, F. R. N. C. Maia, T. Ekeberg, K. John, M. Svenda, N. D. Loh, A. V. Martin, N. Timneanu, D. S. D. Larsson, et al., “High-throughput imaging of heterogeneous cell organelles with an X-ray laser,” *Nature Photonics* **8**, 943 (2014).
- [194] N. T. D. Loh and V. Elser, “Reconstruction algorithm for single-particle diffraction imaging experiments,” *Physical Review E* **80**, 1 (2009).
- [195] B. J. Dauner, M. F. Hantke, C. Nettelblad, and F. R. N. C. Maia, “Hummingbird: monitoring and analyzing flash X-ray imaging experiments in real time,” *Journal of Applied Crystallography* **49**, 1042 (2016).
- [196] B. Schütte, T. Oelze, M. Krikunova, M. Arbeiter, T. Fennel, M. J. J. Vrakking, and A. Rouzée, “Real-time fragmentation dynamics of clusters ionized by intense extreme-ultraviolet pulses,” *Journal of Physics B* **48**, 185101 (2015).
- [197] B. Schütte, F. Campi, M. Arbeiter, T. Fennel, M. J. J. Vrakking, and A. Rouzée, “Tracing Electron-Ion Recombination in Nanoplasmas Produced by Extreme-Ultraviolet Irradiation of Rare-Gas Clusters,” *Physical Review Letters* **112**, 253401 (2014).

## Bibliography

- [198] M. Krikunova, T. Maltezopoulos, A. Azima, M. Schlie, U. Frühling, H. Redlin, R. Kalms, S. Cunovic, N. M. Kabachnik, M. Wieland, et al., “Time-resolved ion spectrometry on xenon with the jitter-compensated soft x-ray pulses of a free-electron laser,” *New Journal of Physics* **11**, 123019 (2009).
- [199] A. Sugishima, H. Iwayama, S. Yase, H. Murakami, K. Nagaya, M. Yao, H. Fukuzawa, X.-J. Liu, K. Motomura, K. Ueda, et al., “Charge and energy transfer in argon-core–neon-shell clusters irradiated by free-electron-laser pulses at 62 nm,” *Physical Review A* **86**, 033203 (2012).
- [200] M. Müller, L. Schroedter, T. Oelze, L. Nösel, A. Przystawik, A. Kickermann, M. Adolph, T. Gorkhover, L. Flückiger, M. Krikunova, et al., “Ionization dynamics of XUV excited clusters: the role of inelastic electron collisions,” *Journal of Physics B: Atomic, Molecular and Optical Physics* **48**, 174002 (2015).
- [201] S. Schütte and U. Buck, “Strong fragmentation of large rare gas clusters by high energy electron impact,” *International Journal of Mass Spectrometry* **220**, 183 (2002).
- [202] A. Mikaberidze, U. Saalmann, and J. M. Rost, “Laser-Driven Nanoplasmas in Doped Helium Droplets: Local Ignition and Anisotropic Growth,” *Physical Review Letters* **102**, 128102 (2009).
- [203] G. J. Williams, personal communication, June 16, 2016.
- [204] T. Gorkhover, “Ultrafast light induced dynamics of xe nanoparticles studies with a combination of intense infrared and x-ray pulses,” Thesis (Technische Universität Berlin, 2014).
- [205] J. P. Toennies and A. F. Vilesov, “Superfluid Helium Droplets: A Uniquely Cold Nanomatrix for Molecules and Molecular Complexes,” *Angewandte Chemie International Edition* **43**, 2622 (2004).
- [206] L. F. Gomez, E. Loginov, and A. F. Vilesov, “Traces of Vortices in Superfluid Helium Droplets,” *Physical Review Letters* **108**, 155302 (2012).
- [207] E. Loginov, L. F. Gomez, N. Chiang, A. Halder, N. Guggemos, V. V. Kresin, and A. F. Vilesov, “Photoabsorption of AG<sub>N</sub>(N ~ 6 – 6000) Nanoclusters Formed in Helium Droplets: Transition from Compact to Multicenter Aggregation,” *Physical Review Letters* **106**, 233401 (2011).
- [208] A. Al-Haddad, A. Picon, M. Bucher, G. Doumy, A. Luttmann, A. Marinelli, T. Maxwell, S. Moeller, D. Ray, T. Osipov, et al., “Time-resolved Two-Color X-ray Pump/X-ray Probe Photoelectron Spectroscopy at LCLS,” in 48th Annual Meeting of the APS Division of Atomic, Molecular and Optical Physics (June 2017).



# Publikationsliste

- K. R. Ferguson, **M. Bucher**, J. D. Bozek, S. Carron, J.-C. Castagna, R. Coffee, G. I. Curiel, M. Holmes, J. Krzywinski, M. Messerschmidt, M. Minitti, A. Mitra, S. Moeller, P. Noonan, T. Osipov, S. Schorb, M. Swiggers, A. Wallace, J. Yin, and C. Bostedt, “The Atomic, Molecular and Optical Science instrument at the Linac Coherent Light Source,” *Journal of Synchrotron Radiation* **22**, 492 (2015).
- K. R. Ferguson, **M. Bucher**, T. Gorkhover, S. Boutet, H. Fukuzawa, J. E. Koglin, Y. Kumagai, A. Lutman, A. Marinelli, M. Messerschmidt, K. Nagaya, J. Turner, K. Ueda, G. J. Williams, P. H. Bucksbaum, and C. Bostedt, “Transient lattice contraction in the solid-to-plasma transition,” *Science Advances* **2**, e1500837 (2016).
- A. Picón, C. S. Lehmann, C. Bostedt, A. Rudenko, A. Marinelli, T. Osipov, D. Rolles, N. Berrah, C. Bomme, **M. Bucher**, G. Doumy, B. Erk, K. R. Ferguson, T. Gorkhover, P. J. Ho, E. P. Kanter, B. Krässig, J. Krzywinski, A. A. Lutman, A. M. March, D. Moonshiram, D. Ray, L. Young, S. T. Pratt, and S. H. Southworth, “Hetero-site-specific X-ray pump-probe spectroscopy for femtosecond intramolecular dynamics,” *Nature Communications* **7**, 11652 (2016).
- A. Rudenko, L. Inhester, K. Hansaki, X. Li, S. Robatjazi, B. Erk, R. Boll, K. Toyota, Y. Hao, O. Vendrell, C. Bomme, E. Savelyev, B. Rudek, L. Foucar, S. Southworth, C. Lehman, B. Krässig, T. Marchenko, M. Simon, K. Ueda, K. Ferguson, **M. Bucher**, T. Gorkhover, S. Carron, R. Alonso-Mori, J. Koglin, J. Correa, G. Williams, S. Boutet, L. Young, C. Bostedt, S.-K. Son, R. Santra, and D. Rolles, “Femtosecond response of polyatomic molecules to ultra-intense hard X-rays,” *Nature*, under review (2017).
- V. Kimberg, A. Sanchez-Gonzalez, L. Mercadier, C. Weninger, A. Lutman, D. Ratner, R. Coffee, **M. Bucher**, M. Mucke, M. Agaker, C. Sathe, C. Bostedt, J. Nordgren, J. E. Rubensson, and N. Rohringer, “Stimulated x-ray raman scattering - a critical assessment of the building block of nonlinear x-ray spectroscopy,” *Faraday Discussions* **194**, 305 (2016).
- A. Munke, J. Andreasson, A. Aquila, S. Awel, K. Ayyer, A. Barty, R. J. Bean, P. Berntsen, J. Bielecki, S. Boutet, **M. Bucher**, H. N. Chapman, B. J. Daurer, H. DeMirci, V. Elser, P. Fromme, J. Hajdu, M. F. Hantke, A. Higashiura, B. G. Hogue, A. Hosseiniزاده, Y. Kim, R. A. Kirian, H. K. Reddy, T.-Y. Lan, D. S. Larsson, H. Liu, N. D. Loh, F. R. Maia, A. P. Mancuso, K.

## Publikationsliste

- Mühlig, A. Nakagawa, D. Nam, G. Nelson, C. Nettelblad, K. Okamoto, A. Ourmazd, M. Rose, G. van der Schot, P. Schwander, M. M. Seibert, J. A. Sellberg, R. G. Sierra, C. Song, M. Svenda, N. Timneanu, I. A. Vartanyants, D. Westphal, M. O. Wiedorn, G. J. Williams, P. L. Xavier, C. H. Yoon, and J. Zook, “Coherent diffraction of single Rice Dwarf virus particles using hard X-rays at the Linac Coherent Light Source,” *Scientific Data* **3**, 160064 (2016).
- C. S. Lehmann, A. Picon, C. Bostedt, A. Rudenko, A. Marinelli, D. Moonshiram, T. Osipov, D. Rolles, N. Berrah, C. Bomme, **M. Bucher**, G. Doumy, B. Erk, K. R. Ferguson, T. Gorkhover, P. J. Ho, E. P. Kanter, B. Krässig, J. Krzywinski, A. A. Lutman, A. M. March, D. Ray, L. Young, S. T. Pratt, and S. H. Southworth, “Ultrafast x-ray-induced nuclear dynamics in diatomic molecules using femtosecond x-ray-pump-x-ray-probe spectroscopy,” *Physical Review A* **94**, 1 (2016).
- M. J. MacDonald, T. Gorkhover, B. Bachmann, **M. Bucher**, S. Carron, R. N. Coffee, R. P. Drake, K. R. Ferguson, L. B. Fletcher, E. J. Gamboa, S. H. Glenzer, S. Göde, S. P. Hau-Riege, D. Kraus, J. Krzywinski, A. L. Levitan, K.-H. Meiwas-Broer, C. P. O’Grady, T. Osipov, T. Pardini, C. Peltz, S. Skruszewicz, M. Swiggers, C. Bostedt, T. Fennel, and T. Döppner, “Measurement of high-dynamic range x-ray Thomson scattering spectra for the characterization of nano-plasmas at LCLS,” *Review of Scientific Instruments* **87**, 11E709 (2016).
- E. Gamboa, B. Bachmann, D. Kraus, M. MacDonald, **M. Bucher**, S. Carron, R. Coffee, R. Drake, J. Emig, K. Ferguson, S. Glenzer, T. Gorkhover, S. Hau-Riege, J. Krzywinski, A. Levitan, K.-H. Meiwas-Broer, T. Osipov, T. Pardini, C. Peltz, S. Skruszewicz, C. Bostedt, T. Fennel, and T. Döppner, “Dual crystal x-ray spectrometer at 1.8 keV for high repetition-rate single-photon counting spectroscopy experiments,” *Journal of Instrumentation* **11**, P08015 (2016).
- C. Bernando, R. M. P. Tanyag, C. Jones, C. Bacellar, **M. Bucher**, K. R. Ferguson, D. Rupp, M. P. Ziemkiewicz, L. F. Gomez, A. S. Chatterley, T. Gorkhover, M. Müller, J. Bozek, S. Carron, J. Kwok, S. L. Butler, T. Möller, C. Bostedt, O. Gessner, and A. F. Vilesov, “Shapes of rotating superfluid helium nanodroplets,” *Physical Review B* **95**, 064510 (2017).
- M. A. Alcalde, **M. Bucher**, C. Emary, and T. Brandes, “Thermal phase transitions for Dicke-type models in the ultrastrong-coupling limit,” *Physical Review E* **86**, 4 (2012).

# **Eidesstattliche Versicherung**

Hiermit erkläre ich an Eides statt, dass ich die vorliegende Dissertation selbständig verfasst habe.  
Alle benutzten Quellen und Hilfsmittel sind aufgeführt.

Wiesbaden, den 28. Mai 2017

---

Maximilian Jakob Bucher

Ort, Datum

---

Diese Seite wurde maschinell gefertigt. Ein unterschriebenes Exemplar dieser Dissertation ist in der Universitätsbibliothek oder dem Universitätsarchiv der Technischen Universität Berlin hinterlegt.



# **Acknowledgment**

This has to be written.